THEORETICAL MODELING OF QUANTUM DOT INFRARED PHOTODETECTORS

By

Mohamed Abdelaziz Kotb Naser

THEORETICAL MODELING OF QUANTUM DOT INFRARED PHOTODETECTORS

By

Mohamed Abdelaziz Kotb Naser

B.Sc., Cairo University, Giza, Egypt (2000)
M.Sc., Cairo University, Giza, Egypt (2005)

A Thesis

Submitted to the School of Graduate Studies

in Partial Fulfillment of the Requirements

for the Degree

Doctor Philosophy

McMaster University

DOCTOR OF PHILOSOPHY (2009)
(Engineering Physics)

McMASTER UNIVERSITY
Hamilton, Ontario

TITLE: Theoretical Modeling of Quantum Dot Infrared Photodetectors

AUTHOR: Mohamed A. Naser
M.Sc., Engineering Physics
Cairo University, 2005
B.Sc., Electronics and Communication Engineering
Cairo University, 2000

SUPERVISOR: Dr. M. Jamal Deen
Professor, Electrical and Computer Engineering.

SUPERVISOR: Dr. David A. Thompson
Professor Emeritus, Engineering Physics.

NUMBER OF PAGES: xix, 172

ABSTRACT

Quantum **d**ot **i**nfrared **p**hotodetectors (QDIPs) have emerged as a promising technology in the mid- and far-infrared (3-25 μm) for medical and environmental sensing that have a lot of advantages over current technologies based on **M**ercury **C**admium **T**elluride (MCT) and **q**uantum **w**ell (QW) **i**nfrared **p**hotodetectors (QWIPs). In addition to the uniform and stable surface growth of III/V semiconductors suitable for large area focal plane applications and thermal imaging, the three dimension confinement in QDs allow sensitivity to normal incidence, high responsivity, low darkcurrent and high operating temperature. The growth, processing and characterizations of these detectors are costly and take a lot of time. So, developing theoretical models based on the physical operating principals will be so useful in characterizing and optimizing the device performance.

Theoretical models based on non-equilibrium Green's functions have been developed to electrically and optically characterize different structures of QDIPs. The advantage of the model over the previous developed classical and semi-classical models is that it fairly describes quantum transport phenomenon playing a significant role in the performance of such nano-devices and considers the microscopic device structure including the shape and size of QDs, heterostructure device structure and doping density. The model calculates the density of states from which all possible energy transitions can be obtained and hence obtains the operating wavelengths for intersubband transitions. The responsivity due to intersubband transitions is calculated and the effect of having different sizes and different height-to-diameter ratio QDs can be obtained for optimization. The dark and photocurrent are calculated from the quantum transport equation provided by the model and their characteristics at different design parameter are studied. All the model results show good agreement with the available experimental results.

The detectivity has been calculated from the dark and photocurrent characteristics at different design parameters. The results shows a trade off between the responsivity and detectivity and what determines the best performance is how much the rate of increase of the photocurrent and dark current is affected by changing the design parameters

Theoretical modeling developed in the thesis give good description to the QDIP different characteristics that will help in getting good estimation to their physical performance and hence allow for successful device design with optimized performance and creating new devices, thus saving both time and money.

ACKNOWLEDGMENTS

I would like to acknowledge the various supports that I have received throughout my research work and in writing this dissertation

Firstly, I would like to thank my supervisor, Prof. M. Jamal Deen, for trusting me with this work and giving me the opportunity to be involved in such a sophisticated and interesting topic of research. I would like to thank him for proposing many of the ideas presented here, which I was able to study in depth. Prof. Deen has been nothing short of a great mentor to me, offering his guidance throughout the intricacies of this research. The amount of energy and devotion he allocates for his work never ceases to amaze me, and he continues to set an example in organization, professionalism, and scholarly prowess that is very hard to follow.

Next, I would like to thank my co-supervisor Prof. David Thompson for his continuous support, encouragements and guidance. In particular, his help and great insights into the experimental aspects of my work are greatly appreciated. I am also very thankful to him for his many inputs into this dissertation documents and our publications.

I would also like to thank the committee members - Prof. Shiva Kumar and Prof. Paul Jessop for taking the time in reading, commenting, and providing feedback on this work. I would also like to thank them being in my committee.

Many thanks are due to all the members of our microelectronics lab and Engineering Physics department for being such a great team to work with. I start with Dr. Farseem Mohammedy, who is a dear friend and an extremely helpful colleague. My thanks to Waleed Shinwari for his valuable discussions and help. I would like to thank Munir Eldesouki and Dr. Ogi Marinov for their help and support. I would like to thank all members of Engineering Physics department from whom I have learnt a lot of things that help me fulfilling my research work,

especially Shahram Tavakoli and Cui Kai for collaborating with me in our common research on quantum dot devices.

Finally, I would like to thank all members of my family: My mother, Neamat Abdelaleem for her continuous praying and encouragements to me, my father Abdelaziz Kotb, who unfortunately, is no longer with us to see the completion of my formal education, my brothers and sisters (Nadia, Gamal, Magdy, Soma, and Kawser) for their continuous support and encouragement. Last, but by no means least, I express my most sincere thanks and gratitude to my dear wife Shimaa Adel for her great help and unwavering support during the final phase of my research. Together, they have always been there for me, and I am forever in their debt.

This thesis is dedicated to

My mother, my father,

My brothers and sisters,

My wife and

My coming children (insha Allah)

TABLE OF CONTENTS

LIST OF FIGURES

LIST OF ACRONYMS AND SYMBOLS

Acronyms

AFM	Atomic Force Microscope
DOS	Density of States
IR	Infrared
LIR	Long Infrared
MBE	Molecular Beam Epitaxy
MCT	Mercury Cadmium Telluride
MIR	Mid Infrared
NEGF	Non-Equilibrium Green's functions
NIR	Near Infrared
QD	Quantum Dot
QDIP	Quantum Dot Infrared Photodetector
QW	Quantum Well
QWIP	Quantum Well Infrared Photodetector

Symbols

α	Absorption Coefficient
λ	Wavelength
c	Speed of Light
ε_0	Free space Permittivity
η	Quantum Efficiency
a	Lattice Constant
R	Responsivity
D	Detectivity
E_F	Fermi Level Energy
E_g	Band gap
h	Planck's Constant
ω	Angular Frequency

Φ	Photon Flux
g	Gain
$\hbar\omega$	Photon Energy
$F(V)$	Electric Field
J	Current Density
k	Wave number
K	Boltzmann Constant
T	Temperature
m_o	Free electron Mass
V	Potential Energy
H	Hamiltonian
G^r	Retarded Green's Function
G^a	Advanced Green's Function
$G^<$	Lesser Green's Function
$G^>$	Greater Green's Function
$\sum^r$	Retarded Self-Energy
$\sum^a$	Advanced Self-Energy
$\sum^<$	In-scattering Self-Energy
$\sum^>$	Out-scattering Self-Energy
Γ	Broadening – Total Decay Rate
A	Spectral Function – Localized Density of States
t	Time or hopping parameter $\hbar^2 / 2ma^2$
T	Absolute Temperature or transmission function

CHAPTER 1 INTRODUCTION

High performance Infrared photodetectors in the mid- and far-infrared (3-25 μm) wavelength range have attracted much interest due to their important sensing applications [1]. They are used in medical and environmental sensing, optical communications, thermal imaging, night vision cameras, and missile tracking and recognition. It is required to obtain a technology that gives high performance at high operating temperature and with low cost. Current technologies based on Mercury Cadmium Telluride (MCT) [2, 3] and quantum well (QW) infrared detectors (QWIPs) [4-15] have some disadvantages that lower the overall performance of the sensing devices. The MCT's epitaxial growth problems limit the manufacturing yield of large area focal plane arrays (FPAs) applications [16, 17]. QWIPs do not support normal incidence detections and so need complicated optical coupling in addition to the requirement of operating at very low temperature [15].

The advance in epitaxial growth of heterostructure semiconductors allows for the fabrication of devices at nano scale dimensions. These nano-devices have new physical operating principles and novel performance characteristics. Quantum dots (QDs) grown by the self-assembled epitaxial technique have attracted much interest in recent years for laser [26-32] and photodetector applications [18 -25]. In addition to the low cost, stable and uniform surface epitaxial growth of the III/V semiconductors, suitable for large area FPAs application in thermal imaging, the three-dimensional confinement in QDs has many advantages such as the intrinsic sensitivity to normal-incidence light which simplifies the optical configuration for any application, reduced electron-phonon scattering, long-lived excited states, low dark current and high temperature

operation [18, 19]. These advantages make quantum dot infrared photodetectors (QDIPs) emerge as an alternative technology to replace QWIP and MCT infrared detectors. Therefore, improving the QDIP performance by optimizing the device design through accurate modeling is useful for obtaining the required characteristics. In this research work, theoretical models based on non-equilibrium Green's functions will be developed to describe the electrical and optical characteristics of QDIPs. The model results will be compared to the available experimental results and the models will be used for optimizing the device performance.

1.1. OPTICAL ABSORPTION

Semiconductor materials typically used for photodetectors in the visible and near infrared (< 2 μm) ranges are shown in Fig. 1-1. For longer wavelength detection, smaller band gap semiconductor materials are used for interband transitions. Alternatively, the intersubband transitions between the bound states in quantum nanostructure detectors such as QWIPs and QDIPs can be used for detection as shown in Fig. 1-2.

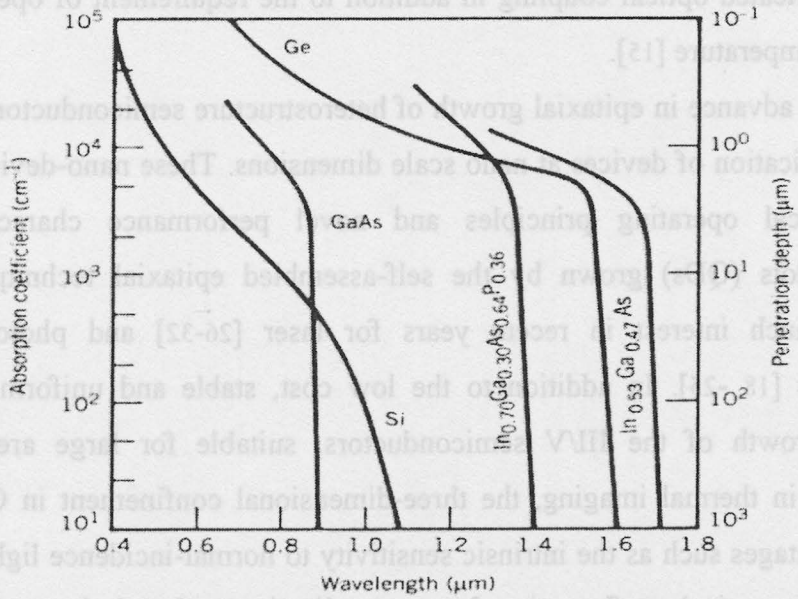

Figure 1-1 – Absorption coefficient as a function of wavelength for various semiconductor materials in the visible and near infrared domain

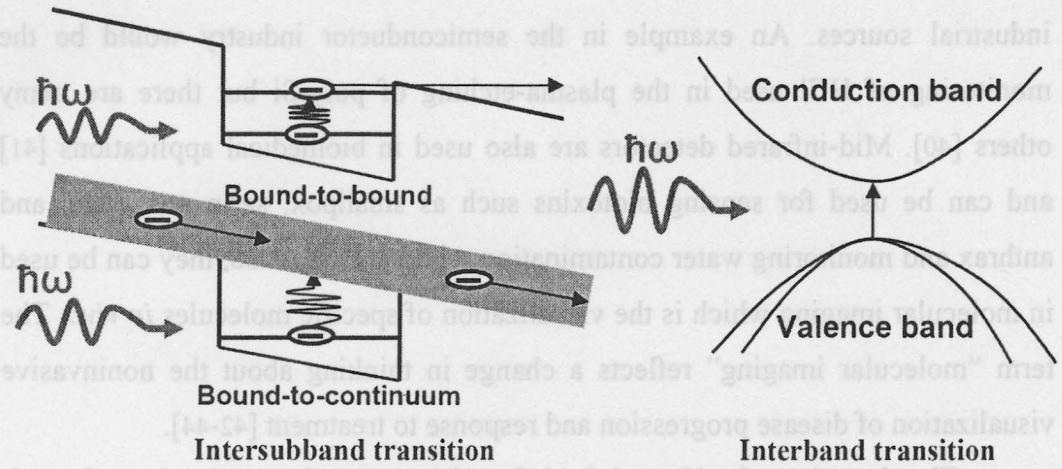

Figure 1-2 – Intersubband transition in quantum nanostructure systems vs. interband transition in narrow band gap materials for infrared detection

1.2. INFRARED PHOTODETECTORS

Near infrared wavelengths (< 2.0 μm) are extensively used in optical fiber communications due to their low attenuation compared to the visible range. The attenuation loss for single mode fiber at 1.55 μm is less than 0.2 dB/km and this leads to the need for fewer repeaters [33, 34]. This attenuation is very small compared to attenuation in the visible range which exceeds 5 dB/km [35]. The development of non-silica fibers allows having smaller attenuations at longer wavelengths in the mid-infrared [36] which makes the development of mid-infrared detectors important for telecommunications [37]. There are some important environmental and medical sensing applications that make the development of infrared detectors very attractive. For example, the remote sensing of gases in the atmosphere such as, for example, O_2, H_2O, CO, CO_2, CH_4, and NH_3 can be done using infrared detectors since the principle absorption lines of these gases lay in the range 0.6 to 2.5 μm [38, 39]. In particular, the monitoring of CO_2 can help in solving the global warming problem by identifying the regions where the emission of CO_2 is big and needs to be decreased. Mid-infrared detectors can be used to monitor forest fires, thermal and gas pollution from

industrial sources. An example in the semiconductor industry would be the monitoring of HCl used in the plasma-etching of poly-Si but there are many others [40]. Mid-infrared detectors are also used in biomedical applications [41] and can be used for sensing biotoxins such as smallpox, sarin gas, ricin, and anthrax and monitoring water contamination with bacteria. Also, they can be used in molecular imaging which is the visualization of specific molecules *in vivo*. The term "molecular imaging" reflects a change in thinking about the noninvasive visualization of disease progression and response to treatment [42-44].

The detection of mid- and far infrared wavelengths can be done through the interband transition process in narrow band gap semiconductors or through the intersubband transitions in quantum nanostructure detectors such as QWIPs and QDIPs. Semiconductor materials with narrow band gap materials such as InAsSb (III-V), PbSnTe (IV-VI), and HgCdTe (II-VI) are used for mid- and far-infrared detection. In addition to narrow band gap material detectors, Schottky barrier photosensitive detectors and doped silicon detectors are used. Photodetectors based on interband transitions in narrow band gap materials have some advantages such as high optical absorption, high quantum efficiency, high mobility and less thermal generation compared to extrinsic detectors and Schottky barriers [15]. The compositions of these materials in the alloy can be controlled for band gap engineering which allows detection of specific infrared regions. Amongst the interband transition detectors, the MCT-based are the most used as the other semiconductor based detectors suffer from less mature technology and their performance is much lower than the MCT photodiodes [9]. Although the MCT photodetectors have many advantages, the problem of the epitaxial growth and alloy instability make it difficult to produce a homogenous composition over a large area. These problems have limited the manufacturing yield of large FPAs which makes the final imaging system very expensive. The performance of the long wavelength infrared InAs/InGaSb superlattices (SL) photodiodes is comparable to MCT photodiodes. The InAs/InGaSb strained layer SL detectors

employ interband transitions across a fundamental energy gap. The band alignment in the structure is based on a type II interface where the conduction band of InAs is lower than the valence band of the InGaSb. Because of this band alignment the SL can have a band gap smaller than that of either constituent material. The presence of coherent strain due to a small lattice mismatch (< 5%) shifts the band edges such that the SL energy gap is reduced. This reduced band gap is advantageous because longer cut-off wavelengths can be obtained with reduced layer thickness in the strained SL, leading to even higher optical absorption coefficient. The resultant effective bandgap is dependent upon the composition, well width, and strain within the SL. The substrate difficulties and immature technology in addition to high dark current are some disadvantages that need further developments.

As an alternative, the intersubband transitions in QWIPs can be used to detect infrared light. QWIPs are based on III-V technology and mostly on GaAs/AlGaAs system. The dependence on the mature GaAs technology results in highly uniform and stable surface growth which is suitable for large area FPAs. Other advantages are the high control on the heterostructure design which gives a good control on the operating wavelength in addition to compatibility with high speed GaAs electronics and the low cost. However, QWIPs do not support normal incidence light detection which complicates the optical coupling. Also they have low quantum efficiency and high dark current and need to be operated at low temperature [15].

Recently, QDIPs consisting of self-assembled QD active regions have emerged as an alternative technology to replace quantum well and HgCdTe infrared photodetectors [24]. The intersubband transitions in the QD can be used to detect incident infrared radiation in the mid- and long-wavelength ranges (3-25 μm) [35]. The advantages of QDIP over MCT and QWIP will be discussed in the next section.

1.3. QUANTUM DOT INFRARED PHOTODETECTORS

The QDIP consists of a stack of QD arrays (layers) separated by wide band gap material layers. It is similar to the QWIP structure but replaces the QW layers with arrays of QDs as shown in Fig. 1-3.

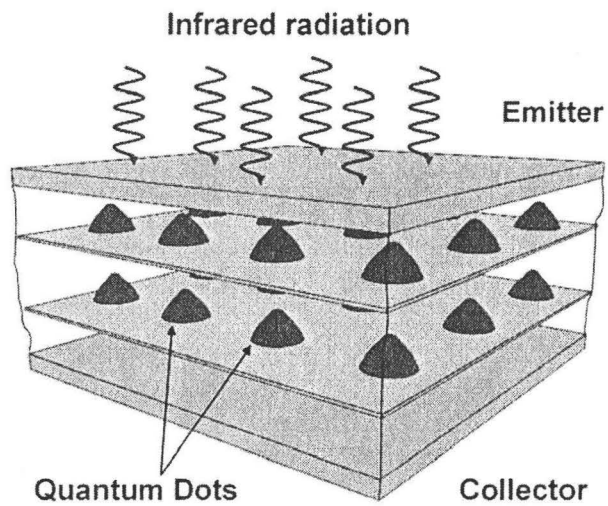

Figure 1-3 – Schematic of planar QDIP structure.

The QDs are formed by the self-assembled epitaxial technique. For example, a QDIP can be formed using QD layers of InAs or InGaAs separated by barrier material layers such as GaAs which have a higher conduction band edge. The QD material is deposited over the substrate and due to the lattice mismatch between deposited material and substrate, the strain is build up and after a critical thickness is reached, the two-dimensional growth changes into a three-dimensional one and dislocation free QD islands start to grow. The QD islands are covered with a layer of the substrate material and three-dimensional confinement of charges inside the QDs are obtained. The QD arrays play the role of the photosensitive base for the QDIP where photoexcited electrons are obtained through intersubband transitions. The QD active region of the QDIP is

sandwiched between heavily doped contact layers which can be viewed as the emitter and collector of the detector.

1.3.1. ADVANTAGES OF QDIPS

QDIPs fabricated using III-V semiconductor self-assembled QD layers show advantages over other infrared photodetector technologies such as those based on MCT and III-V based QWIPs. The main disadvantage of the MCT technology is the MCT's epitaxial growth problems, such as non-uniformity and instability of the growth surface, which limits the manufacturing yield of large area FPAs. The III/V semiconductors allow low cost, stable and uniform surface epitaxial growth, hence are suitable for large area FPA applications in thermal imaging. A problem with QWIPs is that they do not support normal incidence detection and so need complicated optical coupling in addition to the requirement of operating at very low temperature. However, the three-dimensional confinement in QDs has many advantages:

- The intrinsic sensitivity to normal-incidence light which simplifies the optical configuration for any application.
- Reduced electron-phonon scattering due to the large separation between the QD energy levels which exceeds the longitudinal optical phonon energy (phonon bottle-neck effect) [52, 53].
- High responsivity and high photoconductive gain due to the long-lived excited states [68].
- Reduced thermionic emission and low dark current and hence possible high operating temperature.

The main disadvantages are (1) the reduced absorption coefficient which can be overcome by increasing the absorption volume, through increasing the number of QD layers, and (2) the variable uniformity of the QD shape and size which needs to be minimized in order to enhance the absorption in a narrow wavelength range and (3) the non-uniform distribution of QDs in the layers [20]. So

optimizing the growth conditions to produce a high density of uniformly distributed QDs with a narrow size distribution within the layer will improve the absorption coefficient and give high detectivity values at a high operating temperature.

1.3.2. QDS FOR PHOTODETECTORS

For photodetectors applications, QDs should fulfill some requirements in terms of size, uniformity and material quality in order to be useful for good performance at room temperature.

1.3.2.1.Size

The size of the QD should be sufficiently large to have at least one energy level for an electron or hole inside the QD but should not be too large such that the separation between the energy levels inside the QD is below KT for high temperature operation. For example, the minimum diameter for a spherical QD of $InAs/Al_{0.4}Ga_{0.6}As$ to give one energy level inside the QD is about 3-5 nm. The upper limit in size is determined by limiting the population of higher energy levels and to get room temperature operation, the size for $InAs/Al_{0.4}Ga_{0.6}As$ QDs is 20 nm [54].

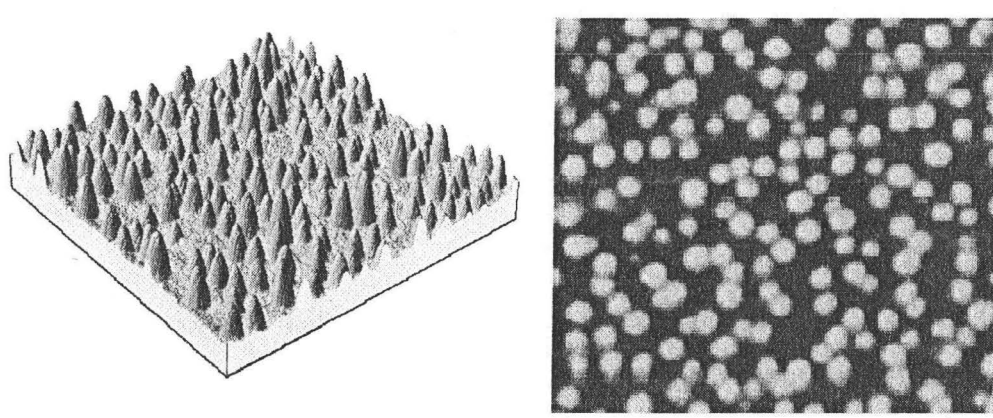

Figure 1-4 – Atomic force microscope image of InAs self-assembled QDs on GaAs, Courtesy: S. Tavakoli.

1.3.2.2. Uniformity

The nonuniform distribution of QDs in the layer affects the dark current characteristics. The dark current density increases in the regions where there are lacks of QDs in the QD layer due to the low potential energy at these punctures. So a high density, uniform distribution of QDs in the layers will reduce the dark current density of the detector. Also the minimum variance of the size variation of the QDs will increase the responsivity by enhancing the absorption at specific wavelength since the variation of the positions of the energy levels of the QDs will be small and then the photon energy to induce intersubband transitions will be almost the same for all QDs.

1.3.3.QDIP CHARACTERISTICS

The QDIP using intersubband transitions have been studied and characterized experimentally [55- 63]. The following are the main operating characteristics of interest for QDIPs

- The operating wavelengths corresponding to the peaks of the responsivity of the detector. By calculating the energy eigenvalues corresponding to both bound and continuum states of the QDs, the photon energies corresponding to all possible intersubband transitions between the energy states can be obtained and hence the operating wavelengths of the detector.
- The dark current due to thermionic emission and field assisted tunneling
- The responsivity which is the photocurrent, I_{ph}, per unit watt of incident light

$$R_p = I_{ph} / \Phi\hbar\omega, \tag{1.1}$$

where $\hbar\omega$ is the photon energy and Φ is the intensity of the incident photon flux, i.e. the number of photons per unit area per unit time.

- The detectivity which is a measure to the signal to noise ratio and is given by

$$D = \frac{R_p A^{1/2}}{S_i^{1/2}} \left[\frac{\text{cm.Hz}^{1/2}}{\text{W}^{-1}} \right], \tag{1.2}$$

where R_p is the peak responsivity, S_i is the noise density spectra, where $S_i^{1/2} = I_{\text{noise}} / \sqrt{\Delta f}$ and Δf is the band width of where the noise current is measured, and A is the detector area. The noise density is related to the dark current, as shown experimentally, through the relation [49]

$$g = \frac{S_i}{4qI_{\text{dark}}} + \frac{1}{2N}, \tag{1.3}$$

where g is the photoconductive gain and N is the number of QD layers. For a large value of N, the second term can be neglected compared to the first term and the noise density can be approximated by

$$S_i^{1/2} \simeq \sqrt{4qI_{\text{dark}} g} \tag{1.4}$$

- The photoconductive gain and quantum efficiency

The photoconductive gain can be given in terms of the carrier life-time which is the time the photocarriers have after photoexcitation until capturing or relaxing back to the QD and the transit time which is the time the carrier needs to be collected by the contacts such that $g = \tau_{\text{life}} / \tau_{\text{transit}}$. The photoconductive gain of QDIP can be extracted experimentally from the measured dark and noise currents as shown in Eq. (1.4). The quantum efficiency is related to the responsivity and photoconductive gain through the relation [15]

$$R_{\text{p}} = \frac{eg}{\hbar\omega}\eta \tag{1.5}$$

The quantum efficiency describes how well the detector couples to the detected light. It is defined as the number of photoexcited carriers per incident photon.

1.3.4. QDIP STRUCTURES

There are different QDIP structures according to the heterostructure design of the detectors. By careful design of the QDIP heterostructure the performance of the QDIP can be improved. The design can improve the responsivity, reduce the dark current, and improve the absorption coefficient by increasing the number of QD layers and the absorption volume.

1.3.4.1. 70 layers planar array

The QDIP reported in [24] has a planar structure of 70 layer QD arrays to increase the absorption volume. The barrier width between the QD layers has been controlled to allow growth of this large number of layers, with a minimal amount of dislocations. A relatively wide barrier between the QD layers of 50 nm was used. Substrate temperature cycling was applied during the growth of the GaAs barriers to allow this large number of QD layers to be grown with minimum dislocations [24]. A variation of QDs was obtained with larger dots located at the top of the QD stack and the smaller ones located near the bottom of the stack. The peak responsivity of the detector obtained at 2 V applied bias was 0.12 A/W and the dark current was 1.83×10^{-2} A/cm^2 at T=175 K which is low at this temperature due to the large width of the GaAs barrier.

1.3.4.2. Quantum Dot-in-a well detector QDWELL

The QDWELL structure reported in [45] is a hybrid between QWIP and conventional QDIP. In this device, the InAs QDs were grown inside an $In_{0.15}Ga_{0.85}As$ QW which was covered by GaAs barriers as shown in the schematic of the conduction band offset profile in Fig. 1-5. It combines the advantages of a QDIP and QWIP such that it allows for normal incidence operation, as for the QDIP, and also provides better control of the operating wavelengths through bound-to-bound transitions instead of bound-to-continuum transitions. The electrons are photoexcited from the ground state of the QD to a set of bound states provided by the QW. The measured peak responsivity at 1 V

was 0.0125 A/W which is low due to the small number of layers (15 layers) and the non optimized thickness of the barrier layers [45].

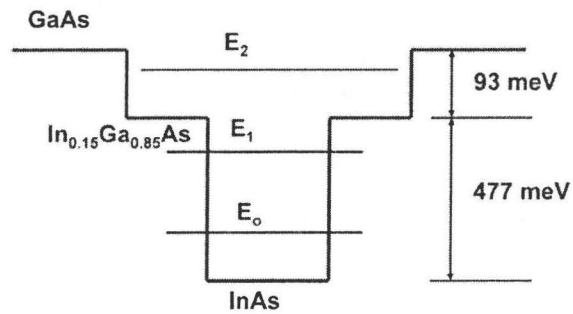

Figure 1-5 – Schematic of the conduction band offsets and the energy levels of the QDWELL structure.

1.3.4.3. Superlattice SL-QDIP

The SL-QDIP structure reported in [24, 46] is a modification of the QDWELL. InAs QDs were directly grown on AlAs layers as shown in Fig. 1-6. The AlAs barriers form a QW structure. The width of the QW can be controlled to change the positions of the minibands formed for wavelength tunability. The growth of InAs on AlAs instead of GaAs leads to increasing the density of QDs by an order of magnitude due to the low mobility In on AlAs compared to GaAs [24]. The SL-QDIP shows high peak responsivity of about 2.5 A/W at 78 K due to the large QD density which allows increased absorption of IR light. A high responsivity detector is suitable for low level signal detection. However the measured dark current [46] is high due to the thin active region of the detector which requires operation at low temperature.

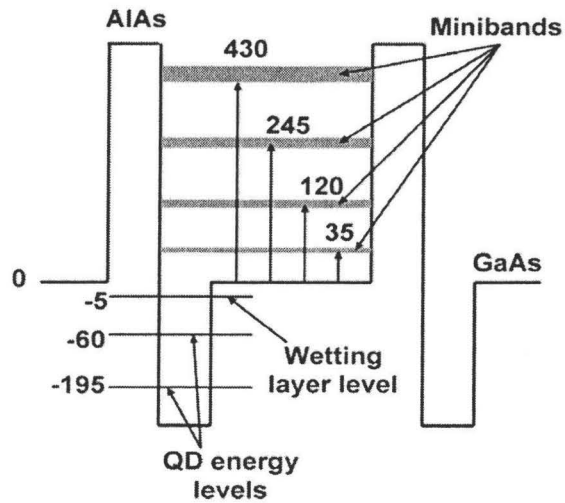

Figure 1-6 – Schematic of the conduction band offset profile of the SL-QDIP demonstrating the energy levels in the QD and wetting layers and mini-bands in the QW (in meV) relative to conduction band of GaAs.

1.3.4.4. Resonant tunneling RT-QDIP

The RT-QDIP reported in [24, 47, and 48] consisted of InGaAs QD layers. Associated with each QD layer are a double barrier $Al_{0.3}Ga_{0.7}As$/ $In_{0.1}Ga_{0.9}As$ and a single barrier $Al_{0.1}Ga_{0.9}As$ forming a resonant tunneling structure as shown in Fig. 1-7. The widths of the double barrier and QW are chosen such that the energy levels in both of them coincide allowing for resonant tunneling through the structure. Resonant tunneling will enhance the photocurrent by allowing photoexcited electrons with the resonant energy to be transmitted, while the dark current will be reduced due to the blocking of the broad distribution of the thermal excited carriers. A dark current density as low as about 1.6 A/cm^2 is measured at 300 K and 1 V applied bias. This low value of the dark current allows the photoresponse to be detectable, even at room temperature, due to the almost two orders of magnitude reduction compared to that measured in conventional QDIP and the measured responsivity is about 0.15 A/W at a long wavelength response at 17 μm at room temperature. The detectivity measured is about 10^7 $cmHz^{1/2}/W$ at

17 μm. Further improvement of the detector design can give higher values of peak responsivity and detectivity making it suitable as a room temperature IR detector.

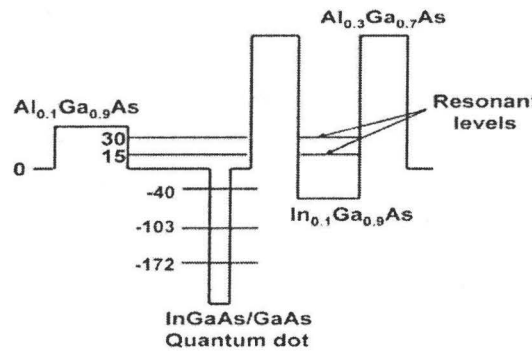

Figure 1-7 – Schematic of the conduction band offset profile of the RT-QDIP demonstrating the energy levels in the QD and the QW (in meV) relative to conduction band of GaAs.

1.4. THEORETICAL MODELING OF QDIP

1.4.1. CLASSICAL MODEL

The electronic transport model is based on a balance equation between the thermal and photoexcitation rates of electrons from the QDs and the capture or relaxation rate into the QDs [16, 25, 64-69]. The balance equation at steady state is given by [65]

$$\frac{\langle J \rangle}{e\Sigma_{QD}} P = G_k + G_t + \sigma I \langle N \rangle \tag{1.6}$$

The L.H.S is the capture rate and $\langle J \rangle$ is the current density; P is the capture probability and Σ_{QD} is the QD density. The R.H.S is the thermal and photexitation rates per QD where G_k is the thermionic emission rate, G_t is the field assisted tunneling rate, and σ is the cross section of the photon induced electron escape from QDs, I is the photon flux intensity, and $\langle N \rangle$ is the average number of electrons per dot.

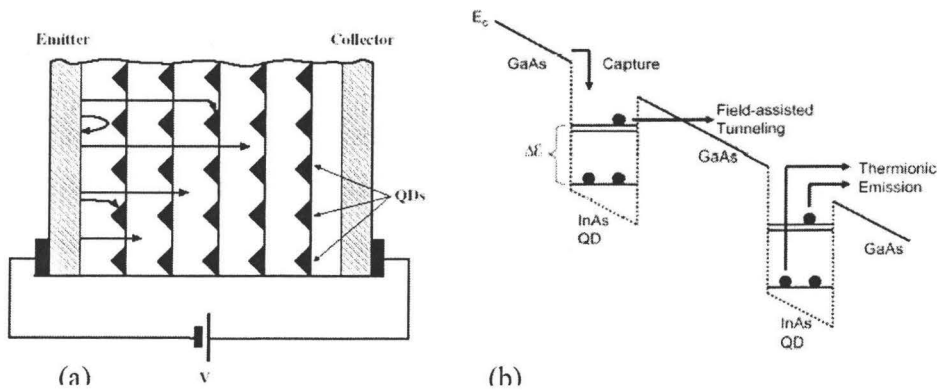

Figure 1-8 – (a) Schematic of cross-sectional view of the QDIP; arrows indicates possible trajectories of electrons, (b) schematic of the conduction band profile illustrating QD capture, field-assisted tunneling, and thermionic emission processes used in the balance equation under dark conditions [65][25].

Electrons escape the QDs by thermal excitation from the bound states of the QDs to the continuum states above the QD barrier as shown in Fig. 1-8 (b) Electron in the excited states can also escape the QDs by field assisted tunneling through the triangular barrier of the QDs due to the electric field of an applied bias. At steady state response, electrons escaping the QDs by thermal excitation, field assisted tunneling or photoexcitation in the presence of light are balanced by electrons captured by the QDs as described by Eq. (1.6). The average current density in Eq. (1.6) can be expressed as [65]

$$\langle J \rangle = J_{\max} \Sigma_{\mathrm{QD}} \int dr^2 \exp\left(\frac{e\varphi_1(N)}{k_{\mathrm{B}} T} \right) \tag{1.7}$$

where $J_{\max}$ is the maximum current density provided by the emitter and $\varphi_1(N)$ is the potential energy distribution in the QD layer adjacent to the emitter as a function of the average number of electrons per dot which satisfies the balance equation (1.6). The average potential energy through the device satisfies Poisson Equation and the Dirac delta functions are used to represent the average 2-D charge density of the QD layers. The average potential energy is given by

$$\frac{d^2\langle\varphi\rangle}{dz^2} = \frac{4\pi e}{\varepsilon}\sum_{k=1}^{K}\left(\langle N\rangle\Sigma_{QD} - \Sigma_D\right)\delta(z-kL) \tag{1.8}$$

The thermionic emission current density of the emitter and the average potential energy are solved simultaneously such that they satisfy the balance equation given by Eq. (1.6). The thermionic emission and field assisted tunneling rates and the capture probability are given in [25, 65, 69]. The relations used to calculate these rates contain fitting parameters that need to be extracted by comparisons with experimental results. The analytical solutions based on this model shows good agreement with experimental results for dark and photocurrents for QDIPs at low applied biases (< 1 V) as shown in [65, 69]. The model can be used to fit the dark current results at < 3 V with modification of some of the fitting parameters as shown in [25]. The dependence of fitting parameters in obtaining the transition rates, instead of the actual calculations of these rates, limits the use of the model for optimization to get the best designs. Moreover, the model does not take into consideration the microscopic device structure including the shape and size of QDs and the heterostructure design including quantum wells or tunneling barriers that have a big effect in determining the device characteristics.

1.4.2. SEMICLASSICAL MODEL

Microscopic models such as those reported in [70, 71], provide a better description of the QDIP relevant parameters by taking into consideration the QD shape and size to calculate the QD wavefunctions, which in turn can be used to calculate the transition rates. The current is calculated using a semiclassical Boltzmann equation. At steady state under dark or light conditions, the population of QD energy levels and consequently the dark current and responsivity are calculated.

The model considers the simplest possible periodic arrangement of the QD layers. Instead of the random arrangement of QDs in different layers as appeared in Fig. 1-9 (a), QDs in all layers are chosen to be aligned as shown in Fig. 1-9 (b).

This simplification is chosen because the transport properties are believed not to depend on the QD arrangement since the transport of electrons from one QD layer to the next one is done through the continuum states and not the direct transport through the QD bound states. Therefore, electrons are exited from bound states of QDs to continuum states, mainly localized in the QD region, and then they are transported via continuum states to the next QD layers until they are collected by contacts or captured by QDs in the next layers and relaxed from continuum states to QD bound states. Fig. 1-9 (c) shows a cylindrical volume in which the Hamiltonian eigenvalue problem is solved to obtain the energy eigenvalues and the corresponding wavefunctions. An orthonormal wavefunction expansion method is used to get the eigenenergies and the corresponding wavefunctions [70, 71].

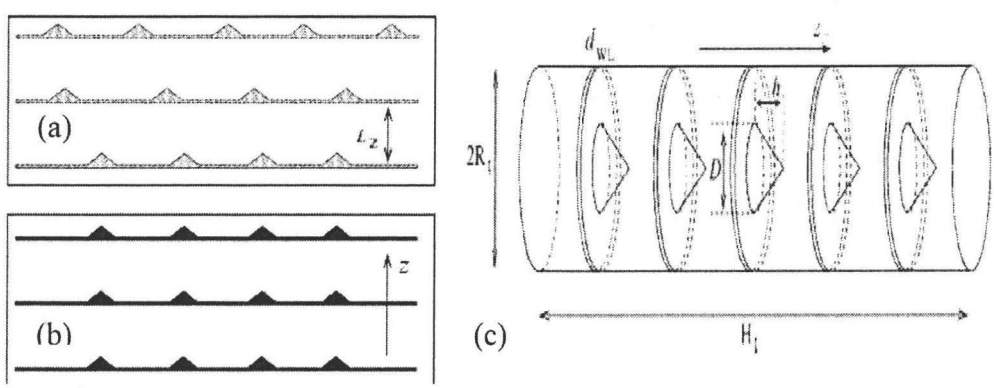

Figure 1-9 – Schematic view of QDIP periods: (a) realistic structure and (b) structure used by the model. (c) The region in space in which the Hamiltonian eigenvalue problem is solved illustrating conical shaped QDs [70].

A similar method of using eigenfunctions expansion to obtain the eigenstates of the QD-in-a well detector is shown in [45, 72]. The eigenfunctions of the Hamiltonian of a cylindrical volume encompassing a QD can be written as a superposition of basis functions formed by the product of the Bessel function of integer n with the sine function assuming zero boundary conditions on the cylindrical surface. The eigenfunctions can be written as [72]

$$\psi_n(r,z,\theta) = \sum_{i>0,j>0} A_{i,j}^n \zeta_{i,j}^n(r,z,\theta),$$
$$\zeta_{i,j}^n(r,z,\theta) = \beta_i^n J_n(k_i^n R) e^{in\theta} \sin(K_j z) \tag{1.9}$$

where $k_i^n R$ is the ith zero of the Bessel function of order n, R is the cylinder radius, $K_j = j\pi / Z$ and Z is the cylinder height and β_i^n is the normalization constant. The choice of the Bessel and sine functions forces zero boundary conditions on the cylinder surface enclosing the QD which gives good results for the ground state of the QDs; however, assuming zero boundary conditions is less accurate for the higher excited states near the QD barrier and not suitable for getting the wetting layer energy levels or continuum states. Other theoretical models used to calculate the QD energy eigenvalues and the corresponding wavefunctions are based on the eight-band **k.p** model [73]. Most of these models predicts a separation between the ground state and the first excited of about 50-60 meV (20-25 μm). However, many experimental groups report intersubband QDIPs with photoresponse in the range of 4-7 μm [49, 50]. The wavefunctions are used to calculate the transition rates due to interaction with longitudinal optical (LO) phonons and interaction with light. The electron-LO phonon interaction was considered in the strong coupling regime where the carrier lifetime is determined by the decay of a LO phonon into two longitudinal acoustic phonons. The details of the model are shown in [70, 71]. The interaction with light is treated using the first order dipole approximation and the Fermi golden rule and the optical cross section of the transition from initial state $|i\rangle$ to a final state $|f\rangle$ is given by

$$\sigma_{if}(\omega) = \frac{2\pi}{n\varepsilon_0 c\omega A^2} \left|\langle i|\hat{H}'|f\rangle\right|^2 \delta(E_f - E_i - \hbar\omega) \tag{1.10}$$

where $\hat{H}'$ is the Hamiltonian due to interaction with the electromagnetic field. The occupation of the energy levels and the current density are obtained from a semiclassical Boltzmann model where systems of rate equations are formed and given by [70]

$$\frac{dn_i}{dt} = \sum_{j \neq i} W_{ji} n_j \left(1 - \frac{1}{2} n_i\right) - \sum_{j \neq i} W_{ij} n_i \left(1 - \frac{1}{2} n_j\right) - \sum_j \sigma_{ij}(\omega)\left(n_i - n_j\right)\Phi, \qquad (1.11)$$

$0 \leq n_i \leq 2$ including spin degeracy

where the energy levels of the QDs are denoted by $i \equiv (M, P)$ representing the P^{th} level of the QD of M^{th} layer, W_{ij} is the total transition rate from the state i to the state j due to interactions with phonons, $\sigma_{ij}(\omega)$ is the optical cross section between the states i and j due to photon absorption of energy $\hbar\omega$, and Φ is the flux of incident radiation. Equation (1.11) is solved under steady state conditions $(d/dt = 0)$ by imposing a condition on the total number of electrons in the system. It was assumed that on the average there is 1 electron per dot which is a typical QD occupation at relatively small applied biases. After solving the system of equations in (1.11), the current density can be obtained from [70]

$$J_{if} = -e\left(w_{if} + \sigma_{if}\Phi\right) n_i \left(1 - \frac{n_f}{2}\right) \times \left[p_i\left(1 - p_f\right) - p_f\left(1 - p_i\right)\right] \qquad (1.12)$$

where J_{if} is the current density due to the transition from the state i to the state f. A reference plane is chosen perpendicular to the growth direction where electrons can be counted when passing through the reference plane; p_i is the probability that the electron in state i is located to the left of the reference plane and p_f is the probability that the electron in state f is located to the right of the reference plane. The probability calculation and details of the model are given in [70].

1.4.3. QUANTUM TRANSPORT MODEL

A quantum transport model can be used to produce a better description of the electron dynamics in QDIPs. The semiclassical models based on Boltzmann formalism combine Newton's law with a probabilistic description of the interaction with random scattering forces. However, the non-equilibrium Green's functions (NEGF) is a quantum transport model that combines Schrödinger

equation for quantum dynamics with statistical description of dissipative interaction [79]. The advantage of such a quantum transport model is that it gives a general framework to deal with quantum structure under non-equilibrium conditions such as high applied biases and in the presence of internal interactions. The interactions inside the device can be electron-electron, electron-phonon or electron-photon interactions. According to the type of interactions included, electron scattering can be elastic, which causes no energy transitions between different energy states or inelastic which leads to energy transitions. The straightforward way of including interactions in the system gives considerable flexibility in the types of interactions to be included and the degree of approximations to be used depending on the accuracy required in the results and the complexity of the calculations. The model should take into consideration the microscopic device structure such as, the shape, size and composition of QDs, density of QDs, and doping density as well as the internal structure design which is useful in device design optimization as it describes the realistic device structure and physical operation. The internal parameters such as density of states (DOS) and electron density, in addition to the transmission function and current, can be obtained.

1.5. THESIS OBJECTIVE

The objectives are to develop theoretical models to well describe the electrical and optical properties of QDIP which can be used for device design optimization for better performance. Improving the device performance experimentally by fabricating and testing devices using combinations of different design parameters are very costly and time wasting. Hence, it is desirable to develop theoretical modeling based on the physical operating principals that can be used in characterization and optimizing the device performance through recommending the best design parameters suitable to achieve specific characteristics. In addition, the models can be used as a design tool to create new

device structures and making comparisons between different structures to establish the best structure for a specific characteristic, such as a high operating temperature, a high responsivity or a high signal-to-noise ratio. Each can be suitable for certain operating conditions.

The research objective is to develop theoretical models based on NEGF that can be used for electrical and optical characterization of QDIPs and give a good physical understanding of the device operation in order to have a guideline to improve the device design. Unlike classical and semi-classical models that are based on fitting parameters or depend on classical physics, the NEGF models developed in the thesis are quantum mechanical models that fairly describe quantum transport phenomenon where energy quantization and tunneling have significant role in the performance of such nano-devices. For any QDIP structure, the model considers the microscopic detector structure including the shape and size of QDs, number of QD layers, the separation between the layers, and the QD doping density. A summary of the results obtained by the NEGF models developed in the thesis are given below

- The density of states of the QDs that gives both the discrete energy levels in the QDs in addition to the continuum states outside the QDs.
- The energy levels provided by the density of states give information about the possible energy transitions and therefore the operating wavelengths of the detector.
- The corresponding calculated wavefunctions are used to calculate the dipole moment between different energy states which indicate the strength of the transition rates between the energy states and therefore gives information about the relative peak of the responsivity of the detector.
- The effect of changing the shape and size of QDs has been studied to establish their effects on the operating wavelength and the

corresponding value of the responsivity.

- The dark current characteristics at different applied biases have been obtained for different design parameters such as the barrier separation between QD layers, the number of QD layers and the QD doping density to test different design performances.
- The photocurrent characteristics at different design parameters have been obtained for comparison with the dark current characteristics to get the best device performance.
- The detectivity of the detector with different design parameters has been calculated using the dark and photocurrent results to obtain the best operating conditions and the best design performance, and can be used for comparisons between different QDIP structures.

To achieve the research objectives, a detailed theoretical model based on NEGF has been developed [74, 75, 76]. The model takes into consideration the microscopic device structure such as the shape and size of QDs, density of QDs, doping density in addition to the internal structure design. The model is fully quantum mechanical, including interactions with the lattice and with the light. The model uses the potential energy and electron effective masses based on a single band effective mass approximation. The governing equation of the Green's functions is obtained in the cylindrical coordinates to be suitable for conical shaped QDs that have a cylindrical symmetry around its axis. Making use of the cylindrical symmetry and assuming local interactions allow reduction of the size of the problem to 2D instead of 3D which simplifies the numerical solution. The differential equation of the retarded Green's function in cylindrical coordinates is discretized using the method of finite differences and the retarded Green's function matrix is obtained by a matrix inversion. The localized DOS of the QD is obtained from the retarded Green's function and from which both the discrete energy levels and the continuum states above the QD barrier are obtained [76].

The DOS shows all possible energy transitions which indicate the operating wavelengths of the detector. The model is used to calculate the spectral function and density of states of different QDIPs such as the quantum dot in a well [76], superlattice and resonant tunneling QDIPs [75]. Information of electronic states, operating wavelengths and allowed energy transitions are obtained and they are in a good agreement with experimental results. The responsivity of QDIPs is calculated using the first-order dipole approximation and Fermi-golden rule, and the results obtained by the model are in a good agreement with the experimental results. The model is used for optimizing the responsivity with respect to the shape and size of QDs to give an insight into the growth requirements needed to give the best responsivity values. [75].

The quantum transport equation of the NEGF is solved numerically to calculate the dark and photocurrent of the RT-QDIP [74]. The dark and photocurrent results by the model are in good agreement with the experimental results over a wide range of applied biases and temperatures. The model has also been used for theoretical predictions of the dark and photocurrent characteristics at different design parameters for detectivity optimization. The effect of using different design parameters such as the number of QD layers, the barrier separation between the layers and the QD doping density on the dark and photocurrent has been obtained. The interaction with light for photocurrent calculations has been done using the first order dipole moment and the Fermi-golden rule. From the dark and photocurrent results, the detectivity of the detector has been calculated for different design parameters. The model has been applied to the RT-QDIP structure for dark current, responsivity and detectivity modeling and the result obtained by the model was in good agreement with experimental results. The model has been used to test different design parameters to get their effect on the RT-QDIP characteristics to get the best design performance.

The electrical and optical characterization by the model is very helpful, because after getting good matching with the experimental observations, the

model can be used to test different alternatives of design parameters to get the best design without the need of the actual fabrication of trial devices. The simulation tool provided by the model will be helpful to predict and design a detector with prescribed characteristics suitable for specific applications in the biomedical and industrial fields, saving money and time.

The research work presented in this thesis has resulted in the following publications:

Journal papers

- M. A. Naser, M. J. Deen and D. A. Thompson, "Photocurrent modeling and detectivity optimization in a resonant tunneling quantum dot infrared photodetector," *IEEE J. Quantum. Elect.*, 11 pages, Submitted (October 2009).
- Shahram Ghanad-Tavakoli, M. A. Naser, David A. Thompson, and M. Jamal Deen, "Experimental characterization and theoretical modeling of the strain effect on the evolution and inter-band transitions of InAs quantum dots grown on $In_xGa_{1-x}As$ ($0.0 \leq x \leq 0.3$) metamorphic pseudosubstrates on GaAs wafers", *Journal of Applied Physics*, Vol. **106**, # 063533, 8 pages (28 September 2009)
- M. A. Naser, M. J. Deen and D. A. Thompson, "Theoretical modeling of dark current in quantum dot infrared photodetectors using non-equilibrium Green's functions," *Journal of Applied Physics*, Vol. **104**, #014511, 11 pages (1 July 2008).
- M. A. Naser, M. J. Deen and D. A. Thompson, "Spectral function and responsivity of resonant tunneling and superlattice quantum dot infrared photodetectors using Green's function," *Journal of Applied Physics*, Vol. **102**, # 083108, 12 pages (15 October 2007).

  The paper has also been chosen to be in the *Virtual Journal of Nanoscale Science & Technology*, Vol. **16**, Issue 19, (Nov. 5, 2007).

- M. A. Naser, M. J. Deen and D. A. Thompson, "Spectral function of InAs/InGaAs quantum dots in a well detector using Green's function," *Journal of Applied Physics*, Vol. **100**, #093102, 6 pages (Nov.1, 2006).

  The paper has also been chosen to be in the *Virtual Journal of Nanoscale Science & Technology*, Vol. **14**, Issue 21, (Nov. 20, 2006).

Conference papers

- M. A. Naser, M. J. Deen and D. A. Thompson, "Photocurrent Modeling of Resonant Tunneling Quantum Dot Infrared Photodetectors," submitted to 217th ECS Meeting, Vancouver, Canada | April 25-30, 2010.
- M. A. Naser, M. J. Deen and D. A. Thompson, "Theoretical Modeling of Quantum Dot Infrared Photodetectors," 14th Canadian Semiconductor Technology Conference (12 August 2009).
- M. A. Naser, M. J. Deen and D. A. Thompson, "Modeling and Optimization of Quantum Dot Infrared Photodetectors," Electrochemical Society Conference, (1 July 2008).

1.6. THESIS ORGANIZATION

The thesis contains seven chapters. Chapter 1, above, discussed the different applications of infrared detectors in medical and environmental sensing. The QDIP is a promising technology with advantages over current technologies based on QWIP and MCT. A literature review of QDIP modeling, including classical and semi-classical methods, has been discussed in addition to an overview of the NEGF modeling that has been developed in the thesis.

Chapter 2 gives a review of the NEGF. The different Green's functions, the self energy, and scattering functions are presented as they will be used intensively in the following chapters of the thesis. The kinetic equation of the NEGF has been shown. The method of finite differences is presented and applied

to solve one dimensional problems as simple examples of the way of solving the differential equation governing the Green's function in the later chapters. Some applications of Green's function have been presented such as solving the wave equation, the transmission function and the current.

Chapter 3 shows the development of theoretical modeling to obtain the DOS of the QDIP. The localized DOS is obtained from the retarded Green's function. The retarded Green's function is obtained numerically by solving the governing kinetic equation using the method of finite differences. The model was applied to calculate the DOS of three different QDIP structures such as QDWELL, SL-QDIP, and RT-QDIP. The chapter is based on the published journal papers [76] and [75].

Chapter 4 shows the development of theoretical modeling to calculate the responsivity of the QDIP. The first order dipole approximation and the Fermi-golden rule were used to model the interaction with light. The bound states of the QDs have been obtained by solving the eigenvalue problem of the QD Hamiltonian, while the continuum states have been obtained using the retarded Green's function. The model has been applied to the SL-QDIP and RT-QDIP. The effect of changing the shape and size of QDs on the calculated responsivity has been studied using the SL-QDIP structure. The chapter is based on the paper [75].

Chapter 5 shows the development of theoretical modeling to obtain the dark current characteristics of QDIP. A uniform self-energy model corresponding to a constant scattering rate has been used to simplify the calculations. A self-consistent solution of the potential energy and charge density has been obtained. The model has been applied to the RT-QDIP and good matching with measured data has been found for a wide range of temperatures and applied biases. The model was used to obtain the dark current characteristics at different design parameters for design optimization. The chapter is based on the paper [74].

Chapter 6 shows the development of theoretical modeling to obtain the photocurrent of the QDIP. The dark current model of chapter 5 has been upgraded to include the interaction with light to calculate the photocurrent. The interaction with light is added using the first order dipole approximation and the Fermi-golden rule. The model has been applied to the RT-QDIP and the responsivity obtained by the model was in good agreement with that measured. The detectivity of the RT-QDIP has been calculated using the dark and photocurrent characteristics and different design parameters have been tested for detectivity optimization.

Finally, chapter 7 concludes the thesis with the major findings and the recommended improvements and extensions for future research. Appendix A shows application of the finite difference method to numerically solve the governing kinetic equation of the retarded Green's function in the cylindrical representation and the conversion to matrix equation. Appendix B shows detailed calculations to the Green's function in the lead outside the QD cylinder which is used to calculate the self-energy added to the QD Hamiltonian due to coupling with the surrounding lead.

CHAPTER 2 NON-EQUILIBRIUM GREEN'S FUNCTIONS

The Green's function is a powerful concept that gives the response at any point due to any excitation at any other point. The excitations can be due to waves incident from the contact leads or due to the internal interactions such as electron-electron, electron-phonon or electron-photon interactions. For non-interacting transport, the excitations are only from coupling with the leads and then the transport is coherent and the Green's function is equivalent or related to a generalized Scattering-matrix approach that can be used to calculate the transmission function and describe the electronic transport. For interacting transport, where the internal interactions within the device exist, the transport is non-coherent and hence the Green's functions are very powerful in describing quantum transport including dissipative internal interactions [80-95]. Simple treatment of the problem using the S-matrix approach or the semi-classical Boltzmann equation is not sufficient to give good results.

The concept of Green's function can be used in many physical topics, and whenever the response R is related to the excitation S by a differential operator D_{op}

$$D_{op}R = S, \tag{2.1}$$

the Green's function and the response [79] can be expressed in the form

$$R = D_{op}^{-1}S = GS \text{ where } G \equiv D_{op}^{-1} \tag{2.2}$$

For a Schrödinger like equation with a source term in the right hand side,

$$\left[E - H_{op}\right]\Psi = S, \tag{2.3}$$

where H_{op} is the Hamiltonian operator, Ψ is the wavefunction and S is the excitation term due to a wave incident from the leads, the Green's function is defined as

$$G=\left[E-H_{op}\right]^{-1},\ \text{where}\ H_{op}=\frac{\left(i\hbar\nabla+eA\right)^2}{2m}+U(r) \tag{2.4}$$

The Green's function defined in (2.4) is not unique, as the inverse of a differential operator needs to have the boundary conditions specified to give a unique solution. For example, the Green's function for a simple 1D problem with a constant potential energy U,

$$G=\left[E-U+\frac{\hbar^2}{2m}\frac{\partial^2}{\partial x^2}\right]^{-1} \tag{2.5}$$

which can be written as

$$\left[E-U+\frac{\hbar^2}{2m}\frac{\partial^2}{\partial x^2}\right]G(x,x')=\delta(x-x') \tag{2.6}$$

Equation (2.6) is just like the Schrödinger equation except with the delta function source term in the R.H.S, and the Green's function gives the wave function at x due to a unit excitation at x'. There are two solutions for (2.6) referred to as the retarded Green's function (G^r) and the advanced Green's function (G^a) and are given by

$$\begin{aligned} &G^r(x,x')=-\frac{i}{\hbar v}\exp\left[ik\left|x-x'\right|\right]\ \text{and}\ G^a(x,x')=+\frac{i}{\hbar v}\exp\left[-ik\left|x-x'\right|\right] \\ &\text{where}\ k=\frac{\sqrt{2m(E-U)}}{\hbar}\ \text{and}\ v\equiv\frac{\hbar k}{m} \end{aligned} \tag{2.7}$$

Physically the retarded solution gives an outgoing plane wave originating at the excitation point x' and going away to $\pm\infty$, while the advanced solution gives an incoming plane wave from $\pm\infty$ and that disappear at the excitation point x'. The boundary conditions can be incorporated in the differential equation to make one solution a valid and finite one while the other one is growing to

infinity when going away from the source term. This can be done by adding an infinitesimal imaginary part to the energy. The sign of this imaginary term specifies which solution is the finite one. Equation (2.6) can be rewritten as

$$\left[E-U+\frac{\hbar^2}{2m}\frac{\partial^2}{\partial x^2}\pm i\eta\right]G^{r,a}(x,x')=\delta(x-x') \tag{2.8}$$

The small imaginary part added to the energy causes a small imaginary part of the wavenumber, and according to the sign of this imaginary part, only one solution will be finite and the wavenumber is given by

$$\begin{aligned} k' &= \frac{\sqrt{2m(E\pm i\eta-U)}}{\hbar}=\frac{\sqrt{2m(E-U)}}{\hbar}\sqrt{1\pm\frac{i\eta}{E-U}} \\ k' &\approx \frac{\sqrt{2m(E-U)}}{\hbar}\left[1\pm\frac{i\eta}{2(E-U)}\right]\equiv k(1\pm i\delta) \end{aligned} \tag{2.9}$$

2.1. EIGENFUNCTION EXPANSION

For any structure, if the eigenfunctions of the Hamiltonian operator are available, the Green's function [79] can be obtained as

$$G^r(x,x')=\sum_\alpha\frac{\psi_\alpha(x)\psi_\alpha^*(x')}{E-\varepsilon_\alpha+i\eta},\ \text{where } H_{\text{op}}\psi_\alpha(x)=\varepsilon_\alpha\psi_\alpha(x) \tag{2.10}$$

Equation (2.10) can be derived easily by knowing that the eigenfunctions of the Hamiltonian form a complete orthonormal set of states and hence the Green's function can be expanded in the form

$$G^r(x,x')=\sum_\alpha C_\alpha(x')\psi_\alpha(x),\ \text{where } \int\psi_\beta^*(x)\psi_\alpha(x)dx=\delta_{\beta\alpha} \tag{2.11}$$

By substituting (2.11) into (2.10) we get

$$\left[E-H_{\text{op}}+i\eta\right]G^r(x,x')=\sum_\alpha(E-\varepsilon_\alpha+i\eta)C_\alpha\psi_\alpha(x)=\delta(x-x') \tag{2.12}$$

Multiplying both sides of (2.12) by $\psi_\alpha^*(x)$ and integrating we get

$$C_\alpha = \frac{\psi_\alpha^*(x')}{E - \varepsilon_\alpha + i\eta} \tag{2.13}$$

and by substituting back in (2.11) we get the definition of the retarded Green's function using the eigenfunctions expansion defined in (2.10).

2.2. ZERO TEMPERATURE GREEN'S FUNCTIONS

The zero temperature Green's function, using the language of second quantization and field operators is defined as [80]

$$G(\lambda, t-t') = -i\left\langle \left| TC_\lambda(t)C_\lambda^\dagger(t') \right| \right\rangle \tag{2.14}$$

where T is the time order operator that arranges the operators with the earlier time to the right, the quantum number λ can be anything depending on the problem of interest and for example, it can be taken as the quantum number of the free electron gas $\lambda = (\mathrm{k}, \sigma)$ as k is the wavevector and σ is the spin, $C_\lambda^\dagger(t')$ is the creation operator that creates an excitation at the state λ at the time t' and $C_\lambda(t)$ is the annihilator operator that destroys the excitation at the state λ at the time t. At zero temperature, the only state that can be occupied is the ground state, so the bra $\langle|$ and ket $|\rangle$ in (2.14) represent the average over the ground state of the system. The time evolution of the creation or annihilation operators are given in the Heisenberg picture and are given by

$$C_\lambda(t) = e^{iHt} C_\lambda e^{-iHt} \text{ and } C_\lambda^\dagger(t) = e^{iHt} C_\lambda^\dagger e^{-iHt} \tag{2.15}$$

where H is the total Hamiltonian of the system including interactions and the Hamiltonian can be written as $H = H_0 + V$. The non-interacting part of the Hamiltonian H_0 is simple and can be diagonalized and its eigenstates can be obtained. The interaction part V is usually complex and so the eigenstates of H are not easy to obtain. C_λ and $C_\lambda^\dagger$ are defined in terms of a complete set of eigenstates of the non-interacting Hamiltonian H_0 whose eigenstates are known.

For the simple form of the Green's function where there is no interaction, $H = H_0$, λ will be an eigenstate to H and $H|\rangle = \varepsilon_0|\rangle$ and $HC_\lambda^\dagger|\rangle = \varepsilon_\lambda C_\lambda^\dagger|\rangle$. Then, the Green's function will have the simple exponential time dependence

$$G(\lambda, t > t') = -i\left\langle \left| C_\lambda(t) C_\lambda^\dagger(t') \right| \right\rangle = -i \exp\left[-i(t-t')(\varepsilon_\lambda - \varepsilon_0)\right] \tag{2.16}$$

The Green's function in the energy representation is obtained by the Fourier transform of the Green's function in the time domain and is given by

$$G(\lambda, E) = \int_{-\infty}^{\infty} dt e^{iEt} G(\lambda, t) = -i \int_0^{\infty} dt e^{i(E-(\varepsilon_\lambda - \varepsilon_0)+i\delta)t} = \frac{1}{E-(\varepsilon_\lambda - \varepsilon_0)+i\delta} \tag{2.17}$$

where a small infinitesimal imaginary part was added to the energy for the integration to converge. In the real situation, where the interactions exist, λ is not an eigenstate to the Hamiltonian and the particle in the state λ gets scattered, shifted in energy during the interval $(t-t')$. The magnitude of the Green's function at a later time t will not be unity as in the case of non-interaction, but it will have a smaller value due to the decay of the state. To correctly calculate the Green's function, the average should be done on the ground state of the total Hamiltonian H and not the ground state of the non-interacting Hamiltonian H_0. An S-matrix operator method can be used to relate the two ground states to each other. The idea is that at $t = -\infty$ the system is assumed to be in the non-interacting state where the ground state is $|\rangle_0$, the ground state of H_0, and after the interaction is switched on, the state at $t = 0$ becomes the ground state of H. So the S-matrix operator brings the ground state of the non-interacting Hamiltonian from $-\infty$ to the current moment where it becomes the ground state of the total Hamiltonian

$$|\rangle = S(0, -\infty)|\rangle_0 \text{ and } \langle| = {}_0\langle|S(\infty, 0) \tag{2.18}$$

Equation (2.18) means that the ground state at a very far time in the future is assumed to be back to the ground state of the non-interacting Hamiltonian after the interaction is switched off. Using the S matrix expansion, it can be shown that the Green's function defined in (2.14) can be written as [80]

$$G(\lambda, t-t') = -i \frac{{}_0\langle | T\hat{C}_\lambda(t)\hat{C}_\lambda^\dagger(t')S(\infty,-\infty) | \rangle_0}{{}_0\langle | TS(\infty,-\infty) | \rangle_0} \tag{2.19}$$

In this definition of the Green's function, the field operators are defined in the interaction picture and not the Heisenberg picture and are given by

$$\hat{C}_\lambda(t) = e^{iH_0 t} C_\lambda e^{-iH_0 t} \text{ and } \hat{C}_\lambda^\dagger(t) = e^{iH_0 t} C_\lambda^\dagger e^{-iH_0 t} \tag{2.20}$$

So, both of the field operator and ground states are related to the non-interacting Hamiltonian. The time order operator T in the numerator will order the operator from the earlier to the later starting from the right to the left, such that if $t > t'$, the sequence will be $S(t',-\infty)$, $\hat{C}_\lambda^\dagger(t')$, $S(t,t')$, $\hat{C}_\lambda(t)$, $S(\infty,t)$. When the interaction V=0, then the S-matrix $S(\infty,-\infty) = 1$, and the non-interacting, or sometime called the free propagator Green's function, is then simplified to

$$G_0(\lambda, t-t') = -i\, {}_0\langle | T\hat{C}_\lambda(t)\hat{C}_\lambda^\dagger(t') | \rangle_0 \tag{2.21}$$

The S matrix is related to the interacting Hamiltonian V in the interaction picture and is given by [80]

$$\begin{aligned} &S(t,t') = T\exp\left[-i\int_{t'}^{t} dt_1 \hat{V}(t_1)\right] \text{ and} \\ &S(t,t) = 1,\ S^\dagger(t,t') = S(t',t),\ S(t,t')S(t',t'') = S(t,t'') \end{aligned} \tag{2.22}$$

and T is the time order operator. The last form of the scattering matrix using the time order operator is compact and its solution can be obtained by some diagrammatic techniques like Feynman diagrams that can be used to calculate some terms of the expansion according to the level of approximation required [80]. By expanding the S-matrix $S(\infty,-\infty)$ in (2.19) and applying The Wick's theorem as shown in [80], we obtain the Dyson equation which is shown here below in energy representation by taking the Fourier transform of both sides:

$$G(\lambda, E) = G_0(\lambda, E) + G_0(\lambda, E)\Sigma(\lambda, E)G(\lambda, E) \tag{2.23}$$

and $\Sigma(\lambda, E)$ is the self-energy due to interaction.

2.3. MATSUBARA GREEN'S FUNCTIONS

At nonzero temperature, other states can be occupied in addition to the ground state. The Green's function should be calculated using a statistical average over all possible configurations of the system weighted by the thermodynamic factor $e^{-\beta H}$ and $\beta = 1/KT$. The Green's function is then defined as [80]

$$G(\lambda, t-t') = \frac{\mathrm{Tr}\left[e^{-\beta H} C_\lambda(t) C_\lambda^\dagger(t')\right]}{\mathrm{Tr}\left[e^{-\beta H}\right]} \tag{2.24}$$

where the $\mathrm{Tr} \equiv \sum_n \langle n | \cdots | n \rangle$ over all possible states n. The total Hamiltonian including interactions appear in two different places in this definition of the Green's function in (2.24). It appears in the thermodynamic factor $e^{-\beta H}$ and in the $e^{\pm iHt}$ in the operator definition $C_\lambda(t) = e^{iHt} C_\lambda e^{-iHt}$. So instead of using two S-matrix expansions in order to express the time evolution and the thermodynamic factor with respect to the non-interacting Hamiltonian, the time t and β can be considered as the imaginary and real parts of a complex variable, which is known as Matsubara technique. Thus, only one S-matrix is required and the Green's function can be written as [80]

$$G(\lambda, \tau-\tau') = -\left\langle \left| T_\tau C_\lambda(\tau) C_\lambda^\dagger(\tau') \right| \right\rangle = -\frac{\mathrm{Tr}\left[e^{-\beta H} T_\tau e^{\tau H} C_\lambda e^{-(\tau-\tau')H} C_\lambda^\dagger e^{-\tau' H}\right]}{\mathrm{Tr}\left[e^{-\beta H}\right]} \tag{2.25}$$

where $\tau = it$, $C_\lambda(\tau) = e^{\tau H} C_\lambda e^{-\tau H}$ and T_τ is a τ - ordering operator that arranges operators with the earliest τ closest to $-\beta$ to the right. Using the cyclic properties of the trace, the Green's function can be shown, as in [80], to be periodic in τ such that

$$G(\lambda, \tau) = -G(\lambda, \tau + \beta) \tag{2.26}$$

and then it can be expanded in a Fourier series

$$G(\lambda, i\omega_n) = \int_0^\beta d\tau e^{i\omega_n \tau} G(\lambda, \tau) \tag{2.27}$$

where $i\omega_n$ is an odd multiple of π/β. Using the S-matrix expansion to use the non-interacting Hamiltonian instead of the total Hamiltonian, we end up with the Dyson equation which is shown here in the energy representations:

$$G(\lambda, i\omega_n) = G_0(\lambda, i\omega_n) + G_0(\lambda, i\omega_n)\Sigma(\lambda, i\omega_n)G(\lambda, i\omega_n) \tag{2.28}$$

where $G_0(\lambda, i\omega_n)$ is the energy representation of the free propagator Green's function $G_0(\lambda,\tau) = -\left\langle \left| T_\tau \hat{C}_\lambda(\tau)\hat{C}_\lambda^\dagger(0) \right| \right\rangle_0$ and $\hat{C}_\lambda(\tau) = e^{\tau H_0} C_\lambda e^{-\tau H_0}$.

The advantage of the Matsubara Green's function is that it gives a simpler way to get the retarded Green's function in both zero and nonzero temperature, as the S-matrix expansion is simpler in the Matsubara method than in the real time method. So it can be used to calculate some measurable equilibrium quantities such as the conductivity or the susceptibility.

2.4. NON-EQUILIBRIUM GREEN'S FUNCTIONS

At non-equilibrium conditions, the temperature of the system is not defined and so the thermodynamic average over all possible states cannot be done as shown before for equilibrium Green's function. Thus, the starting point by calculating the Matsubara Green's function to get from it the retarded Green's function is not suitable. In fact, real time calculations have to be used when dealing with systems out of equilibrium. In equilibrium, the S-matrix $S(\infty, -\infty)$ is constructed such that the system is in the non-interacting states at $t = -\infty$. The interaction is switched on and off again and eventually the system goes back to be in the non-interacting states at $t = \infty$. At non-equilibrium, actually the system is not expected to go back to the non-interacting state after a long time. Instead, Schwinger (1961) suggested a different way of handling the asymptotic behavior at $t = \infty$ [80, 81]. The time integral starts at $t = -\infty$ until a moment $t = \tau$ and after that it starts from τ and goes back to $-\infty$ again and eventually $\tau \to \infty$ as shown in Fig. 2-1. So, the start and the end points of the contour is at $-\infty$ and then the system can be in the non-interacting states at the two ends of the contour.

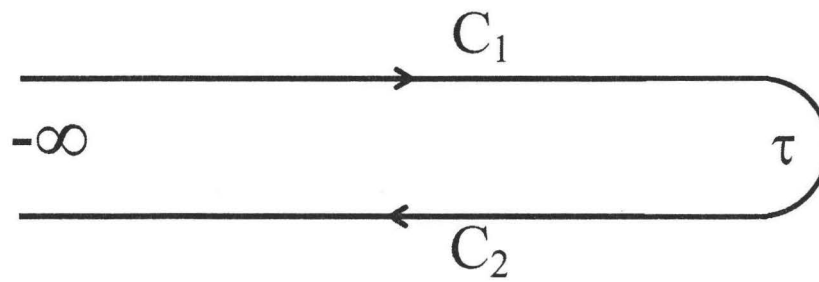

Figure 2-1 – The contour integration path.

The S-matrix defined in the contour shown above will be from $-\infty$ to $-\infty$ and using the contour time order operator, it is given by

$$S_C = S(-\infty,-\infty) = T_C \exp\left[-i\int_C dt\hat{V}(t)\right] \tag{2.29}$$

The contour time-order operator arranges the operators with the earliest time to the right. So, the time evolves from $-\infty$ to τ through C_1 and then from τ to $-\infty$ through the C_2. The contour Green's function in the space representation is given by

$$G(1,1') = -i\left\langle T_C\left[\psi_H(1)\psi_H^{\dagger}(1')\right]\right\rangle \tag{2.30}$$

where $(1) \equiv (r_1,t_1)$ and ψ_H and $\psi_H^{\dagger}$ are the field operators defined in the Heisenberg picture and the total Hamiltonian of the non-equilibrium system can be divided as

$$H = h + H'(t) \text{ and } h = H_0 + H_i \tag{2.31}$$

The total Hamiltonian consists of an equilibrium and time independent part h, which can be divided into a non-interacting and simple part H_0, and another part due to interaction H_i, and a non-equilibrium and time dependent Hamiltonian $H'(t)$ like an external applied bias, for example. The non-equilibrium part is assumed to be zero before a specific time $t < t_0$ and $t_0 \to -\infty$ for steady-state problems where the transient response is not important. In order to define the

Green's function in terms of the non-interacting equilibrium part of the Hamiltonian as done before, two S-matrix expansions are needed. The first one is to express the time evolution according to h instead of H and another S-matrix expansion is needed to write the time evolution with respect to H_0 instead of h. The transformation is complicated and as shown in [94] is given by

$$G(1,1') = -i\frac{\mathrm{Tr}\left\{\rho_0 T_C\left[S_C^i S_C^{'} \psi_{H_0}(1)\psi_{H_0}^{\dagger}(1')\right]\right\}}{\mathrm{Tr}\left[\rho_0 T_C\left(S_C^i S_C^{'}\right)\right]} \text{ and } \psi_{H_0}(t) = e^{iH_0 t}\psi(0)e^{-iH_0 t} \tag{2.32}$$

The thermodynamic function ρ_0 and the two contour S-matrices S_C^i and $S_C^{'}$ are given by

$$\begin{aligned}
\rho_0 &= \frac{\exp(-\beta H_0)}{\mathrm{Tr}\left[\exp(-\beta H_0)\right]} \\
S_C^{'} &= \exp\left[-i\int_C dt H_{H_0}^{'}(t)\right], \text{ and } H_{H_0}^{'}(t) = e^{iH_0 t}H^{'}(0)e^{-iH_0 t} \\
S_C^{i} &= \exp\left[-i\int_C dt H_{H_0}^{i}(t)\right], \text{ and } H_{H_0}^{i}(t) = e^{iH_0 t}H^{i}(0)e^{-iH_0 t}
\end{aligned} \tag{2.33}$$

The previous definition of the contour Green's function seems complicated but it is exact and all the time dependences are governed by the non-interacting Hamiltonian. The contour Green's function has similar definition as the equilibrium Green's function and hence it can be expanded using the S-matrix expansion and applying the Wick's theorem to get the Dyson equation. According to the positions of the times t_1 and t_2 on the contour defined in Fig. 2-1, four different Green's functions can be obtained as follows [80, 83]

$$G(1,1') = \begin{cases} G^t(1,1') & t_1, t_1^{'} \in C_1 \\ G^{>}(1,1') & t_1 \in C_2,\ t_1^{'} \in C_1 \\ G^{<}(1,1') & t_1 \in C_1,\ t_1^{'} \in C_2 \\ G^{\tilde{t}}(1,1') & t_1, t_1^{'} \in C_2 \end{cases} \tag{2.34}$$

The Green's functions are called the time-ordered, the greater, the lesser, and the antitime-ordered respectively. Using the field operators in the Heisenberg picture, the four Green's function are given by

$$\begin{aligned} G^{t}(1,1') &= -i\theta(t_1 - t_1')\left\langle \psi_H(1)\psi_H^{\dagger}(1')\right\rangle + i\theta(t_1' - t_1)\left\langle \psi_H^{\dagger}(1')\psi_H(1)\right\rangle \\ G^{>}(1,1') &= +i\left\langle \psi_H(1)\psi_H^{\dagger}(1')\right\rangle \\ G^{<}(1,1') &= -i\left\langle \psi_H^{\dagger}(1')\psi_H(1)\right\rangle \\ G^{\tilde{t}}(1,1') &= -i\theta(t_1' - t_1)\left\langle \psi_H(1)\psi_H^{\dagger}(1')\right\rangle + i\theta(t_1 - t_1')\left\langle \psi_H^{\dagger}(1')\psi_H(1)\right\rangle \end{aligned} \tag{2.35}$$

Two other Green's functions can be derived from the previous four Green's functions and although they are not independent, defining them simplifies the equations and they are used directly to calculate some physical properties. These Green's functions are called the retarded and advanced Green's functions and they are given by [80]

$$\begin{aligned} G^{r}(1,1') &= -i\theta(t_1 - t_1')\left\langle \left\{\psi_H(1),\psi_H^{\dagger}(1')\right\}\right\rangle \\ &= G^{t}(1,1') - G^{<}(1,1') = G^{>}(1,1') - G^{\tilde{t}}(1,1') \\ G^{a}(1,1') &= i\theta(t_1' - t_1)\left\langle \left\{\psi_H(1),\psi_H^{\dagger}(1')\right\}\right\rangle \\ &= G^{t}(1,1') - G^{>}(1,1') = G^{<}(1,1') - G^{\tilde{t}}(1,1') \end{aligned} \tag{2.36}$$

A Dyson equation of the contour Green's function defined in (2.32) by expanding the S-matrices and applying the Wick's theorem can be obtained, and by using the four Green's functions shown above, the Dyson equation can be put in a matrix form derived by Keldysh (1965) [80, 83]

$$\tilde{G} = \tilde{G}_0 + \tilde{G}_0 \tilde{\Sigma} \tilde{G} \tag{(2.37)}$$

where the matrices for the four the Green's functions and interaction self-energy functions are given by

$$\tilde{G} = \begin{bmatrix} G^{t} & -G^{<} \\ G^{>} & -G^{\tilde{t}} \end{bmatrix}, \quad \tilde{\Sigma} = \begin{bmatrix} \Sigma^{t} & -\Sigma^{<} \\ \Sigma^{>} & -\Sigma^{\tilde{t}} \end{bmatrix} \tag{(2.38)}$$

The general definition of the four free propagator Green's functions matrix $\tilde{G}_0$ is given by

$$G_0(1,1') = -i\frac{\mathrm{Tr}\left\{\rho_0 T_C\left[\psi_{H_0}(1)\psi^{\dagger}_{H_0}(1')\right]\right\}}{\mathrm{Tr}\left[\rho_0\right]} = -i\mathrm{Tr}\left\{\rho_0 T_C\left[\psi_{H_0}(1)\psi^{\dagger}_{H_0}(1')\right]\right\} \tag{2.39}$$

and according to the potions of t_1 and t_2 on the contour, the four free propagator Green's function can be obtained from the previous general definition.

2.4.1. LANGRETH THEOREM

In order to resolve the Dyson matrix equation to get the retarded and lesser Green's function and their relation to each other and to the self-energy functions, the Langreth theorem gives a simple way to do that using the analytic continuation rules. The rule can be explained by this simple example. For a contour integration given as,

$$C(t_1,t_1') = \int_C dt A(t_1,t)B(t,t_1'), \tag{(2.40)}$$

if t_1 is in the upper half of the contour, while t_2 is in the lower half, then C is a lesser function. The contour can be split into two parts and the integration can be done in the real time integration as shown in [94] such that

$$C^{<}(t_1,t_1') = \int_{-\infty}^{\infty} dt\left[A^{r}(t_1,t)B^{<}(t,t_1') + A^{<}(t_1,t)B^{a}(t,t_1')\right], \tag{2.41}$$

and in a matrix form: $C^{<} = (AB)^{<} = A^{r}B^{<} + A^{<}B^{a}$

If t_2 is in the upper half of the contour, while t_1 is in the lower half, then C is a greater function. The greater function in a similar way for the contour integration defined in (2.40) is given in the matrix form as

$$C^{>} = (AB)^{>} = A^{r}B^{>} + A^{>}B^{a} \tag{2.42}$$

The retarded function can be obtained from the lesser and greater function as

$$C^r(t_1,t_1') = \theta(t_1 - t_1')\left[C^>(t_1,t_1') - C^<(t_1,t_1')\right] = \int_{t_1'}^{t_1} dt\left[A^r(t_1,t)B^r(t,t_1')\right], \quad (2.43)$$

or $C^r = (AB)^r = A^r B^r$

In the previous example, A and/or B can be a multiplication of two functions. By applying these simple rules, The retarded and lesser Green's functions can be obtained from the generic Dyson equation $G = G_0 + G_0 \Sigma G$.

2.4.2. DYSON EQUATION

The kinetic equation that governs the dynamics of the Green's function is the Dyson equation [80]

$$\left\{i\frac{\partial}{\partial t_1} - \left[-\frac{\hbar^2}{2m}\nabla_1^2 + U(r_1)\right]\right\} G(r_1,r_2;t_1-t_2) = \delta(1-2) + \iint \Sigma(r_1,r;t_1-t)G(r,r_2;t-t_2)dtdr \quad (2.44)$$

The dependence on the time difference for both the Green's function and the self-energy $(t_1 - t_2)$ is for steady state response. The Fourier transform to (2.44) gives

$$\left[E - H_{op}\right]G(r_1,r_2;E) = \delta(r_1 - r_2) + \iint \Sigma(r_1,r;E)G(r,r_2;E)dr$$
$$H_{op} = -\frac{\hbar^2}{2m}\nabla_1^2 + U(r_1) \quad (2.45)$$

In Equation (2.45), the Hamiltonian in the L.H.S is the free or the non-interacting Hamiltonian while all sources of interactions are included in the self-energy in the R.H.S. Equation (2.45) can be written in a simplified matrix form, where a matrix multiplication can be used instead of integration over the internal variables

$$[EI - H]G = I + \Sigma G \quad (2.46)$$

The Dyson equation can be put in another form which is useful to get the different forms of Green's function. By multiplying both sides of (2.46) by $[EI - H]^{-1}$, we get

$$\begin{aligned} G &= g + g\Sigma G \\ \text{and } g &= \left[EI - H\right]^{-1} \end{aligned} \tag{2.47}$$

where g is the Green's function of the system without including interactions. The last form of the Dyson equation, it is known also by Keldysh formulation, is generic and using Langreth theorem and the analytic continuation rules, different forms of Green's function can be obtained such as the retarded, advanced, less than, greater than, time ordered and anti time ordered Green's functions.

2.4.3. KINETIC EQUATION

The Dyson equation mentioned above can be used to get the retarded and lesser Green's functions and get the relation between them which is called the kinetic equation. Applying the analytic continuation rules on (2.47) we get

$$G^r = g^r + \left(g\Sigma G\right)^r = g^r + g^r \Sigma^r G^r \tag{2.48}$$

and so

$$\begin{aligned} \left[g^r\right]^{-1} G^r &= I + \Sigma^r G^r \\ G^r &= \left[\left[g^r\right]^{-1} - \Sigma^r\right]^{-1} = \left[EI - H - \Sigma^r\right]^{-1} \end{aligned} \tag{2.49}$$

The less than Green's function can be obtained from (2.47) by applying the analytic continuation rules

$$\begin{aligned} G^< &= g^< + \left(g\Sigma G\right)^< = g^< + g^r \left(\Sigma G\right)^< + g^< \left(\Sigma G\right)^a \\ &= g^< + g^r \Sigma^r G^< + g^r \Sigma^< G^a + g^< \Sigma^a G^a \end{aligned} \tag{2.50}$$

The function $g^<$ represents the initial occupation of the device before coupling with the surrounding leads. It can be set to zero as the steady-state occupation of the device cannot depend on the initial occupation. It can be proved that $g^<$ equal zero as shown in [94].

Multiplying both sides of (2.50), after setting $g^< = 0$, by $\left[g^r\right]^{-1}$, we get

$$\left[g^r\right]^{-1} G^< = \Sigma^r G^< + \Sigma^< G^a \tag{2.51}$$

and so

$$\begin{aligned} \left[\left[g^r\right]^{-1} - \Sigma^r\right] G^< &= \Sigma^< G^a \\ \left[EI - H - \Sigma^r\right] G^< &= \Sigma^< G^a \end{aligned} \tag{2.52}$$

The kinetic equation relating the lesser and the retarded Green's function is then given by

$$G^< = G^r \Sigma^< G^a \tag{2.53}$$

2.4.4. REPLACING THE LEADS BY SELF-ENERGY

The retarded Green's function for a conductor connected to a semi-infinite lead contact as shown in Fig. 2-2 is given by

$$G^r = \left[(E + i\eta) - H\right]^{-1} \tag{2.54}$$

where H is the total Hamiltonian representing the conductor and the lead. The isolated conductor, with no coupling with any surrounding contacts, is H_C and the Hamiltonian of the isolated semi-infinite lead is H_p.

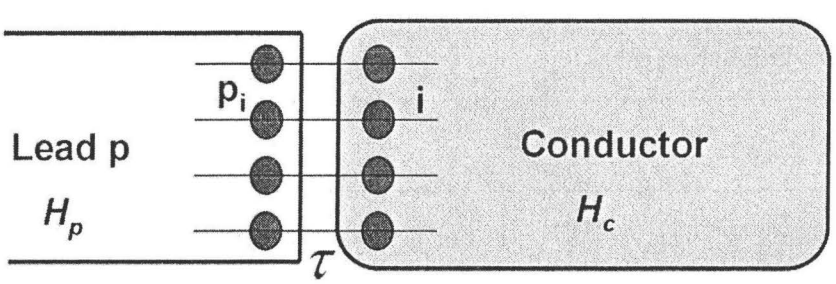

Figure 2-2 – A conductor in contact with a contact lead

Equation (2.54) can be rewritten in sub matrices and is given by

$$\begin{bmatrix} G_p & G_{pc} \\ G_{cp} & G_c \end{bmatrix} = \begin{bmatrix} (E + i\eta)I - H_p & \tau \\ \tau & EI - H_c \end{bmatrix}^{-1} \tag{2.55}$$

where τ is the coupling matrix whose elements are zero except at the interface points $\tau(p_i, i) = t$. By solving equation (2.55) as shown in [79], we end up with

$$G_c = \left[EI - H_c - \Sigma^r_{\text{lead}} \right]^{-1}, \text{ where } \Sigma^r_{\text{lead}} = \tau^\dagger g^r_p \tau$$
$$g^r_p = \left[(E + i\eta) I - H_p \right]^{-1} \tag{2.56}$$

Although the dimensions of the matrices to be inverted to get the retarded Green's function inside the conductor taking into consideration the coupling with the leads is finite due to the small size of the conductor, the dimensions of the matrix H_p, the Hamiltonian of the semi-infinite lead is still infinite. Thus it needs to be inverted to get the Green's function of the lead used to calculate the self-energy. So, the reduction in size obtained by replacing the leads by self-energy and so get smaller matrices to be inverted to get the Green's function does not help much unless the Green's function in the semi-infinite lead can be calculated analytically. In most cases, the lead can be approximated in simple shapes and the Green's function of it is easy to get. Then the numerical solution is needed to solve for the Green's function in the conductor which has a complicated potential profile and cannot be solved analytically. The self-energy is complex, so the real part shifts the energy eigenvalues, while the imaginary part is proportional to the decay rate of the states, whether by being lost in the leads or scattered to a different state.

2.4.5. SELF-ENERGY

The retarded self-energy is a non-Hermitian Hamiltonian that describes the effect of coupling with the leads or internal interactions within the device on the electron dynamics.

2.4.5.1. Interactions with leads

As shown in the previous section, the leads can be replaced by a self-energy $\Sigma^r_{\text{lead}} = \tau^\dagger g^r_p \tau$ and g^r_p is the retarded Green's function of the isolated semi-infinite lead and. For a 1D problem the retarded Green's function of the lead and the corresponding self-energy is given by [79]

$$g^r_p(x = x' = a) = -\frac{1}{t} e^{ika} \text{ and } \Sigma^r_{\text{lead}} = \tau^\dagger g^r_p \tau = -t\, e^{ika}$$
$$E = U + 2t(1 - \cos(ka)) \tag{2.57}$$

In equation (2.57), the Green's function of the lead is calculated at one lattice point from the interface with the conductor, where zero boundary condition is assumed for the isolated lead. For 2D semi-infinite lead as shown in Fig. 2-3, the Green's function and the corresponding self-energy are given by [79]

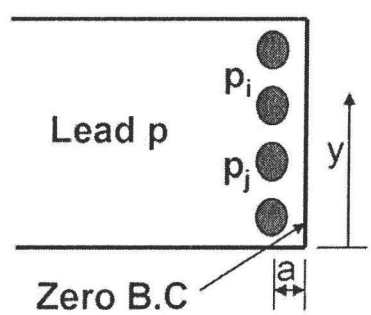

Figure 2-3 – Schematic of 2D semi-infinite lead

$$g^r_p(a; p_i, p_j) = -\frac{1}{t}\sum_m \chi_m(p_i) \exp[ik_m a] \chi_m(p_j)$$
$$\Sigma^r_{\text{lead}} = \tau^\dagger g^r_p \tau \Rightarrow \Sigma^r_{\text{lead}}(i,j) = -t\sum_m \chi_m(p_i) \exp[ik_m a] \chi_m(p_j) \tag{2.58}$$

The transverse wavefunction χ_m appearing in the Green's function and self-energy satisfies the eigenvalue problem:

$$\left[-\frac{\hbar^2}{2m}\frac{\partial^2}{\partial y^2} + U(y)\right]\chi_m(y) = \varepsilon_m \chi_m(y) \tag{2.59}$$

and the dispersion relation is now given by

$$E - \varepsilon_m = 2t(1 - \cos(k_m a)) \tag{2.60}$$

The in-scattering and out-scattering self-energy functions due to the coupling with leads can be obtained from the retarded self-energy assuming that the leads are in thermal equilibrium with a specific Fermi function. The total transition rate or the decay rate of state due to interactions is related to the retarded self-energy such that:

$$\Gamma_{\text{lead}} = i\left[\Sigma^{r}_{\text{lead}} - \Sigma^{a}_{\text{lead}}\right] = \Sigma^{<}_{\text{lead}} + \Sigma^{>}_{\text{lead}} \tag{2.61}$$

The decay rate of a state equals twice the imaginary part of the retarded self-energy. This decay rate of a state equals the summation of the in-scattering and out-scattering rates from and to the leads. The reason that the decay rate equals the summation of the in-scattering and out-scattering rate and not only the out-scattering rate is that the new incoming electrons from the lead will be blocked by the current electron occupying the state, but this interaction already contributes to the decay of the state. The state remains evolving without decay as long as no thing happens that disturbs the coherence and causes the state to decay whether by the loss in the leads or the scattering to a new state. The in-scattering and out-scattering are related to the total transition rates by the Fermi function of the thermal equilibrium lead and are given by

$$\begin{aligned} \Sigma^{<}_{\text{lead}}(E) &= f(E)\Gamma_{\text{lead}}(E) \\ \Sigma^{>}_{\text{lead}}(E) &= (1 - f(E))\Gamma_{\text{lead}}(E) \end{aligned} \tag{2.62}$$

2.4.5.2. Internal interactions

The internal interactions such as electron-electron and electron-phonon interactions affect the dynamics of electrons inside the device through the self-energy term. The imaginary part of the self-energy gives the rate of decay of a state due to the scattering occurring by the interactions within the device. The electron-electron interaction in the Hartree-Fock approximation does not give rise to energy transitions through in-scattering or out-scattering processes, so the

while P means the principal part of the integral. The previous relation between the real and imaginary part of the retarded self-energy is to have a causal function such that when we take the Fourier transform to get the function in time domain, it becomes proportional to the time step function and so vanishes for times less than zero and in time domain the retarded self-energy is $\Sigma_{\varphi}^{r}(t) \sim \vartheta(t)\Gamma_{\varphi}(t)$.

2.5. GREEN'S FUNCTIONS APPLICATIONS

Calculations of the Green's functions are very useful for device modeling. The retarded Green's function allows us to describe the electrons while they are inside the device and it can be used to calculate the wavefunctions for open boundary conditions. The transmission function of electrons through the device can be expressed in terms of the retarded Green's function. The correlation or the lesser Green's function is a generalized density matrix and from which the probability of states occupancy and the phase correlation between different states are known. The correlation function is important to calculate the current in the non-coherent transport regime. Usually in most cases, a numerical solution is needed to calculate the kinetic equation describing the retarded or the correlation Green's functions as obtaining analytical solutions are very hard for a complicated potential profile of the device.

2.5.1. TIGHT BINDING MODEL (FINITE DIFFERENCES)

To solve a differential equation like (2.6), a common way is to discretize the spatial coordinate such that the Green's function becomes a matrix:

$$G^{r}(x,x') \rightarrow G^{r}(i,j) \text{ where } i,j \text{ denote points in a discrete lattice} \qquad (2.71)$$

The differential equation becomes a matrix equation

$$\left[(E+i\eta)I - H\right]G^{r} = I \qquad (2.72)$$

where $[I]$ is the identity matrix and $[H]$ is the matrix representation of the Hamiltonian operator H_{op}. So, from this matrix equation, the retarded Green's

function equals $\left[(E+i\eta)I-H\right]^{-1}$. One way to discretize the Hamiltonian operator and to get the matrix H is the method of finite differences or the tight binding model.

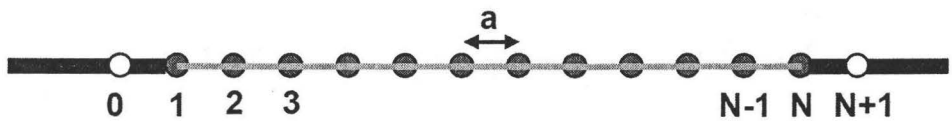

Figure 2-4 – Discrete lattice space

For 1D problem with zero magnetic vector potential, the Hamiltonian operator in (2.4) can be discretized as follows:

$$\left[H_{\text{op}}F\right]_{x=ja}=\left[-\frac{\hbar^2}{2m}\frac{\mathrm{d}^2F}{\mathrm{d}x^2}\right]_{x=ja}+U_jF_j \tag{2.73}$$

where a is the lattice constant and the second derivative can be expressed as

$$\left[\frac{\mathrm{d}^2F}{\mathrm{d}x^2}\right]_{x=ja}=\frac{1}{a}\left\{\left[\frac{\mathrm{d}F}{\mathrm{d}x}\right]_{x=(j+1/2)a}-\left[\frac{\mathrm{d}F}{\mathrm{d}x}\right]_{x=(j-1/2)a}\right\}=\frac{1}{a^2}\left\{F_{j+1}-2F_j+F_{j-1}\right\}$$

So (2.73) can be written as

$$\left[H_{\text{op}}F\right]_{x=ja}=(U_j+2t)F_j-tF_{j-1}-tF_{j+1} \tag{2.74}$$

where $t=\hbar^2/2ma^2$ and is called the hopping matrix element or the overlap integral between neighboring sites, while the term (U_j+2t) represents the energy of the localized orbital. So the matrix representation of the 1D Hamiltonian in (2.74) can be shown in the matrix form

$$H=\begin{bmatrix} \ldots & -t & 0 & 0 & 0 \\ -t & \mathrm{U}_{-1}+2t & -t & 0 & 0 \\ 0 & -t & \mathrm{U}_0+2t & -t & 0 \\ 0 & 0 & -t & \mathrm{U}_1+2t & -t \\ 0 & 0 & 0 & -t & \ldots \end{bmatrix} \tag{2.75}$$

This can be used to calculate the Green's function matrix in (2.72).

2.5.1.1. Dispersion relation

For a free electron moving in a constant potential in 1D space, the wave function is a plane wave and the relation between energy the wavenumber is a parabolic dispersion relation [96]:

$$\Psi_k(x) = \exp[ikx] \text{ where } E = U + \frac{\hbar^2 k^2}{2m} \tag{2.76}$$

In a discrete space, the Schrödinger equation can be written as

$$E\psi_j = (U + 2t)\psi_j - t\psi_{j-1} - t\psi_{j+1} \text{ satisfied by } \psi_j = \exp[ikx_j] \tag{2.77}$$

provided that

$$E = U + 2t(1 - \cos(ka)) \tag{2.78}$$

The parabolic dispersion relation in (2.76) is modified to (2.78) in discrete space and the possible values of energy in the discrete space $E \le U + 4t$. The velocity is then given by

$$\hbar v = \frac{\partial E}{\partial k} = 2at \sin(ka) \tag{2.79}$$

At the limit $a \to 0$, we recover back the parabolic dispersion relation and the velocity $v = \hbar k / m$

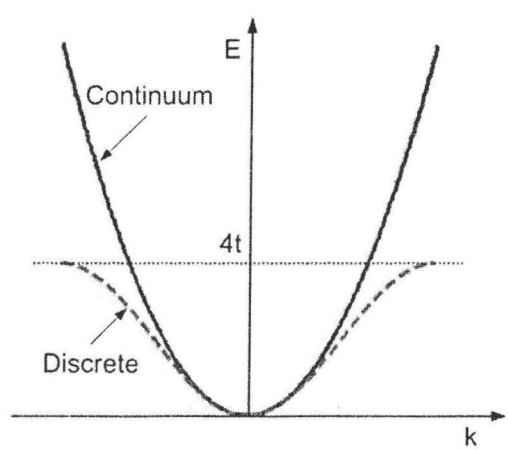

Figure 2-5 – Dispersion relation between E and k in both continuum and discrete space

2.5.2. WAVEFUNCTIONS CALCULATIONS

For 1D time independent Schrödinger equation

$$\frac{-\hbar^2}{2m}\frac{d^2\psi(x)}{dx^2}+U(x)\psi(x)=E\psi(x) \tag{2.80}$$

Using the discrete space shown in Fig. 2-4, the discrete wavefunction satisfies the difference equation

$$\left[-t\psi_{i-1}+(2t+U_i)\psi_i-t\psi_{i+1}\right]=E\psi_i \text{ and } i=1,2,3,...,N \tag{2.81}$$

To solve (2.81), the boundary conditions at $i = 0$ and $i = N + 1$ should be specified.

2.5.2.1. Eigenvalue problem

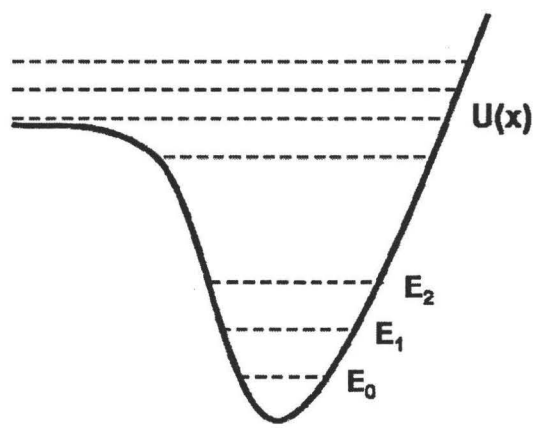

Figure 2-6 – Potential energy profile of bound system

For zero boundary conditions where the wavefunction vanishes at the boundaries for a closed system as shown in Fig. 2-6, the energy eigenvalues and the corresponding wavefunctions are obtained by solving the eigenvalue problem

$$H\psi=E\psi \Rightarrow \begin{bmatrix} U_1+2t & -t & 0 & \cdots & 0 \\ -t & \ddots & & & \vdots \\ 0 & -t & U_i+2t & -t & 0 \\ \vdots & & & \ddots & -t \\ 0 & \cdots & 0 & -t & U_N+2t \end{bmatrix}\begin{bmatrix} \psi_1 \\ \vdots \\ \psi_i \\ \vdots \\ \psi_N \end{bmatrix}=E\begin{bmatrix} \psi_1 \\ \vdots \\ \psi_i \\ \vdots \\ \psi_N \end{bmatrix} \tag{2.82}$$

2.5.2.2. Open boundary conditions

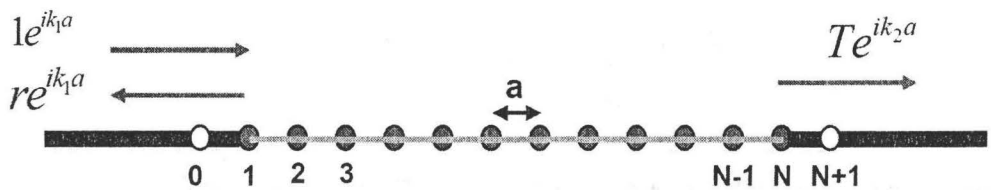

Figure 2-7 – Device in contact with leads in discrete space

When the device is in contact with leads, the system is not confined and the energy states become continuum. Assuming incident, reflected and transmitted plane waves at the contact interfaces as shown in Fig. 2-7, the discrete wave equation near the left contact at (i=1) is given by

$$E\Psi_1 - \left[-t\Psi_0 + (2t + U_1)\Psi_1 - t\Psi_2\right] = 0 \qquad (i = 1) \tag{2.83}$$

In equation (2.83), Ψ_0 is the value of the wavefunction inside the contact. By applying that the wavefunction at the interface point should be continuous, we can get (2.83) expressed as only wavefunctions inside the device. The wavefunction inside the left contact can be expressed as $\Psi(x) = 1e^{ik_1x} + re^{-ik_1x} \quad x \le 0$. Equating the wavefunctions of the device and leads at the interface points we get

$$\begin{aligned} \Psi(x=0) &= \Psi_1 = 1 + r \\ \Psi(x=-a) &= \Psi_0 = e^{-ik_1a} + re^{ik_1a} \end{aligned} \tag{2.84}$$

From (2.84), $\Psi_0 = \Psi_1 e^{ik_1a} - (e^{ik_1a} - e^{-ik_1a})$, and so equation (2.83) can be expressed in terms of wavefunctions inside the device as

$$E\Psi_1 - \left[\left(2t + U_1 - te^{ik_1a}\right)\Psi_1 - t\Psi_2\right] = t(e^{ik_1a} - e^{-ik_1a}) \qquad (i = 1) \tag{2.85}$$

The effect of the coupling with the left lead appeared through adding a self-energy term $-te^{ik_1a}$ to the device first point (i=1), and instead of having zero in the R.H.S, we have the broadening term $t(e^{ik_1a} - e^{-ik_1a})$ which is the excitation term. The self-energy due to coupling with the right lead can be obtained in the same way.

Figure 2.8 shows the added self-energy terms due to the coupling with the left and right lead contacts in addition to the excitation term in the R.H.S arise from the wave incident from the left lead.

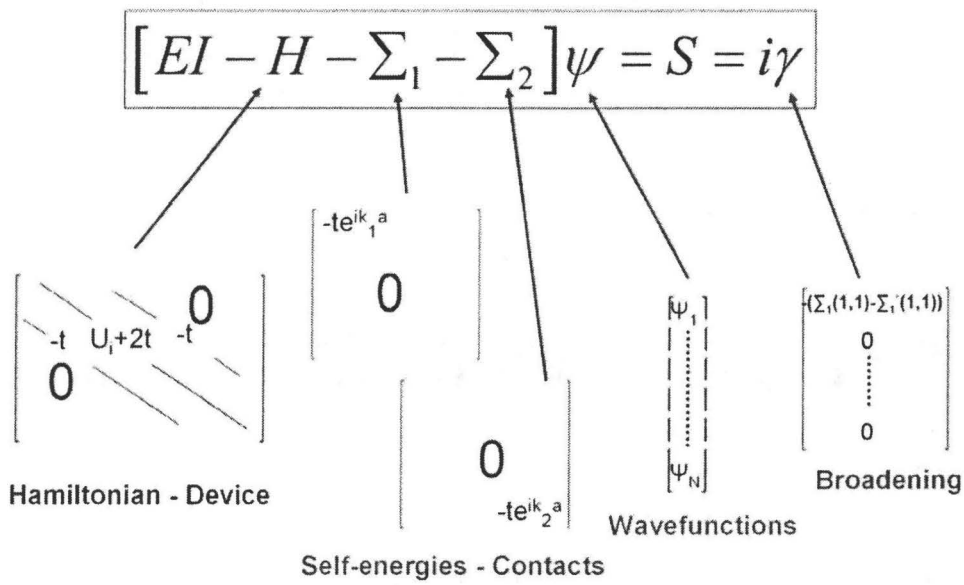

Figure 2-8 – Self-energy terms and excitation term to express the effect of lead coupling

The wavefunction can be calculated from the Green's function as

$$\psi = [EI - H - \Sigma_1 - \Sigma_2]^{-1} S = G^r S \tag{2.86}$$

At every energy value, the self-energies at the left and right contacts are calculated. The broadening or the excitation term in the R.H.S is obtained from the self-energy. The wavefunction at specific energy is then obtained by multiplying the Green's function matrix times the excitation vector. The discrete dispersion relation between the energy and the wavevector is used to get the values of the wavevector and hence to calculate the self-energies.

2.5.3. TRANMISSION FUNCTION

After calculating the retarded Green's function of the device, including the coupling effect with the contact leads, it can be used to calculate the elements of the scattering matrix and from which the transmission function can be obtained.

The transmission function between two contact leads p and q through a device can be obtained in terms of the retarded and advanced Green's function as [79]

$$T_{p\to q}(E) = \mathrm{Tr}\left[\Gamma_p G^r_{pq} \Gamma_q G^a_{pq}\right] \tag{2.87}$$

The Green's function in (2.87) gives the dynamics of the electrons inside the device taking into consideration the effect of the leads and is given by

$$G^r = \left[E\,I - H\, - \Sigma^r_p - \Sigma^r_q\right]^{-1} \quad \text{and} \quad \Sigma^r_{p,q} = -t.e^{ika} \tag{2.88}$$

and Γ_p and Γ_q represent the coupling of the device with the leads and are given by

$$\Gamma_{p,q} = i(\Sigma^r_{p,q} - \Sigma^a_{p,q}) = 2t\sin(ka) \tag{2.89}$$

and the dispersion relation is given by

$$E\ = 2t(1-\cos(ka)) \tag{2.90}$$

2.5.4. CURRENT CALCULATIONS

The terminal current per unit energy from the contact lead p to the device in terms of the correlation Green's functions, the lesser and the greater, and the in-scattering and out-scattering self-energy functions is given by [79]

$$i_p(E) = \frac{e}{h}\mathrm{Tr}\left[\Sigma^<_p G^> - \Sigma^>_p G^<\right] \tag{2.91}$$

The in-scattering rate from the lead p to an empty state in the device is given by $\Sigma^<_p$ and $G^>$ gives the probably of a state to be unoccupied. So, the term $\Sigma^<_p G^>$ gives the in-scattering flow of electrons going from the lead p to the device, while the $\Sigma^>_p G^<$ gives the out-scattering flow of electrons from the device to the lead p. The difference of the two terms gives the net current per unit energy flowing from the lead p to the device. The integration of $i_p(E)$ over all energy values gives the terminal current. The internal interactions inside the device, which leads to a change in the energy and phase of electrons, can be modeled as if

the device is connected to an external virtual prop (reservoir) such that the device and the virtual reservoir exchange electrons where the energy channels of electrons are changed and the electrons phases are randomized. A schematic of particles exchange between a device and a reservoir is shown in Fig. 2-9.

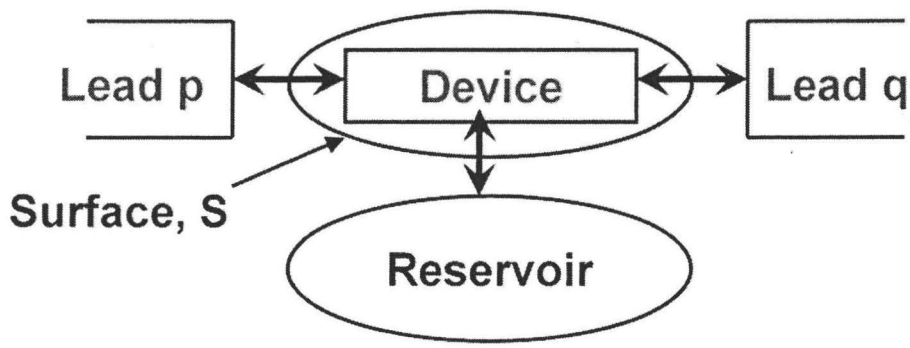

Figure 2-9 – Non-coherent transport is viewed as exchange of particles between the device and a reservoir where the energy and phase of electrons are changed

The flow of electrons into this reservoir is given in a similar formula as the one of the terminal current and is called the vertical current:

$$i_{\varphi}(E)=\frac{e}{h}\mathrm{Tr}\left[\Sigma_{\varphi}^{<}G^{>}-\Sigma_{\varphi}^{>}G^{<}\right] \tag{2.92}$$

where $\Sigma_{\varphi}^{<}$ and $\Sigma_{\varphi}^{>}$ are in-scattering and out-scattering self-energy functions from and to the reservoir, respectively. There is no net loss or gain of particles from the device, but what happens is that electrons leave the device to the reservoir with a specific value of energy and are re-injected back with a different energy value. So, the vertical current may have some positive values for some energy channels and some negative values for other channels and the net current after integration over all energy channels should give $\int i_{\varphi}(E)dE=0$. Although the integration over all energy channels of the vertical current gives zero, but it does not equal zero at every energy channel unless there are no interactions. The interactions affect the terminal current through $G^{>}$ and $G^{<}$ as the correlation functions depend on the in-scattering and out-scattering self-energy functions which can be from coupling

with leads or internal interactions. Assuming they are independent, they can be written as

$$\Sigma^{<} = \Sigma_{\varphi}^{<} + \sum_{p} \Sigma_{p}^{<} \text{ and } \Sigma^{>} = \Sigma_{\varphi}^{>} + \sum_{p} \Sigma_{p}^{>} \tag{2.93}$$

and

$$G^{<} = G^{r}\Sigma^{<}G^{a} \text{ and } G^{>} = G^{r}\Sigma^{>}G^{a} \tag{2.94}$$

Equation (2.91) can be written as

$$i_p(E) = \frac{e}{h}\mathrm{Tr}\left[\Sigma_p^{<}G^{>} + \Sigma_p^{<}G^{<} - \Sigma_p^{<}G^{<} - \Sigma_p^{>}G^{<}\right] = \frac{e}{h}\mathrm{Tr}\left[\Sigma_p^{<}A - \Gamma_p G^{<}\right] \tag{2.95}$$

and by writing the scattering function as

$$\Sigma^{<} = \Sigma_{\varphi}^{<} + \sum_{q} \Sigma_{q}^{<} \text{ and } \Gamma = \Gamma_{\varphi} + \sum_{q} \Sigma_{q}^{>} \tag{2.96}$$

The total terminal current can be separated into two components, coherent from leads and non-coherent from interactions

$$\begin{aligned} \left[i_p\right]_{\text{coherent}} &= \frac{e}{h}\sum_{q}\mathrm{Tr}\left[\Sigma_p^{<}G^{r}\Gamma_q G^{a} - \Gamma_p G^{r}\Sigma_q^{>}G^{a}\right] \\ \left[i_p\right]_{\text{non-coherent}} &= \frac{e}{h}\mathrm{Tr}\left[\Sigma_p^{<}G^{r}\Gamma_{\varphi}G^{a} - \Gamma_p G^{r}\Sigma_{\varphi}^{>}G^{a}\right] \end{aligned} \tag{2.97}$$

If $\Sigma_{\varphi}^{>}$ and $\Sigma_{\varphi}^{<}$ are zero at the case when we do not have electron-phonon or electron-photon interactions, then the transport is coherent and the formula is simplified to the Landauer-Buttiker formalism. For equilibrium contacts, the in-scattering and out-scattering functions are given by

$$\Sigma_p^{<} = f_p\Gamma_p \text{ and } \Sigma_p^{>} = \left(1 - f_p\right)\Gamma_p \tag{2.98}$$

where f_p is the Fermi function in lead p and by substituting back in (2.97), we get

$$\left[i_p\right]_{\text{coherent}} = \frac{e}{h}\sum_{q}\mathrm{Tr}\left[\Gamma_p G^{r}\Gamma_q G^{a}\right]\left(f_p - f_q\right) = \frac{e}{h}\sum_{q}T_{pq}\left(f_p - f_q\right) \tag{2.99}$$

So, for coherent transport the current formula is simplified to the Landauer-Buttiker formalism and the Green's function is then used to calculate the transmission function.

CHAPTER 3 QDIPS DENSITY OF STATES MODELING

QDIPs can be used to detect infrared light in the mid- and far-infrared (3-25 μm) through the intersubband transitions in the conduction band of the quantum dots. Both of the bound-to-bound and bound-to-continuum transitions can be used for detection. In order to obtain the operating wavelengths corresponding to these transitions, the positions of the quantum dot energy levels relative to the quantum dot conduction band edge should be obtained. A theoretical model based on Green's function has been used to calculate the spectral function and the density of states (DOS) of the quantum dot [76]. The kinetic equation that governs the Green's functions is solved numerically using the method of finite differences [79]. The model considers the microscopic device structure including the shape and size of QDs and the device heterostructure. From the calculated density of states, all possible energy transitions can be obtained, and hence, the corresponding operating wavelengths for intersubband transitions are determined. The model has been applied to three different QDIP structures which are quantum dot-in-a-well detector QDWELL, resonant tunneling (RT) QDIP and superlattice (SL) QDIP [75] and good agreement with experimental data has been found.

3.1. GREEN'S FUNCTION MODEL

The method of Green's function is used to calculate the spectral function or the localized density of states (DOS) of the quantum dots. The spectral function can be integrated over an arbitrary selected volume enclosing one quantum dot to get the DOS or the number of states per unit energy inside this the arbitrary

selected volume. The DOS gives the positions of the discrete energy levels inside the QD in addition to the continuum spectrum of states outside the QD. Thus from the DOS, the positions of the discrete energy levels relative to the continuum states are known and so all possible intersubband transitions bound-to-bound or bound-to-continuum are obtained; thus the operating wavelengths for both transitions are determined. The retarded Green's function of the system in cylindrical representation is given by [79, 80, and 96]

$$\left[E - H_{\text{op}}\right] G^r(r,r';\theta,\theta';z,z') = \frac{1}{r}\delta(r-r')\delta(\theta-\theta')\delta(z-z'), \tag{3.1}$$

where E is the total energy of electron and H_{op}, the Hamiltonian operator of the system, is given by

$$H_{\text{op}} = \frac{-\hbar^2}{2}\left(\frac{1}{r}\frac{\partial}{\partial r}\frac{r}{m^r(r,z)}\frac{\partial}{\partial r} + \frac{1}{m^r(r,z)}\frac{1}{r^2}\frac{\partial^2}{\partial\theta^2} + \frac{\partial}{\partial z}\frac{1}{m^z(r,z)}\frac{\partial}{\partial z}\right) + V(r,\theta,z) \tag{3.2}$$

where $V(r,\theta,z)$ is the potential energy seen by the electron, m^r and m^z are the in-plane and out-of-plane effective masses, respectively. If the potential energy of the QD has an azimuthal symmetry around the z-axis, which is the case for cylindrical and conical shape QDs, the potential energy is not a function of θ, thus the z-component of the angular momentum and the Hamiltonian commute, and hence, the Green's function can be written as

$$G^r(r,r';\theta,\theta';z,z';E) = \frac{1}{2\pi}\sum_n e^{in(\theta-\theta')} G_n^r(r,r';z,z';E), \; n \text{ is an integer.} \tag{3.3}$$

The diagonal elements of the spectral function [79] is given by

$$A(r,z;E) = -2\,\text{Im}\left[G^r(r,r;\theta,\theta;z,z;E)\right] = -\frac{1}{\pi}\sum_n \text{Im}\left[G_n^r(r,r;z,z;E)\right]. \tag{3.4}$$

The density of states, which is the number of states per unit energy, is obtained from the spectral function and is given by

$$D(E) = \frac{1}{2\pi}\mathrm{Tr}\left[A(r,z;E)\right] = \frac{1}{2\pi}\int 2\pi r dr dz\ A(r,z;E)\,. \tag{3.5}$$

The trace or the integration is done over an arbitrary cylindrical volume enclosing the QD. This model will be applied to three different QDIP structures to calculate the DOS and from which the discrete and continuum energy levels can be obtained. The intersubband transitions obtained by the model are compared with the available experimental responsivity of the detectors and good matching is obtained. The details of how to apply the model to obtain the DOS will be given for the DWELL structure and then the results of the models will be given for the other two structures

3.2. QUANTUM DOT-IN-A WELL MODELING

The quantum dots-in-a-well (DWELL) detector is a hybrid between the conventional quantum well and the emerging quantum dot detectors. The DWELL detectors are advantageous over quantum well and quantum dot photodetectors in that they can detect light at precise wavelengths since their detection is based on bound-to-bound rather than bound-to-continuum transitions. Moreover, they demonstrate normal incidence operation and low dark current [45]. The nature of the potential profiles of these detectors makes the theoretical modeling challenging. Different approaches have been used in the literature for theoretical modeling of pyramidal, cylindrical and hemispherical quantum dots [97-101]. A theoretical model of pyramidal-shaped InAs quantum dots placed in an InGaAs quantum well, which is buried in a GaAs matrix, is shown in [72]. The model of the DWELL is based on a Bessel function expansion of the wave function. The model can estimate the ground state of the quantum dot. For the higher states in the quantum well, the model has to be modified to account for the free motion of electrons perpendicular to the growth direction.

The DWELL detector grown by molecular beam epitaxy, reported in [45], consists of a ten-period active region of 6 nm $In_{0.15}Ga_{0.85}As$, 2.4 monolayers (ML) of InAs, 6 nm $In_{0.15}Ga_{0.85}As$, and 49 nm of GaAs, as shown in Fig. 3-1.

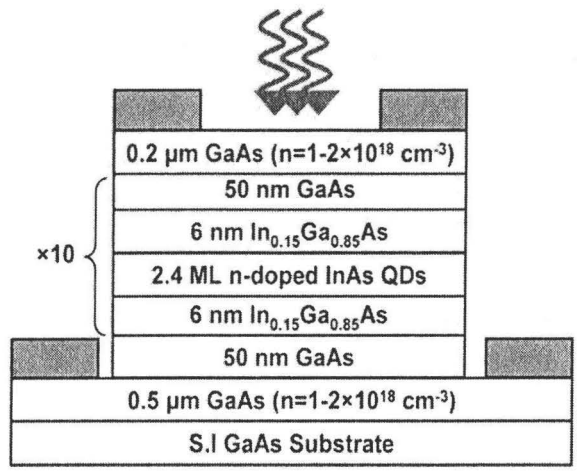

Figure 3-1 – Schematic of a 10-layer InAs/InGaAs QDWELL [45].

The TEM image of the DWELL heterostructure is shown in Fig. 3-2 [72]. The darkest region is the InAs quantum dot. The quantum dot is placed in $In_{0.15}Ga_{0.85}As$ quantum well which is surrounded by the GaAs region, as shown in Fig. 3-2. The image shows that the quantum dots are positioned in the top half of the quantum well and have a pyramidal shape with base dimension of 11 nm and height of 6.5 nm.

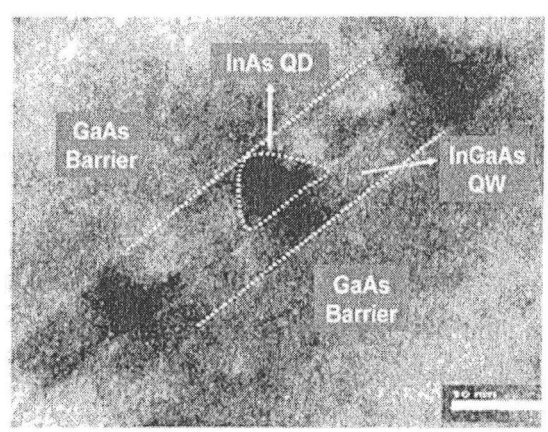

Figure 3-2 – Cross-section TEM image of a single QD layer of the DWELL [72].

From the information of the TEM image, a schematic for the potential profile of the DWELL can be defined as shown in Fig. 3-3. The potential profile has a cylindrical symmetry about the z-axis and consists of a conical shaped InAs quantum dot with a diameter of 11 nm and height of 6.5 nm placed in the top half of an 11 nm quantum well. There is 2.4 ML (~ 0.5 nm) of InAs (wetting layer) between the first half of the quantum well and the quantum dot. The numerical method used to get the energy spectrum of the DWELL is described in [45, 72]. The approach is to enclose the region that contains the quantum dot by a cylinder of radius R and height Z_C where the wavefunctions are forced to vanish on the surface. The structure is shown in Fig. 3-3. The coupling between quantum dots is neglected and the cluster inside the cylinder is treated as isolated. The ground state of the quantum dot is confined inside the quantum dot and vanishes outside, so it can be estimated fairly well by this model. However, for the higher states, especially those in the quantum well, the electron has no confinement in the lateral direction perpendicular to the z-axis, so the zero boundary condition on the cylindrical surface has to be changed.

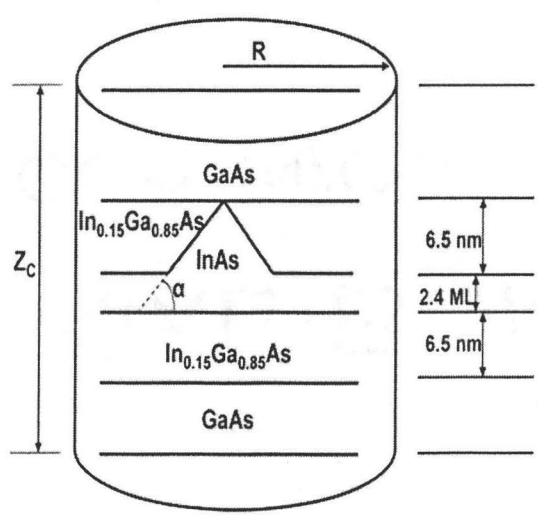

Figure 3-3 – Schematic of the DWELL structure to be used to formulate potential profile.

To get the potential profile, the band offset between the different materials in the structure must be known. The conduction band offset between InAs and GaAs is about 60% of their band gap difference [102, 103]. The calculated band offset used in [72] is 477 meV between InAs and $In_{0.15}Ga_{0.85}As$ and 93 meV between $In_{0.15}Ga_{0.85}As$ and GaAs. The zero level is chosen to be the conduction band edge of the $In_{0.15}Ga_{0.85}As$. The band offset profile is shown in Fig. 3-4. Using the conduction band offsets between the different heterostructure material and the schematic of the cylindrical volume enclosing one QD, the potential energy profile of electrons in the conduction band is shown in Fig. 3-5.

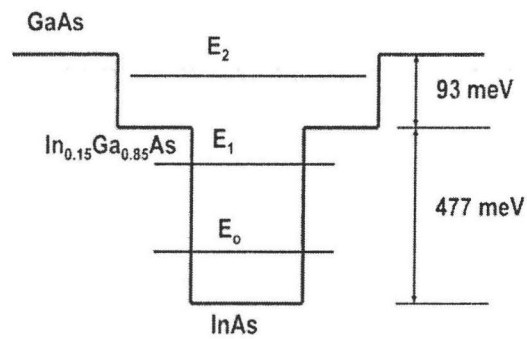

Figure 3-4 – Conduction band offsets and the energy levels of the QDWELL.

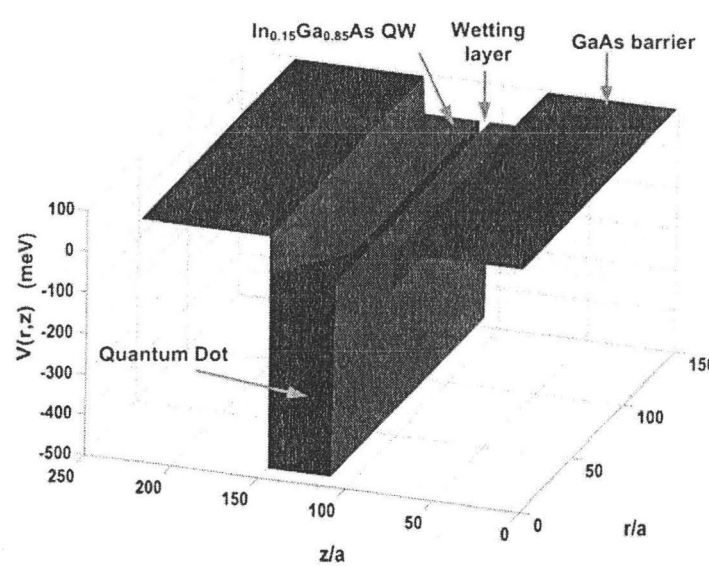

Figure 3-5 – Potential energy profile used by the model plotted as a function of r and z [76].

It represents the variation in the conduction band offsets between the different materials in space. It is drawn in a plane passing through the axis of the cylinder shown in Fig. 3-3, where r varies from 0 to R and z varies from 0 to Z_C. The figure shows the InAs quantum dot and wetting layer, the InGaAs quantum well and the GaAs barrier. The variations in effective masses are described in the same way as that used for the potential energy. Since the potential energy is not a function of θ, the Green's function can be defined as in Eq. (3.3), and by substituting Eq. (3.3) into Eq. (3.1) and using $\delta(\theta-\theta') = \sum_n e^{in(\theta-\theta')} / 2\pi$, the problem can be reduced to two dimensions instead of three, and we get

$$\left[E - H_n\right] G_n^r(r,r';z,z') = \frac{1}{r}\delta(r-r')\delta(z-z'), \tag{3.6}$$

where H_n is given by

$$H_n = -\frac{\hbar^2}{2}\left(\frac{1}{r}\frac{\partial}{\partial r}\frac{r}{m^r(r,z)}\frac{\partial}{\partial r} + \frac{1}{m^r(r,z)}\frac{\left(-n^2\right)}{r^2} + \frac{\partial}{\partial z}\frac{1}{m^z(r,z)}\frac{\partial}{\partial z}\right) + V(r,z) \tag{3.7}$$

Equation (3.6) can be solved numerically using the method of finite differences to convert the differential equation into a matrix equation. The Hamiltonian in Eq. (3.6) is transformed to a matrix form by discretizing the space in the r-z plane using a grid with a lattice constant a such that we have N_r points in the r-direction and N_z in z-direction. A schematic of the grid is shown in Fig. 3-6.

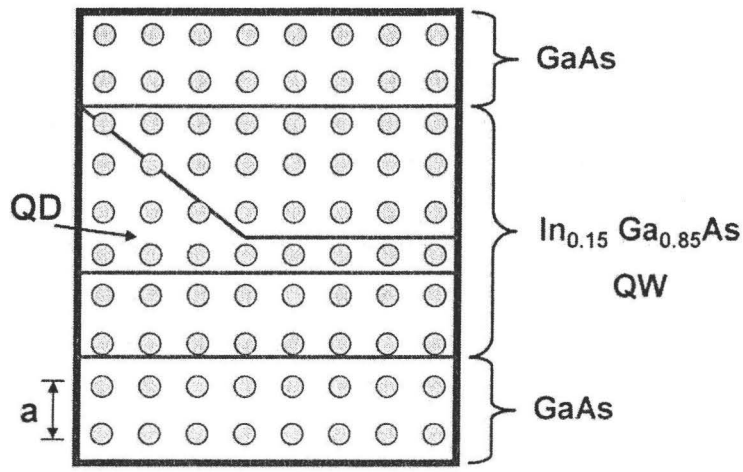

Figure 3-6 – Schematic of the lattice grid in *r*-*z* plane used in the numerical simulation

At every lattice point in the grid shown in Fig. 3-6, the value of the potential energy $V(ia, ja)$, where i and j are integers, are obtained as shown in Fig. 3-5. The effective mass value of electrons at every lattice point in the grid is obtained in the same way. The derivatives with respect to r and z are approximated by finite differences, for example, $(\partial F/\partial z)\big|_i \rightarrow (F_{i+1} - F_i)/a$. The delta functions in the RHS of Eq. (3.6) are transformed to the identity matrix, and the details of the Hamiltonian discretization are shown in appendix A. After discretizing Eq. (3.6), the differential equation is transformed to a matrix equation which is given by

$$[EI - H_n]G_n^r = [r]^{-1}, \tag{3.8}$$

where H_n is the matrix representation of the Hamiltonian operator and its form is given in appendix A, I is the identity matrix and $[r]$ is a diagonal matrix where its diagonal elements take the r component of the total position vector. The matrix H_n has infinite dimensions since it represents the Hamiltonian of the whole system inside and outside the cylinder. By adding appropriate boundary conditions at the cylindrical surface, the size of the matrices can be finite. In order

to truncate the matrix and consider only the Hamiltonian inside the cylinder, we can consider the Hamiltonian inside cylinder as if it were isolated, and then compensate for the coupling to the outside region by adding an additional effective Hamiltonian at the cylinder's surface, to simulate the coupling between the points inside and outside the cylinder. This effective Hamiltonian is not Hermitian, which means it has real and imaginary parts and it is called self-energy. The real part of the self-energy shifts the energy eigenvalues and the imaginary part of it determines the decay rate of the electron state. The matrix representation of the total Hamiltonian and Green's function can be divided into sub-matrices such that [79]

$$\begin{bmatrix} EI - H_{nL} & \tau \\ \tau^{+} & EI - H_{nD} \end{bmatrix} \begin{bmatrix} G_{nL} & G_{nLD} \\ G_{nDL} & G_{nD} \end{bmatrix} = \begin{bmatrix} r_L & 0 \\ 0 & r_D \end{bmatrix}^{-1}, \tag{3.9}$$

where H_{nL} and H_{nD} are the Hamiltonian matrices outside and inside the isolated cylinder, respectively, and τ is the coupling matrix where its elements are zero everywhere except at points adjacent to the interface (L_i, i). For such points, $\tau(L_i, i) = t$ and t is the hopping or tunneling parameter. This concept is described in detail in [79, 104]. Equation (3.9) can be reduced to

$$\left[EI - H_{nD} - \Sigma^{r}\right] G_{nD} = \left[r_D\right]^{-1}, \tag{3.10}$$

where H_{nD} is the matrix representing the Hamiltonian of the isolated cylinder (without coupling) and Σ^{r} is the self-energy term that gives the interaction between the points at the interface inside and outside the cylinder and is given by $\Sigma^{r} = \tau\left[EI - H_{nL}\right]^{-1}\tau^{+}R$, where R is the radius of the cylinder. The self-energy term is obtained from the retarded Green's function outside the cylinder, with zero boundary condition at the cylinder's surface. The retarded Green's function outside the cylinder satisfies Eq. (3.6); however, the potential energy and the effective mass are functions only of z.

Now if we take an average value of the effective mass in the radial part, we can solve for the Green's function analytically by the method of separation of variables. The Hamiltonian outside the cylinder is approximated by

$$H_n = -\frac{\hbar^2}{2}\left(\frac{1}{m_{\text{av}}}\left\{\frac{1}{r}\frac{\partial}{\partial r}r\frac{\partial}{\partial r} - \frac{n^2}{r^2}\right\} + \frac{\partial}{\partial z}\frac{1}{m^z(z)}\frac{\partial}{\partial z}\right) + V(z), \tag{3.11}$$

where m_{av} an average effective mass of the electron and its value is chosen such that it gives the same lowest eigenvalues obtained by solving 1-D problem which has the same potential and effective mass variation in z-direction.

Using the Hamiltonian in Eq. (3.11), the retarded Green's function outside the cylinder with zero boundary condition at r=R, calculated at $r = r' = R + a$ and at specified energy E is given by

$$G^r_{nL} = \begin{cases} \displaystyle\sum_m \left(\chi_m(z)\chi^*_m(z')\frac{2m_{\text{av}}}{\hbar^2}\frac{\pi}{2}\begin{Bmatrix} J_n\left[k_m(R+a)\right]Y_n(k_mR) - \\ J_n(k_mR)Y_n\left[k_m(R+a)\right] \end{Bmatrix} \times \frac{H_n(k_m(R+a))}{H_n(k_mR)} \right), & E > \varepsilon_m \\ \displaystyle\sum_m \left(\chi_m(z)\chi^*_m(z')\frac{2m_{\text{av}}}{\hbar^2}\begin{Bmatrix} K_n\left[k_m(R+a)\right]I_n(k_mR) \\ -K_n(k_mR)I_n\left[k_m(R+a)\right] \end{Bmatrix} \times \frac{K_n(k_m(R+a))}{K_n(k_mR)} \right), & E \le \varepsilon_m \end{cases} \tag{3.12}$$

The details of the calculations are shown in appendix B. In Eq. (3.12), a is the lattice constant of the grid, J_n, Y_n and H_n are the Bessel, Neuman and Hankel functions of order n, respectively, I_n and K_n are the modified Bessel functions of the first and second kinds, respectively, $\chi_m(z)$ and ε_m are the eigenvectors and the corresponding eigenvalues obtained by numerically solving the eigenvalue problem

$$\left[-\frac{\hbar^2}{2}\left(\frac{\partial}{\partial z}\frac{1}{m^*(z)}\frac{\partial}{\partial z}\right)+V(z)\right]\chi_m(z)=\varepsilon_m\chi_m(z), \tag{3.13}$$

and assuming zero boundary condition at $z=0$ and $z=Z_c$, and k_m is related to the energy of electron by the dispersion relation [79, 96] given by

$$E=\varepsilon_m+2t(1-\cos(k_m a)). \tag{3.14}$$

Equation (3.14) is the modified version of the parabolic dispersion relation between E and k due to discretization and t is the tunneling or the hopping parameter given by $t=\left(\hbar^2/2m_{av}a^2\right)$. The self-energy is related to the Green's function in Eq. (3.12) by the relation

$$\Sigma^r=\tau\left[EI-H_{nL}\right]^{-1}\tau^+R=aRt^2G_{nL}. \tag{3.15}$$

The self-energy matrix is zero everywhere except at the points of interface where we have coupling between the inner and outer points at $r=R$. The lattice constant a appeared in Eq. (3.15) is used since the Green's function G_{nL}, solved analytically in Eq. (3.12), is for a continuum semi-infinite lead and is used to calculate the self-energy in the discrete space to give the correct result when using the matrix multiplication instead of doing integration over the intermediate variables. By substituting Eq. (3.15) into Eq. (3.10), we can get the retarded Green's function inside the cylinder by doing a matrix inversion at certain values of E and n. The height of the cylinder is taken to be 44 nm while the radius of the cylinder is 30 nm. The grid step is 0.2 nm, and hence the matrix dimensions are 33000×33000. The spectral function is calculated from Eq. (3.4). The series converges and for the energy ranges used in the calculations, the first 10 terms in the series corresponding to n=0, 1, 2,..., 9 are enough to produce the required DOS for both the discrete and continuum part of the spectrum near the top of the potential barrier surrounding the QDs. The contributions to the DOS from the terms corresponding to negative values of n are equal the ones corresponding to

the positive values due to the Hamiltonian degeneracy with respect to n. Therefore, there is no need for further calculations of the negative terms and instead the terms corresponding to positive values of n are multiplied by 2. The measured responsivity of the QDWELL of a sample having pyramidal quantum dots with 11 nm for the base and 6.5 nm for the height is shown in Fig. 3-7. The resulting three-color response has peaks at wavelengths 5, 10 and 25 μm. The corresponding energy transitions ΔE due to photon absorption at these wavelengths are ~ 250, 124 and 50 meV.

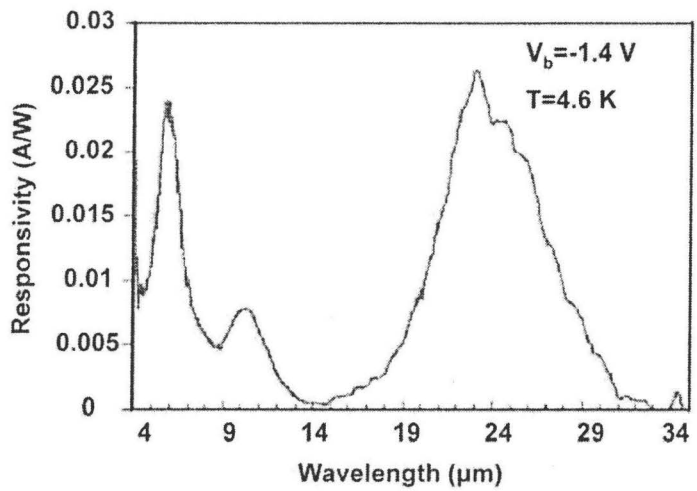

Figure 3-7 – The measured multicolor responsivity of the QDWELL [45].

To interpret the appearance of these peaks (Fig. 3-7) at these wavelengths in the responsivity curve, we need to calculate the density of states of the QDWELL. The matrix representation of the spectral function can be used to obtain the density of states such that $D(E) = \sum_{i=1}^{N_r} \sum_{j=1}^{N_z} ai \times A(ai, aj; E)$. The calculated density of states of the DWELL is shown in Fig. 3-8. From the density of states shown in Fig. 3-8, we notice three quantized levels of the DWELL - E_o, E_1 and E_2 at the energy values -178, -60 and 65 meV, respectively. The sharp peak at E=-178 meV is due to the ground state of the quantum dot and the electron is completely confined inside the quantum dot. There are no more quantized levels

inside the quantum dot as seen in the density of states for these quantum dot dimensions. For quantum dots with larger lateral area, such as the ones obtained by growing InAs on GaAs, the quantum dot has a base of ~20 nm and a height of ~3 nm, and so more than one quantized level can be found inside the quantum dot as shown in [105]. The two quantized levels E_1 and E_2 are in the InAs wetting layer and in the InGaAs quantum well, respectively. They appeared in the density of states as two steps of constant values, as expected when the electron is confined in one dimension and free to move in the other two dimensions. Due to the quantum dot potential, the two steps have some deformation and we get a peak at energy E = -60 meV.

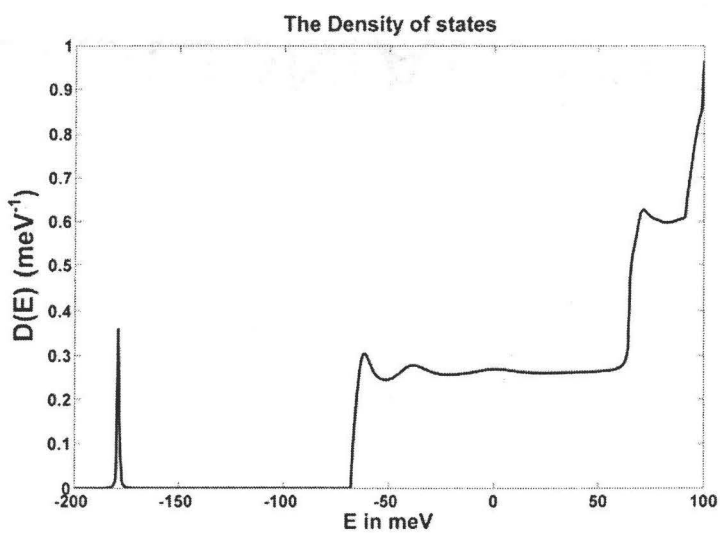

Figure 3-8 – The density of states of the QDWELL [76].

In Figure (3-8), the increase in the density of states for $E > 93$ is due to the continuum states above the quantum well. The density of states for $E > 93$ meV should vary as $E^{1/2}$, as the electron is free above the quantum well. When the spectral function was calculated for $E < -60$ meV, an infinitesimal imaginary part was added to the energy in Eq. (3.10) such that $E \rightarrow E + i\eta$. The addition of this small imaginary part is necessary because the self-energy term has only a real part for these energy values, and to do the matrix inversion we have to remove the

singularities at the values of energies which are equal to the eigenvalues of the Hamiltonian. However, we do not need to worry about that for E>-60 meV since the self-energy has already an imaginary part.

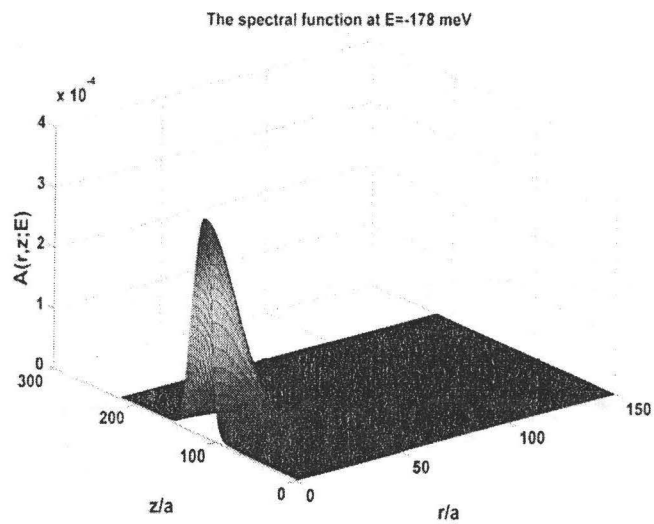

Figure 3-9 – The spectral function at the ground state in the QD at $E = E_o$ [76].

The transition between the ground state in the quantum dot E_o to the second excited state E_2 gives $\Delta E = 243$ meV. So, it is expected to have a peak in the responsivity at (λ=5 μm, ΔE=250 meV). The peak at (λ=10 μm, ΔE=125 meV) can be interpreted as the transition between E_o and E_1 which gives ΔE=118 meV or the transition between E_1 and E_2 which gives ΔE=125 meV. The peak appeared at the long wavelength (λ=25 μm, ΔE=50 meV) and has width from λ=19 μm to 29 μm can be due to the transition between the level of the quantum well at E_2 and the continuum states since the difference between this level and the top of the quantum well is around 30 meV.

The spectral function calculated at the energy values E=-178, -60 and 65 meV are shown in Figures 3-9, 3-10 and 3-11. It is shown that for the ground state of the quantum dot, the electron is completely confined inside the quantum dot as the spectral function is non-zero in the QD region and almost zero elsewhere. For the peak at E=-60 meV, corresponding to the energy level localized in the wetting

layer, the electron is mostly confined in the wetting layer outside the quantum dot. For the energy E=65 meV, the electron is confined in the quantum well which shows that the energy level lies inside the quantum well as expected.

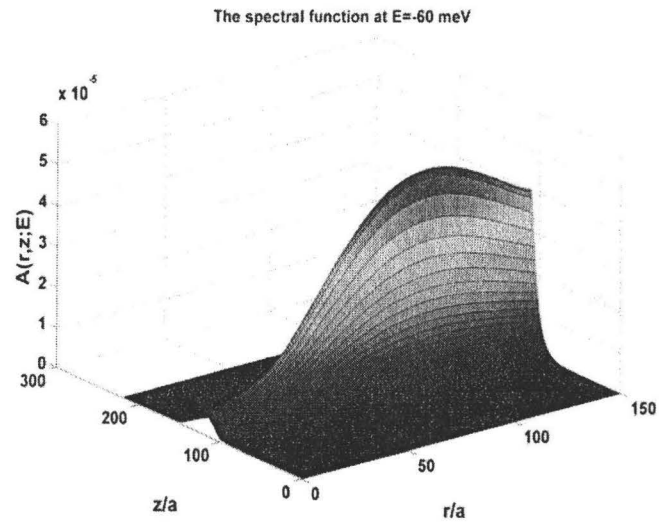

Figure 3-10 – The spectral function at E= E_1 [76].

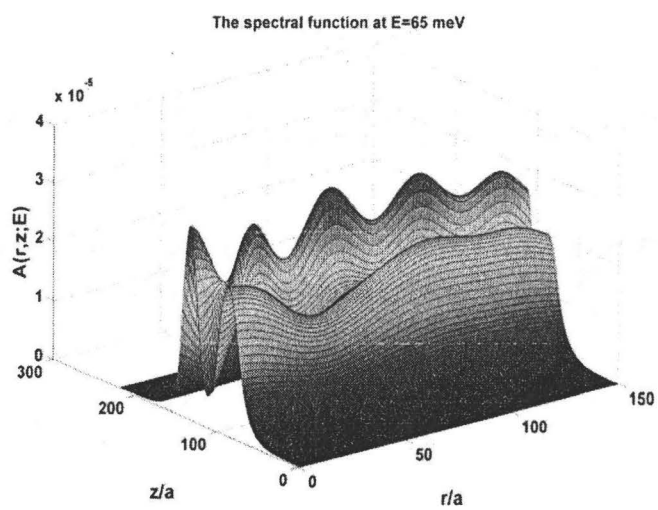

Figure 3-11 – The spectral function at E= E_2 [76].

3.3. RESONANT TUNELLING (RT) QDIP

The RT-QDIP grown by molecular beam epitaxy, reported in [47, 48], is schematically shown in Fig. 3-12. It consists of a ten-period active region, where each period contains a double barrier structure formed by a 4 nm layer of $In_{0.1}Ga_{0.9}As$ surrounded by a 3 nm layer of $Al_{0.3}Ga_{0.7}As$, 1 nm GaAs layer for surface smoothing, 6 MLs $In_{0.4}Ga_{0.6}As$ for quantum dots formation, 4 nm GaAs and finally 4 nm $Al_{0.1}Ga_{0.9}As$ barrier layer. The growth of the 4 nm barrier layer of $Al_{0.1}Ga_{0.9}As$ opposite to the double barrier structure forms a quantum well that creates a well-defined quasi-bound final state for the photoexcited electrons. The double barrier and the quantum well are designed such that the ground state energy levels in both of them coincide. The eigenfunctions in the double barrier and the quantum well overlap and hence the corresponding energy level split allows for resonant tunneling through the structure. The shape and size of individual quantum dots, as observed from high-resolution images of transmission electron microscopy [51, 106], are pyramidal with a base dimension of ~ 25 nm and height of ~6 nm. Measured values of dark current of the RT-QDIP is as low as 1.6×10^{-8} A/cm^2 at 80 K and 1.55 A/cm^2 at 300 K for 1V applied bias have been reported [47] which is very low compared to other QDIP structures. The double barrier is designed such that the resonant level inside the double barrier coincides with the energy of the photoexcited carriers and hence enhances the photocurrent transport across the structure. Thus, the dark current is reduced since the thermally excited carriers have a broad energy distribution where the transmission probability across the double barrier is low. The calculated energy levels in the quantum dot of the resonant tunneling QDIP using the eight-band **k.P** model estimated an energy separation between the ground state of the quantum dot and the resonant energy level in the quantum well as ΔE=161 meV [47]. However, it is expected that this energy separation is larger since the observed peak at λ=6 μm in the responsivity curve corresponds to an energy transition ΔE=206 meV [24]. It is estimated from the model developed in this chapter that the energy of the ground

state in the QDs is -178 meV while the energy of the resonant levels in the quantum well are 15 and 30 meV, as shown in Fig. 3-12. Therefore, the center of the peak in the responsivity is estimated to be due to ΔE~200 meV which is in a good agreement with ΔE=206 meV observed experimentally. The responsivity of the detectors can be qualitatively understood from the information provided by the density of states which gives an insight about the possible energy transitions.

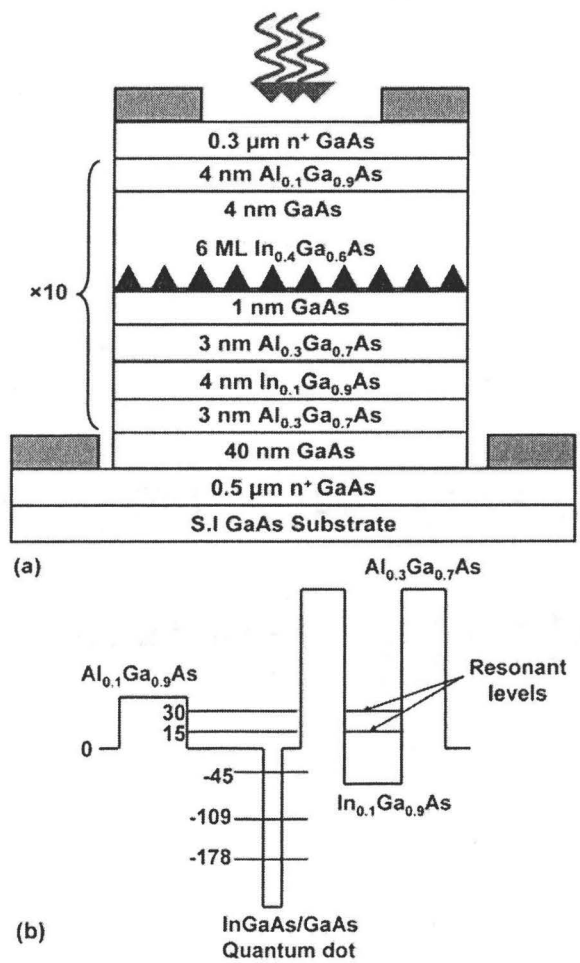

Figure 3-12 – (a) Schematic of the RT QDIP heterostructure. (b) Schematic of the conduction band profile demonstrating the energy levels (in meV), relative to CB bottom in GaAs, in the quantum dot and quantum well [47, 48].

The numerical approach used to obtain the energy spectrum of the RT QDIP is to enclose the region that contains the quantum dot by a cylinder of

radius R and height Z_C as shown in Fig. 3-13. The radius and height of the cylinder are chosen such that the cylinder encloses one quantum dot, including the double barrier, the quantum well and the single barrier ($Al_{0.1}Ga_{0.9}As$) opposite to the double barrier, as shown in Fig. 3-13. The model physically approximates the problem by considering one quantum dot, which is uncoupled to other quantum dots, and lies on an infinite wetting layer. The spectral function and the density of states, which is defined as the number of energy states inside the cylindrical volume which contains one quantum dot, can be calculated. Both the discrete energy levels inside the quantum dot and the continuum energy levels in the wetting layer, the quantum well and the double barrier structure will appear in the density of states and hence the possible energy transitions for electrons can be determined. The density of states of the structure is obtained by solving for the retarded Green's function. To describe the potential energy profile of electrons inside the cylinder, the conduction band offsets between the different materials in the heterostructure need to be calculated.

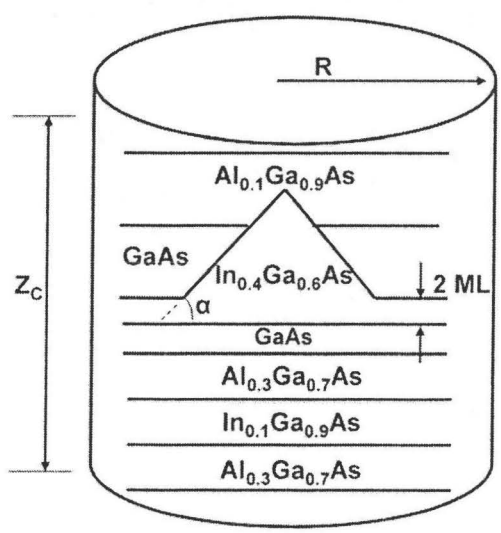

Figure 3-13 – Schematic of the RT QDIP structure used for formulating the potential energy

The conduction band offsets of AlAs and InAs compared to GaAs are taken to be 60% of the band gap differences [46, 107]. The band gap of $Al_xGa_{1-x}As$ and $In_xGa_{1-x}As$ can be calculated from the simple quadratic formula [108]

$$E_g(A_{1-x}B_x) = (1-x)E_g(A) + xE_g(B) - x(1-x)C, \tag{3.16}$$

where C is called the bowing parameter to account for the deviation from the linear interpolation and is 0.477 for $In_xGa_{1-x}As$ and $-0.127+1.310x$ for $Al_xGa_{1-x}As$. The zero level is chosen to be the conduction band edge of GaAs. The calculated band offsets for $Al_{0.3}Ga_{0.7}As$, $Al_{0.1}Ga_{0.9}As$, $In_{0.4}Ga_{0.6}As$ and $In_{0.1}Ga_{0.9}As$ are 250, 95, -333 and -92 meV, respectively. A linear interpolation is used to calculate the effective masses in the different materials. The effective masses used for GaAs, $Al_{0.3}Ga_{0.7}As$, $Al_{0.1}Ga_{0.9}As$, $In_{0.4}Ga_{0.6}As$ and $In_{0.1}Ga_{0.9}As$ are 0.067, 0.092, 0.075, 0.048 and 0.062 respectively. The band offset used for InAs is -500 meV and its effective mass is 0.026, while the band offset for AlAs is 500 meV and its effective masses in the radial- and z- direction (growth direction) are 0.22 and 0.97, respectively [108]. From the calculated band offsets, the potential energy profile for the RT-QDIP, $V(r, z)$, can be obtained and it is shown in Fig. 3-14. It is drawn in a plane passing through the axis of the cylinder, where r varies from 0 to R and z varies from 0 to Z_C. Figure 3-14 shows the $In_{0.4}Ga_{0.6}As$ quantum dot (with a base of 25 nm and a height of 6 nm), the wetting layer (2 MLs thick), the quantum well and the double barrier structure. The variations in effective masses are described in the same way as that used for the potential energy. The retarded Green's function is calculated numerically from Eq. (3.10) by doing a matrix inversion at certain values of E and n. For the RT QDIP, the height of the cylinder is taken to be 20 nm while the radius of the cylinder is 30 nm. The grid step is 0.2 nm, and hence the matrix dimension is 15000×15000. The spectral function and the DOS are calculated the same way as described before for the QDWELL structure.

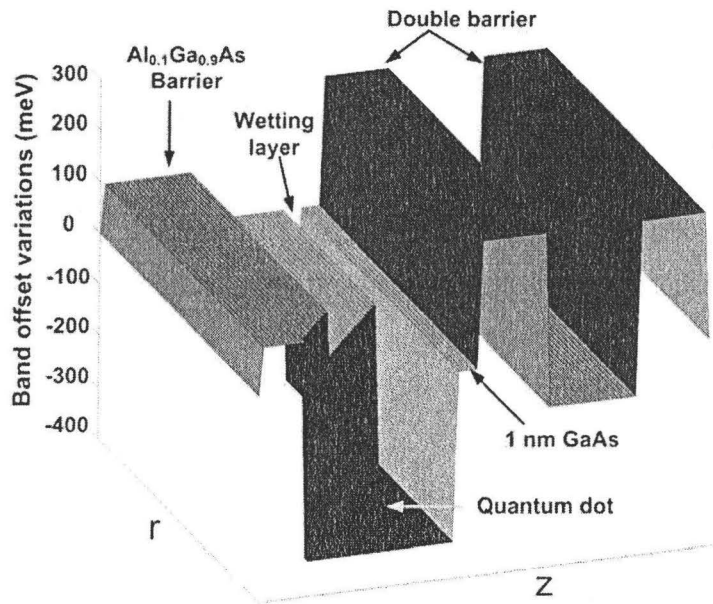

Figure 3-14 – The potential energy profile of the RT QDIP used for the theoretical modeling is plotted as a function of r and z.

The measured responsivity of the RT QDIP is shown in Fig. 3-15 [24]. The figure shows two strong peaks at $\lambda \sim 6$ μm and $\lambda \sim 17$ μm, in addition to a weak response at $\lambda \sim 9$ μm. The corresponding energy transitions ΔE due to photon absorption at these wavelengths are ~ 206, 113 and 73 meV. It is also shown that the peak centered at λ=6 μm is split into two peaks at λ=5.8 μm and λ=6.2 μm with an energy separation ΔE=14 meV.

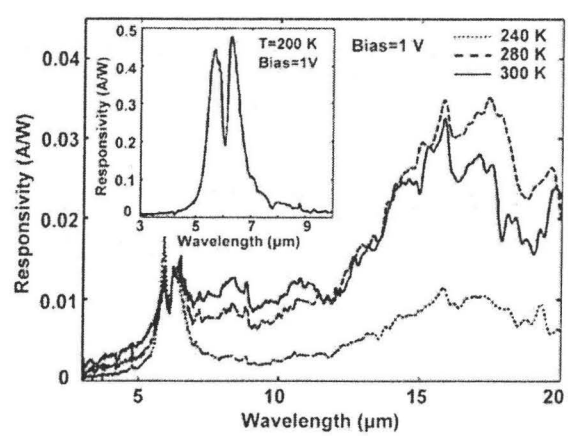

Figure 3-15 – The measured responsivity of the RT QDIP [24].

To interpret the characteristics of the responsivity curve (Fig. 3-15), we need to calculate the density of states of the RT QDIP. The matrix representation of the spectral function can be used to obtain the density of states such that $D(E) = \sum_{j=1}^{N_r} \sum_{k=1}^{N_z} ja \times A(ja, ka; E)$. The calculated density of states of the RT QDIP is shown in Fig. 3-16. The figure shows three peaks at E=-178, -109 and -45 meV corresponding to the three quantized levels inside the quantum dot in addition to continuum of states for E>0. The peaks look like delta-functions which is the case for a 3-D confining potential. When the Green's function is calculated for E<0, a small (infinitesimal) imaginary part (η) is added to the energy, $E \rightarrow E + i\eta$ in order to remove the singularities before doing the matrix inversion. Physically, the addition of this small imaginary part is attributed to the disorder in the shape and size of the quantum dots, as we consider only the average values in the calculations, which broadens the delta functions in the spectrum.

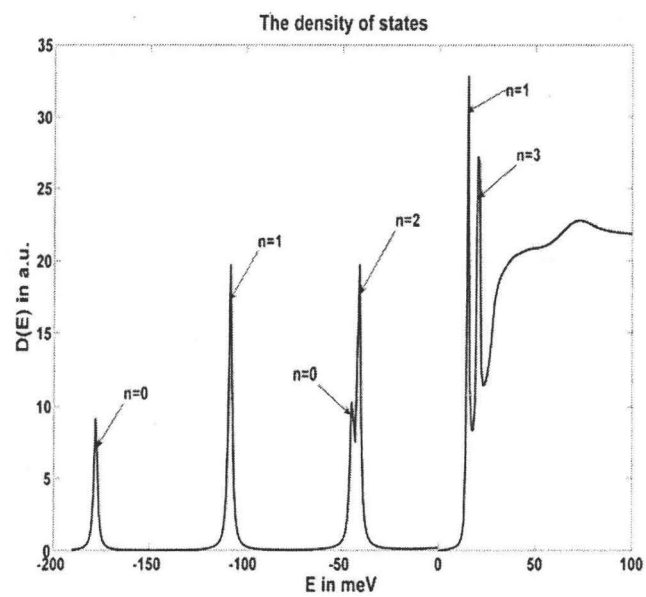

Figure 3-16 – The density of states of the RT QDIP.

The main contribution to the ground state at E=-178 meV comes from n=0, while the other terms in the series for $n \neq 0$ are very small. The first excited state at E=-109 meV is from n=1 and n=-1 as they are degenerate. The second excited state has contribution from n=0 at E=-45 meV and from n=2 at E=-40 meV. The spectral functions corresponding to the three eigenstates of the quantum dot are shown in Fig. 3-17. It is shown that the states are mainly concentrated in the region of the quantum dot since the spectral function is almost zero outside the QD.

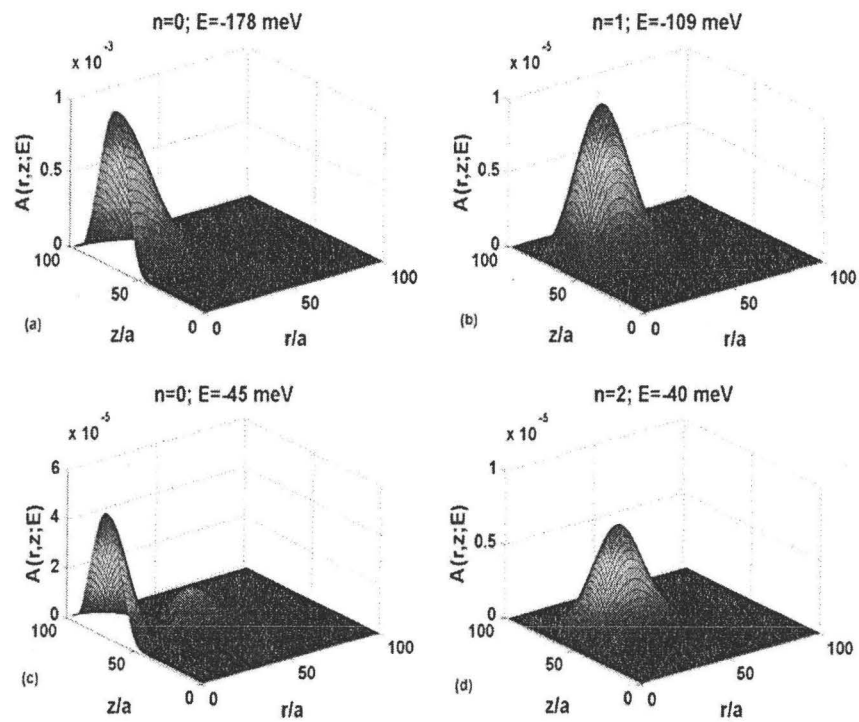

Figure 3-17 – The spectral function of the RT QDIP in the quantum dot at (a) the ground state at n=0 and E=-178 meV; (b) the first excited state at n=1 and E=-109 meV; (c) the second excited state at n=0 and E=-45 meV; and (d) the second excited state at n=2 and E=-40 meV.

In the continuum part of the spectrum, there are two peaks at E=15 and 20 meV superimposed on two step functions whose edges are at E=15 and 30 meV. To illustrate this part of the spectrum in detail, the contribution of the density of states from n=1 and n=3 are shown in Fig. 3-18. It is also shown in the figure the

density of states for the structure in the absence of the quantum dot, but the wetting layer is included. The two peaks at E=15 and 20 meV in the density of states in Fig. 3-18 are from n=1 and n=3. The spectral function, in the presence and absence of the quantum dot, is also shown in Fig. 3-19 at a point in the continuum spectrum where E=32 meV. The figure shows the variation of the number of states inside the cylinder between the first barrier of the double barrier, z=3 nm, and the barrier of the quantum well, $z=Z_C$-4 nm. The effect of the quantum dot appears in the deformation of the spectral function and in the existence of the two peaks that correspond to n=1 and 3.

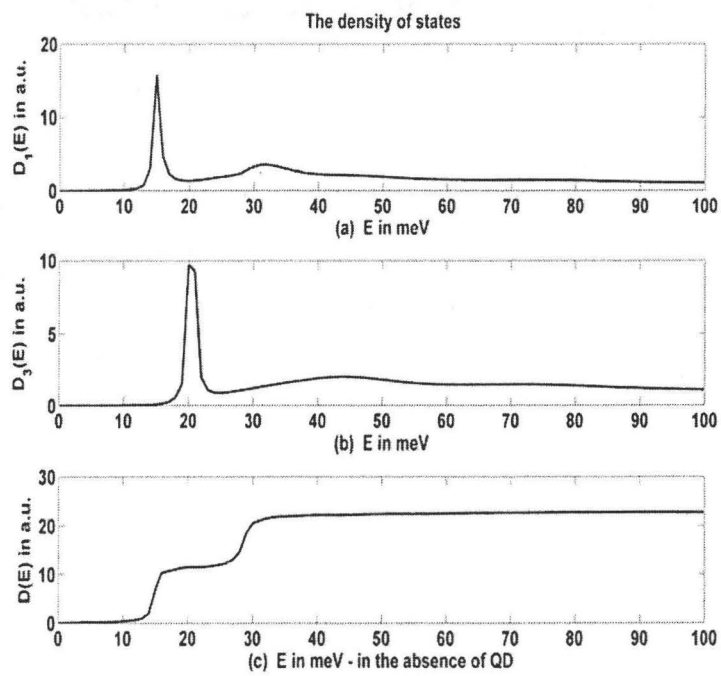

Figure 3-18 – (a) The density of states at n=1; (b) the density of state at n=3; and (c) the density of state in the absence of the quantum dot.

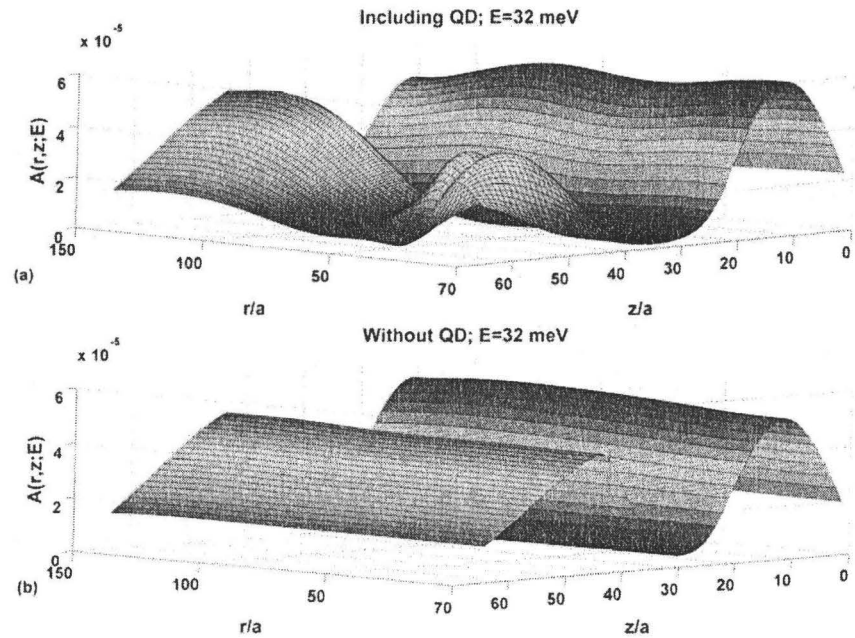

Figure 3-19 – The spectral function of the tunneling QDIP at E=32 meV (a) with and (b) without including the quantum dot potential.

The two step functions in the spectrum (Fig. 3-18(c)) are due to two levels at E=15 and 30 meV in the quantum well above the quantum dot. These two levels are formed as a result of the interaction between the wavefunctions in the double barrier and the quantum well. Due to this interaction, the energy level splits into these two levels, corresponding to two distinct eigenstates which are symmetric and anti-symmetric in the z-direction, allowing for resonant tunneling through the structure, as shown in Fig 3-20.

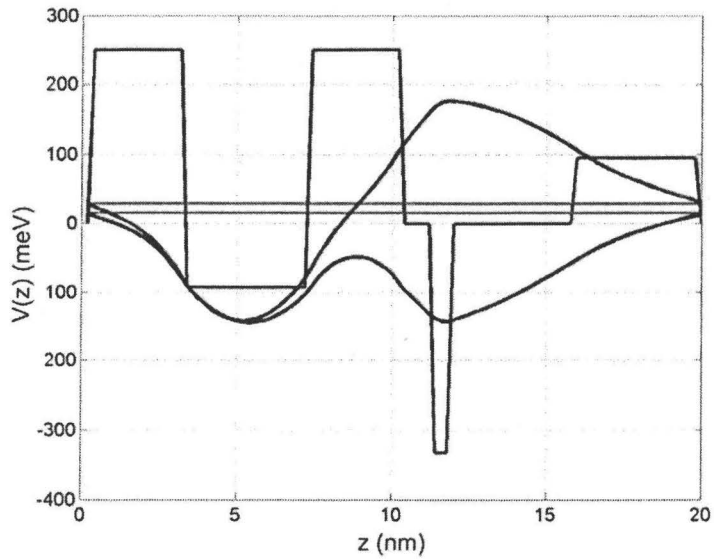

Figure 3-20 – The resonant levels and the corresponding z-component wavefunctions of the RT QDIP.

The calculated DOS shown above was done at zero applied bias. For non-zero bias, we have to modify the potential energy profile in Fig. 3-14 to include the electric field effect throughout the structure. An additional potential energy term will be added to the Hamiltonian of the system in the form $V(z) = -eFz$, where F is the electric field strength which is assumed to be uniform. The self-energy Σ^r is modified through the new eigenvalues and eigenstates, ε_m and χ_m, obtained by solving Eq. (3.13) and taking into consideration the modified potential. Figure 3-21 shows the variation of the eigenvalues inside the quantum dot and of the resonant levels in the quantum well with the electric field. The eigenvalues shift to lower values with the increase of the electric field. The separation between the eigenvalues are nearly constant, which means that the peaks in the responsivity curve will be nearly the same as in the zero bias condition for these electric field values.

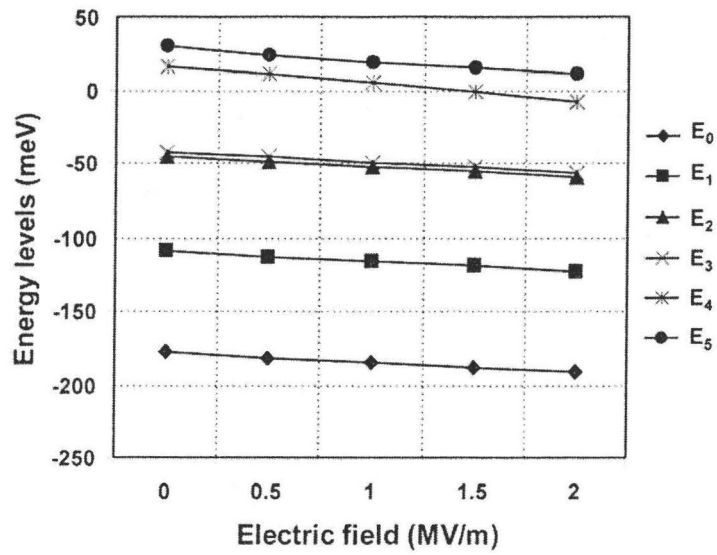

Figure 3-21 – Variation of the theoretically calculated energy levels in the quantum dot and resonant levels in the quantum well of the RT QDIP with the applied electric field.

3.4. SUPERLATTICE (SL) QDIP

The SL-QDIP is a modified version of the dot-in-a well (DWELL) structure. The InAs QDs are embedded in a GaAs/AlAs superlattice barrier. It benefits from the increased carrier confinement due to the AlAs barrier and the spectral response tunability due to the multiple transitions between the QD energy states and the minibands in the SL quantum well. The growth of the InAs QDs directly on the AlAs barrier increases the QD density by one to two orders of magnitude relative to that of conventional InAs/GaAs QDs, and this is due to the low mobility of In on AlAs compared to GaAs which affects the adatom kinetics [51]. The responsivity of this detector is high due to the high density of the QDs in the layers. A peak responsivity of 2.5 A/W measured at T= 78 K for a bias of -1.5 V was reported in [46]. The high responsivity allows the detector to be sensitive to low level optical signal. The dark current is also high due to the small thickness of the active layer and hence it has to be operated at low temperature. The schematic diagram of the heterostructure in this detector is shown in Fig. 3-22. It consists of a ten-period of 1 nm AlAs, 2 ML of InAs and 14 nm GaAs. The quantum dot

shape and size are taken to be similar to that of InAs quantum dots grown on GaAs. It is estimated that the quantum dot has a pyramidal shape with a base dimension of ~ 18 to 20 nm and a height ~3 nm [105].

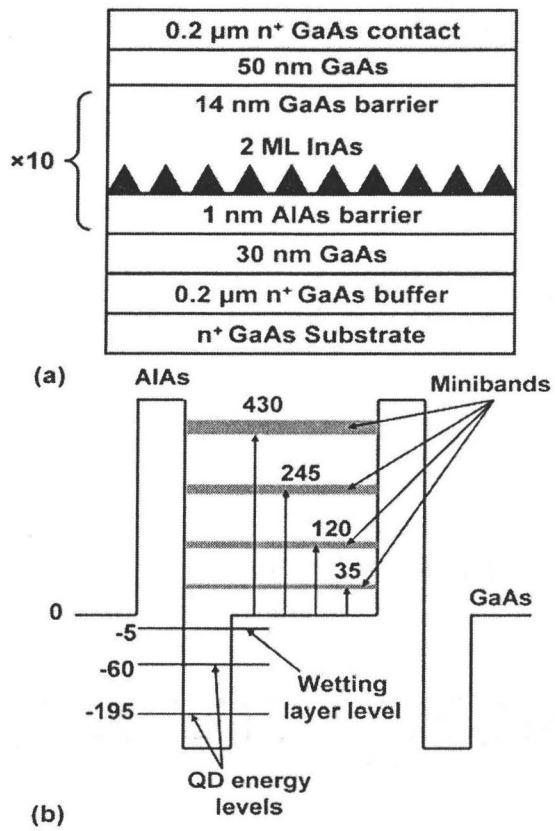

Figure 3-22 – (a) Schematic of the SL QDIP heterostructure. (b) Schematic of the conduction band profile demonstrating the energy levels (in meV) in the quantum dot and the wetting layer as well as the formation of the minibands in the quantum well.

From the calculated conduction band offsets between the different materials, the potential energy profile for the SL-QDIP, $V(r, z)$, can be obtained and it is shown in Fig. 3-23. The variations in effective masses are described in the same way as that used for the potential energy. The retarded Green's function, the spectral function and the DOS are calculated numerically in the same way as described before for the DWELL structure.

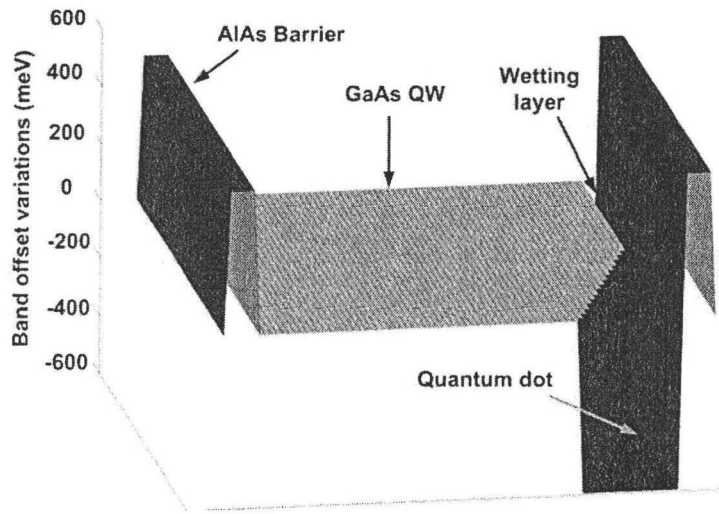

Figure 3-23 – The potential energy profile of the SL QDIP used for the theoretical modeling is plotted as a function of r and z.

The measured responsivity of SL is shown in Fig. 3-24 [24]. The maximum peak of the responsivity is observed at λ=4.3 μm corresponding to ΔE=288 meV.

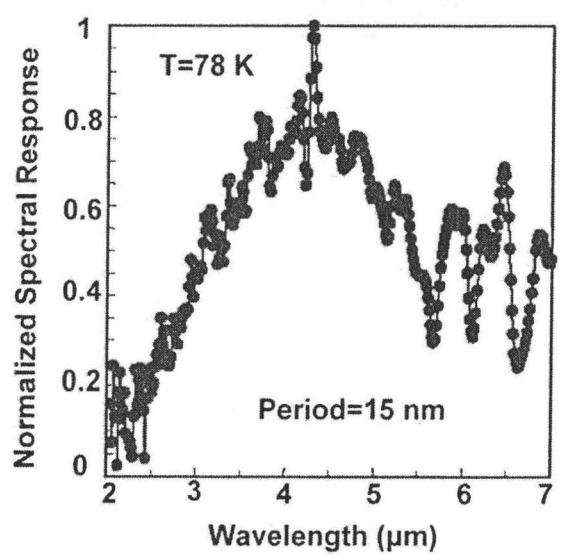

Figure 3-24 – The normalized spectral response of the SL QDIP [24].

The density of states of the SL is shown in Fig. 3-25. There are two energy levels inside the quantum dot at E=-195 and -60 meV corresponding to n=0 and 1, respectively. The step function appearing at E=-5 meV is due an energy level in the wetting layer. The step functions starting at E=35, 120, 245 and 430 meV are the minibands formed between the double barrier structure. There are two sharp peaks due to the QD potential, corresponding to n=0, that appear in the spectrum at E=40 and 110 meV superimposed on the step functions. The energy levels in the quantum dot and wetting layer and the minibands in the quantum well were shown schematically in Fig. 3-22.

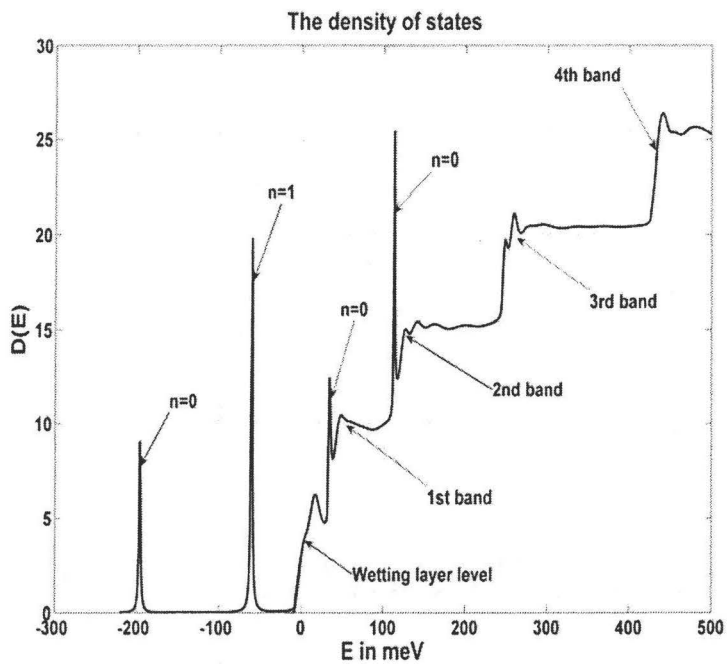

Figure 3-25 – The density of states of the SL QDIP.

The spectral functions for both the ground state and the first excited state in the quantum dot are shown in Fig. 3-26. The states are concentrated in the region of the quantum dot and nearly zero outside as expected. The maximum peak in the responsivity curve at λ=4.15 μm occurs due to the transition from the ground state to the second mini-band in the continuum states. The peaks in the responsivity at λ=6.2 and 5.75 μm are assigned to the transition from the ground

state to the wetting layer level, the peaks at λ=5.1 and 4.6 μm are assigned to the transition to the first mini-band and the peaks at λ=4.15 and 3.7 μm are assigned to the transition from the ground state to the second mini-band. Assigning the peaks of the responsivity to these transitions mentioned above will be clear after including interaction with light and calculating the dipole moments and the responsivity in the next chapter.

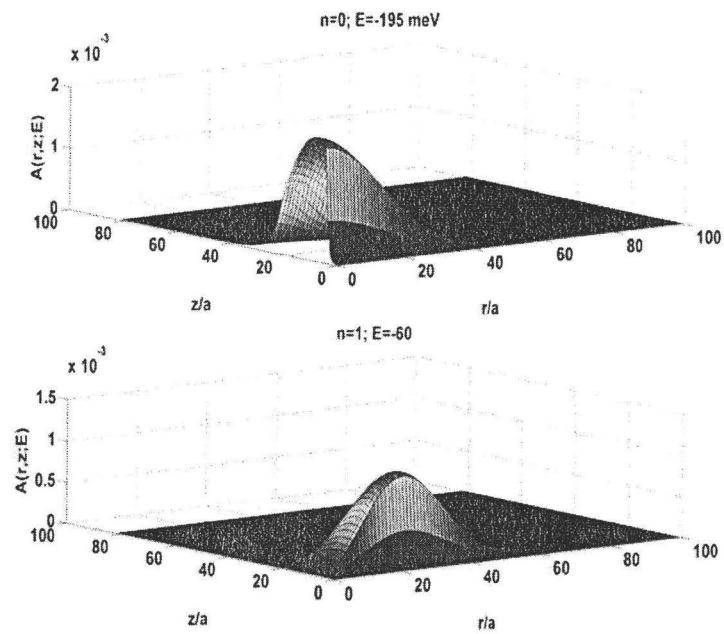

Figure 3-26 – The spectral function of the SL QDIP in the quantum dot at (a) the ground state at n=0 and E=-195 meV; and (b) the first excited state at n=1 and E=-60 meV.

CHAPTER 4 QDIPS RESPONSIVTY MODELING

The DOS of the QDs gives an insight into the possible intersubband transitions whether between the bound states of the QDs, bound-to-bound, or between the bound states and the continuum, bound-to-continuum and hence the corresponding operating wavelengths. However, the DOS does not explain why some peaks in the responsivity are bigger than other peaks and why some other peaks are very small or disappear. In order to get a better description of the responsivity, the interaction with light is required. In this chapter, a theoretical model [75] to calculate the responsivity is given. The model has been applied to the RT-QDIP and the SL-QDIP described before in the previous chapter. The model gives a good qualitative agreement with the responsivity experimentally measured for these detectors. A quantitative description of the dark and photo current using NEGF [74] will be given in the next two chapters. In the calculations of the responsivity, the first-order dipole approximation and Fermi-golden rule are used to get the selection rules for the possible transitions and the relative strength for all transitions. To calculate the dipole moment, the wavefunctions for the bound states in the QDs and for the continuum have been calculated. The bound states are calculated by solving the eigenvalue problem using the method of finite differences assuming zero boundary conditions on the cylindrical surface surrounding the QD, while the continuum states localized in the QD region are calculated using the Green's functions in a similar way that described in chapter 2. The theoretical model is then used for studying the effect of changing the quantum dot height- to-diameter ratio on the normal incidence responsivity of the SL structure for responsivity optimization.

4.1. THEORETICAL MODELING

The interaction with the electromagnetic radiation is treated within the first order dipole approximation and Fermi's golden rule. In terms of the dipole moment, the absorption coefficient is written as [109, 110]

$$\alpha(\hbar\omega)=\frac{\pi\omega}{n_r c\varepsilon_o}\frac{2}{V}\sum_{b,c}\left|\hat{e}.\mu_{bc}\right|^2\frac{\Gamma/2}{(E_c-E_b-\hbar\omega)^2+(\Gamma/2)^2}(f_b-f_c), \tag{4.1}$$

where $\hbar\omega$ is the photon energy, E_b and E_c are the energies of the initial and final states, $\hat{e}$ is the polarization direction of the incident light, $\mu_{bc}=e\langle\psi_c|\mathbf{r}|\psi_b\rangle$ is the electric dipole moment and Γ is the linewidth of the transition representing the inhomogeneous broadening due to the size inhomogeneity of the quantum dots.

The absorption coefficient defined in Eq. (4.1) gives the ratio between the number of photons absorbed per unit volume per second and the number of photons injected per unit area per second, so that the responsivity which is the photocurrent per Watt of incident radiation, can be written as [109]

$$R(\omega)=(S/\hbar\omega)\frac{\pi\omega}{n_r c\varepsilon_o}\frac{2}{V}\sum_{b,c}\left|\hat{e}.\mu_{bc}\right|^2\frac{\Gamma/2}{(E_c-E_b-\hbar\omega)^2+(\Gamma/2)^2}T(E_c)(f_b-f_c), \tag{4.2}$$

where $S/\hbar\omega$ is the optical intensity divided by the photon energy which gives the number of injected photons per unit area and $T(E_c)$ is the transmission probability of the photoexcited electrons at the total energy E_c.

4.1.1. WAVEFUNCTIONS CALCULATIONS

To calculate the dipole moment in (4.2), the wavefunctions corresponding to the initial and final states of the transitions should be obtained. The wavefunctions corresponding to the discrete energy states in the QDs are localized inside the QDs. Therefore, assuming zero boundary conditions on a virtual cylinder surrounding the QD, the bound wavefunctions and the corresponding

discrete energy eigenvalues can be calculated. In the continuum states above the QD barrier, the assumption of zero boundary conditions is not suitable for obtaining the wavefunctions in this part of the DOS. Instead, the method of the Green's function is used to calculate the wavefunctions in this part of the spectrum. A self-energy term is added to the Hamiltonian at the cylinder surface to simulate the proper boundary conditions representing the coupling with the surroundings outside the cylinder.

The wavefunctions in the bound and continuum states, due to the cylindrical symmetry of the Hamiltonian, can be written as

$$\Psi_n(r,\theta,z) = e^{in\theta}\varphi_n(r,z), \tag{4.3}$$

where n is integer and represents the quantum number of the z component of the total angular momentum. The bound state wavefunctions in the quantum dots are calculated by solving the eigenvalue problem

$$\left[EI - H_{nD}\right]\varphi_n = 0, \tag{4.4}$$

which gives all the eigenstates and the corresponding eigenvalues at the quantum number n and H_{nD} is the Hamiltonian matrix of the isolated cylinder that contains the QD at specific quantum number n. This procedure is suitable to calculate the bound states since they are localized inside the quantum dot and hence we can assume zero boundary condition at the cylinder radius.

To get the wavefunctions in the continuum part of the spectrum, the Green's function method has been used to simulate the free motion of electrons above the quantum dot and to add an additional self-energy term at the cylindrical surface to simulate the open boundary condition. The retarded Green's function gives the response at any point due to a unit excitation at any other point. So from Eq. (4.4), the Hamiltonian of the isolated cylinder is modified by adding a self-energy term to simulate the interaction with the surroundings in addition to the excitation term in the R.H.S. The wavefunctions [79] satisfy the equation

$$\left[EI - H_{nD} - \Sigma^r\right]\varphi_n = S\,, \tag{4.5}$$

where S is the excitation term due to propagating waves incident from the lead at the cylinder's surface. The retarded Green's function of the system in the cylindrical representation and in the matrix form is given by

$$\left[EI - H_{nD} - \Sigma^r\right]G^r_{nD} = [r_D]^{-1}. \tag{4.6}$$

From (4.5) and (4.6), the wavefunction can be related to the Green's function by the relation

$$\varphi_n = \left[EI - H_{nD} - \Sigma^r\right]^{-1} S = G^r_{nD}[r_D]S\,. \tag{4.7}$$

If we write the self-energy Σ^r in the compact form $\Sigma^r = \sum_m f_n(R)\left|\chi_m(z)\right\rangle\left\langle\chi_m(z')\right|$, then the excitation S is given by

$$S = \sum_m \left(f_n^*(R) - f_n(R)\right)\left|\chi_m(z)\right\rangle, \tag{4.8}$$

which gives the contribution from all propagating modes at same total energy E. The equations (4.5), (4.6), (4.7) and (4.8) are the multimode version of the 1-D single mode problem discussed before in chapter 2. The detailed form Σ^r was shown before in Eqs. (3.12) and (3.15) in chapter 3.

In normal incidence operation, the electric field is polarized in the in-plane directions, that is, x- or y-directions. Therefore for the x-polarized electric field, the dipole moment will be given by

$$\begin{aligned}\mu_{bc} = e\left\langle\psi_c\left|\mathrm{r}\right|\psi_b\right\rangle &= e\left\langle e^{il\theta}\varphi_l(r,z)\left|x\right|e^{in\theta}\varphi_n(r,z)\right\rangle \\ &= e\left\langle e^{i(n\pm1)\theta}\varphi_{n\pm1}(r,z)\left|r\cos\theta\right|e^{in\theta}\varphi_n(r,z)\right\rangle\end{aligned}$$

which indicates the selection rules for allowed optical transitions. The electrons can be photoexcited from the bound states of quantum number n to the continuum

states which differ in this quantum number by ± 1, otherwise the integration over θ will make the dipole moment vanish.

The transmission probability function $T(E_z)$ as a function of the z-component of energy E_z and neglecting the quantum dot potential, is calculated using the relation for 1-D case given by

$$T(E_z) = \mathrm{Tr}\left[\Gamma_z G_z^r \Gamma_z G_z^a\right], \tag{4.9}$$

where $G_z^r = \left[E_z I - H_z - \Sigma_z^r\right]^{-1}$, Σ_z^r is the self-energy due to coupling with the leads and for Hamiltonian matrix of dimensions $N \times N$ $\Sigma_z^r(1,1) = \Sigma_z^r(N,N) = -t.e^{ika}$ and zero otherwise. The transition rate matrix $\Gamma_z = i(\Sigma_z^r - \Sigma_z^a)$ which is zero everywhere except at the interface points with the leads $\Gamma_z(1,1) = \Gamma_z(N,N) = 2t\sin(ka)$ and $E_z = 2t(1-\cos(ka))$. Calculating the transmission function as a function of the z-component of energy E_z, assuming that the effect of the quantum dot potential can be neglected for the energy values higher than the QD barrier potential, simplifies the solution. At applied bias, the photoexcited electrons will drift in the electric field in the z-direction toward the contact. For the RT-QDIP and the SL-QDIP structures, $T(E_z)$ has non-zero values only at E_z corresponding to the resonant levels in the RT-QDIP and to the miniband energies in the QW in the SL-QDIP as shown in Figures (4-4) and (4-7). The transmission function in the z-direction as a function of the total energy will be equal to $T(E_z)$ at the resonant levels for $E \geq (E_z = \varepsilon_m)$, where ε_m are resonant levels in the quantum well, and zero for $E < \varepsilon_m$.

4.2. RT-QDIP RESPONSIVITY MODELING

The wavefunctions of the bound and continuum states are calculated using Eqs. (4.4) and (4.7) respectively. The excitation in the R.H.S of Eq. (4.7) is calculated using the two modes of the resonant levels shown in Fig. 4-1. The responsivity of the device is calculated using Eq. (4.2) and the transmission probability as a function of total energy is $T(E)\sim 1$ when E exceeds the first resonant level value and zero otherwise, since E_z coincides with one of the two resonant levels. The inhomogeneous broadening factor Γ is assumed to be 5 meV.

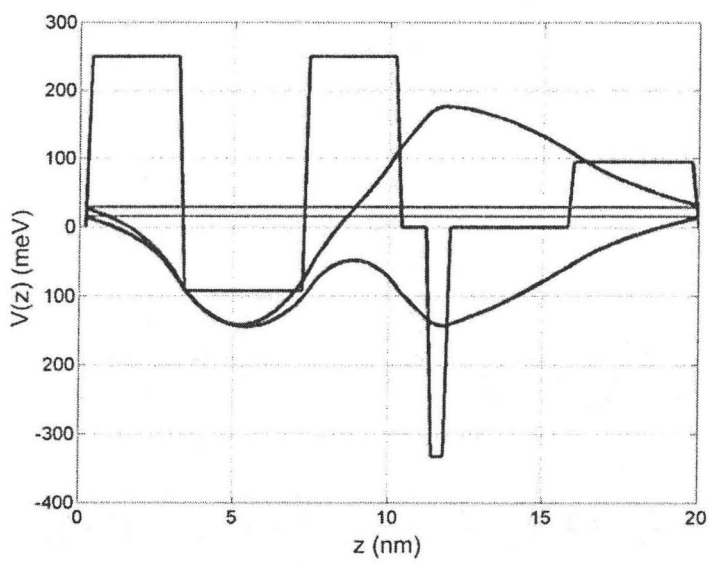

Figure 4-1 – The resonant levels and the corresponding z-component wavefunctions of the RT-QDIP

Figure (4-2) shows the calculated responsivity as a function of wavelength at different temperatures for the RT QDIP. The splitting of the peak at 6 μm is due to the transition probability from the ground state to the resonant levels in the quantum well. This is shown in Fig. 4-3 through the dipole moment between the ground state at $n=0$ and the continuum states with $n=\pm 1$. The peak at 9 μm is due to the transition from the first excited state in the quantum dot at $n=1$ to the continuum states at $n=0$ and $n=\pm 2$. The peak centered at 17 μm is due to the

transition from the second excited states in the quantum dot at n=0 to the continuum states at $n=\pm1$, and the bound state at $n=2$ to the continuum states at $n=\pm1$ and $n=\pm3$. As the temperature increases, the peak at $\lambda=17$ μm becomes more pronounced, as shown in Fig. 4-2. This can be interpreted by the occupation of the higher states in the quantum dot increasing with the temperature increase. The second excited state is more degenerate than the ground state since it has contribution from $n=0, \pm2$ in addition to the spin degeneracy, while the ground state has only spin degeneracy.

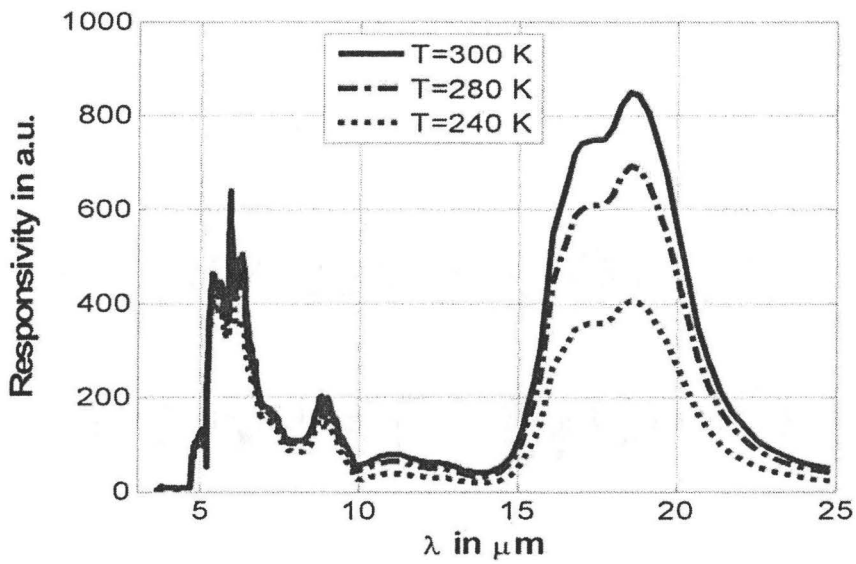

Figure 4-2 – Responsivity of the RT QDIP in a.u. at different temperatures

The calculated responsivity by this model is in good qualitative agreement with the experimental results, shown before in Fig. 3-15 in chapter 3, as it predicts the peak splitting at 6 μm due to the transition from the ground state, the weak response at 9 μm due to the transition from the first excited state in addition to the increase in the magnitude of the peak at 17 μm with temperature due to the increased filling of the second excited state. The increase of the peak at 17 μm, predicted by the model when the temperature increases from 280 K to 300 K, is due to the increase of the filling of the second level in the quantum dot which does not appear clearly in the experimental results. This can be interpreted as the

increase in temperature leading to reducing the relaxation time of the electron due to the interaction with the lattice, which leads to increasing the probability of capturing the electron in the quantum dots and hence reducing the photocurrent. This effect was not considered in the model.

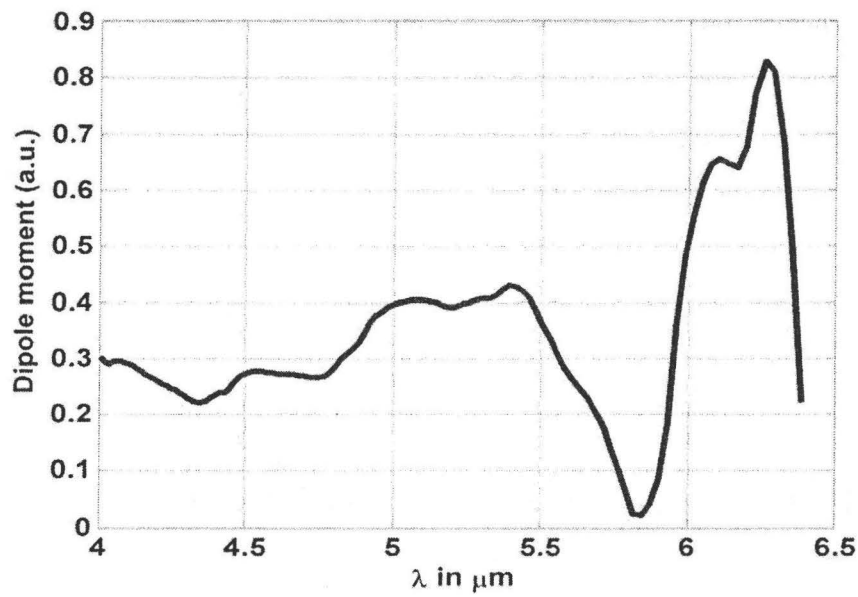

Figure 4-3 – The dipole moment of transition between the ground state of $n=0$ and the continuum states of $n=\pm 1$.

Fig. 4-4 shows the transmission function for the structure. The transmission has two peaks at the values of E_z that corresponds to the two resonant levels. The separation between the two peaks is ~ 14 meV and is the same as the separation between the resonant levels and comparable to the separation between the peaks appearing in the responsivity.

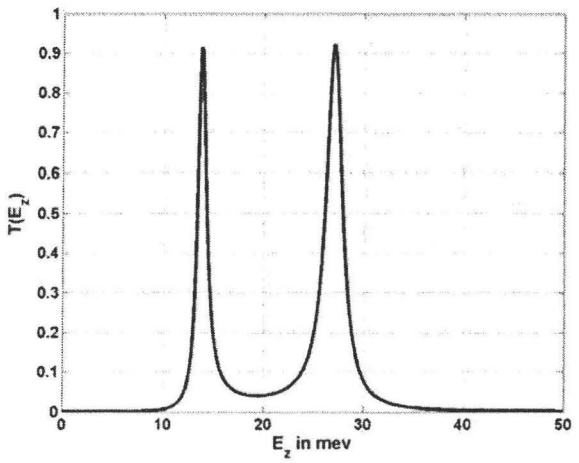

Figure 4-4 – The transmission probability function of the RT structure without including the quantum dot potential.

4.3. SL-QDIP RESPONSIVITY MODELING

The transmission probability function across the double barrier above the quantum dot of the SL structure as a function of the z-component of energy is shown in Fig. 4-5. A biasing electric field of 1 MV/m is used in the calculations. When the total energy exceeds the first band energy (E>35 meV), $T(E)$~1, while $T(E)$~0.2 when E exceeds the wetting layer level and is less than the first mini-band energy.

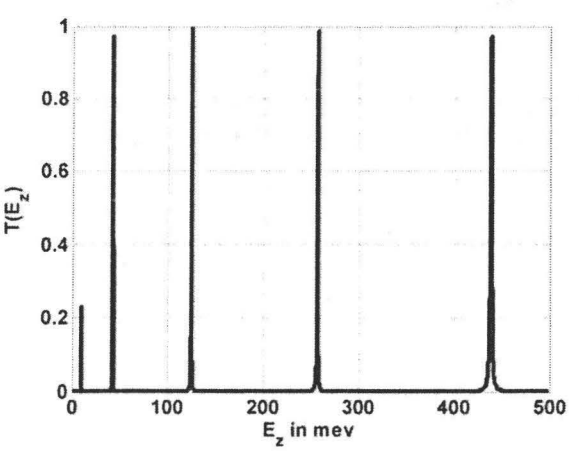

Figure 4-5 – The transmission probability function of the SL structure without including the quantum dot potential.

The normalized responsivity is calculated and shown in Fig. 4-6. The dipole moments of transitions from the ground and first excited states in the quantum dot to the continuum states are shown in Fig. 4-7. It is noticed from Fig. 4-7 that the peak maximum in the responsivity curve at λ=4.15 μm occurs due to the transition from the ground state to the second mini-band in the continuum states. The peaks in the responsivity, in Fig. 4-6, at λ=6.2 and 5.75 μm are assigned to the transition from the ground state to the wetting layer level, the peaks at λ=5.1 and 4.6 μm are assigned to the transition to the first mini-band and the peaks at λ=4.15 and 3.7 μm are assigned to the transition from the ground state to the second mini-band.

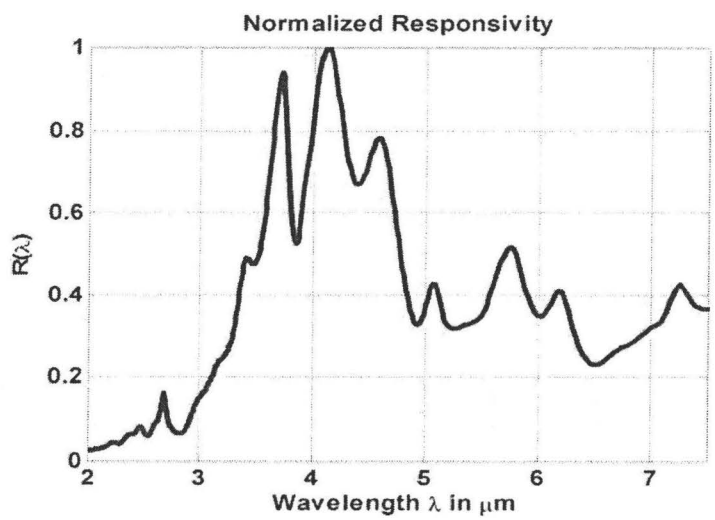

Figure 4-6 – Normalized responsivity of the SL-QDIP.

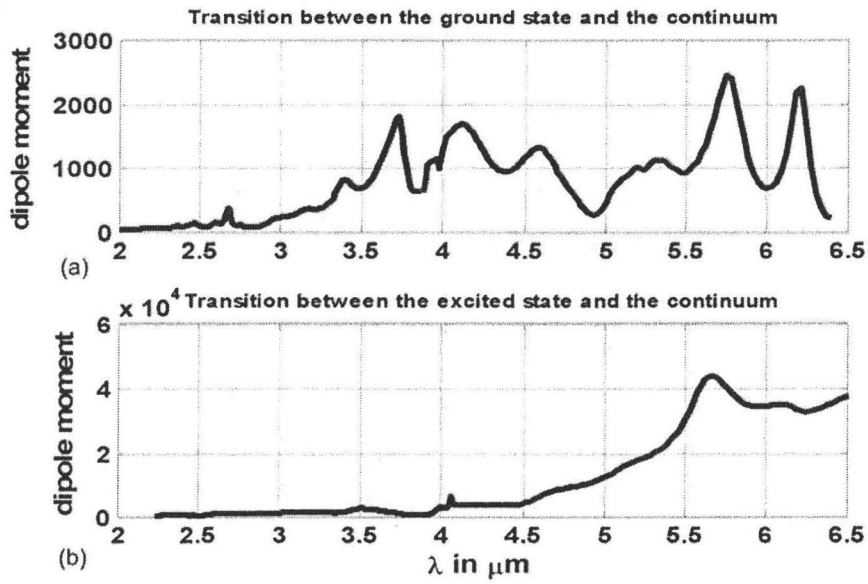

Figure 4-7 – The dipole moment of transition between (a) the ground state of n=0 and the continuum; (b) the first excited state at n=1 and the continuum.

4.4. SL-QDIP RESPONSIVITY OPTIMIZATION

To study the effect of changing the shape of the quantum dot on the normal incidence responsivity, the responsivity is calculated for different height-to-diameter ratios as shown in Fig. 4-8 such that the ground state energy level is kept almost constant and the Fermi level is taken to be 90 meV above the ground state energy level in all shapes to keep the occupation of QDs the same equivalent to same doping density. Figure 4-9 shows the calculated responsivity versus wavelength for various quantum dot shapes while the other parameters in the structure are kept the same, such as the QD density and the heterostructure design. Increasing the height-to-diameter ratio leads to increasing the responsivity. So taller quantum dots is more sensitive to normal incidence light than shorter ones. This is expected since when h/D→0, the quantum dot layer transforms to a quantum well which is insensitive to normal incidence light. Figure 4-10 shows the amount of increase in the peak responsivity as a function of the height-to-diameter ratio.

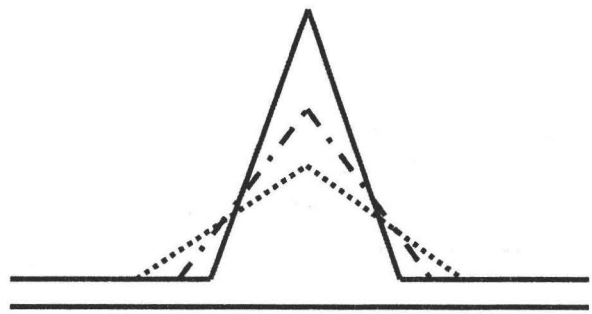

Figure 4-8 – Different height-to-diameter ratio QDs

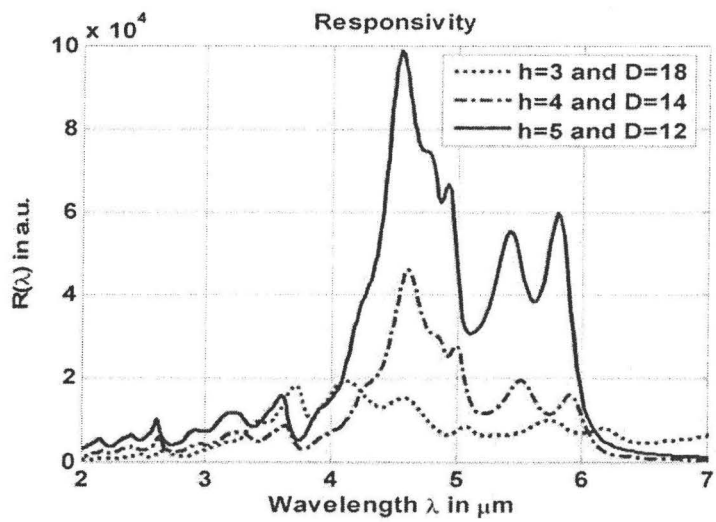

Figure 4-9 – The responsivity in a.u. for the SL QDIP for different quantum dot shapes.

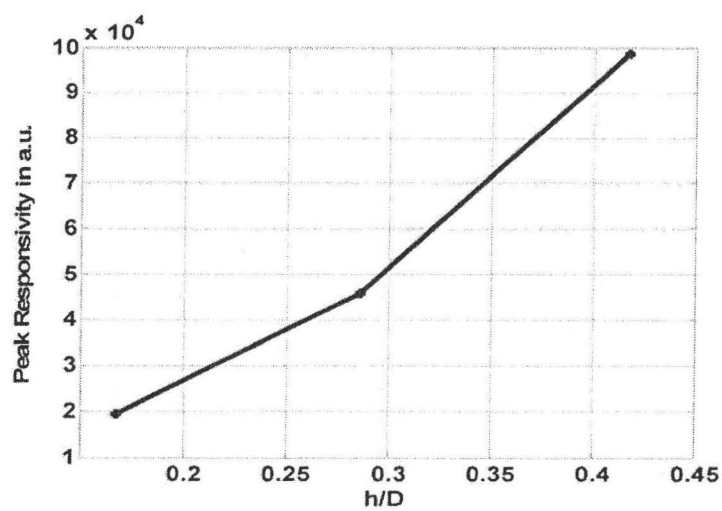

Figure 4-10 – The peak responsivity as a function of the height-to-diameter ratio

To investigate the increase of the height of the quantum dot with a fixed diameter as shown in Fig. 4-11 and with the same doping density, the normal incidence responsivity is calculated for three quantum dots with the same diameter but having different heights. The doping density is kept constant and hence the Fermi level is taken to be above the ground state by 90 meV in all cases. Figure 4-12 shows the calculated responsivity for the three quantum dot structures. From the figure, the responsivity decreases with height increase which means the quantum dots with smaller size give higher responsivity than the ones with larger sizes. So the optimum solution for normal incidence peak responsivity is to maximize the height-to-diameter ratio of the quantum dot, such that the ground state position is kept constant.

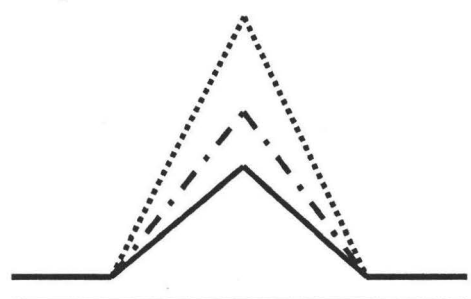

Figure 4-11 – Fixed diameter with different height QDs

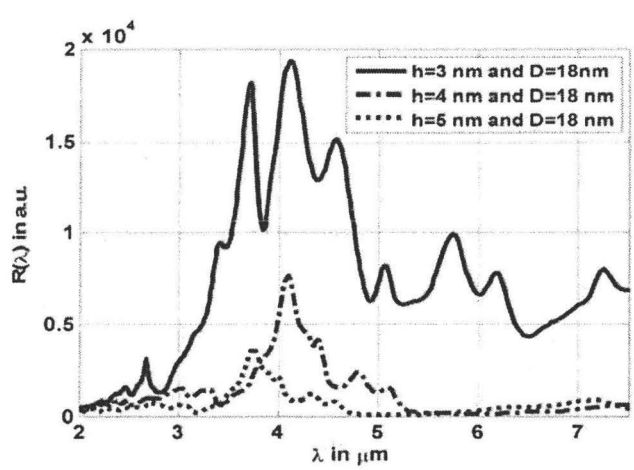

Figure 4-12 – The responsivity in a.u. for the SL QDIP for different quantum dot heights at fixed diameter size

CHAPTER 5 DARK CURRENT MODELING

Theoretical modeling of the dark and photocurrent in QDIPs is very useful since it allows studying the dark and photocurrent characteristics at different design parameters such as doping density, barrier separation between QD layers and the number of QD layers to establish the optimized detector design. Reducing the dark current of the QDIP will improve the detector detectivity or the signal to noise ratio (SNR) and the photoresponse of the detector can be still detectable at higher operating temperature. In this chapter, a theoretical model [74] describing electron dynamics in QDIPs is presented to obtain the dark current characteristics of the RT-QDIP. The model is based on the non-equilibrium Green's functions formalism (NEGF) which provides a general framework to study electron transport in a non-equilibrium quantum system and in the presence of interactions [111, 112, and 115]. A self-consistent solution of the charge density and the average potential energy through the device by satisfying Poisson's equation has been obtained; hence, the Hamiltonian of the QDs is established. The self-energies due to coupling with the contact layers and due to internal electron interactions are calculated and then the Green's functions of the QDs are obtained by numerically solving their governing kinetic equations using the method of finite differences. A quantum transport equation using the Green's functions is formed to calculate the current. The model [74] has been applied to simulate the dark current and to extract microscopic information about the density of states and carrier distribution in the quantum dot bound and continuum states. The simulated dark currents with this model are in good agreement with experimental results over a wide range of applied biases and temperatures. The model was also used to

study the effect on the dark current and the average number of electrons occupying the QDs due to changing the QD doping density, the barrier separation between QD layers and the number of QD layers. The model is general and can be applied to any QDIP structures as a tool in design and for predictions of their dark current characteristics.

5.1. QUANTUM TRANSPORT MODEL

Theoretical models to study the current of QDIP performance under dark or light conditions have been made [16, 25, 64-69]. In these models, the current is obtained from a balance equation between the carrier capture rate and the thermal and photoexcitation rates. The calculations of these rates contain fitting parameters obtained by comparisons with the experimental results. Microscopic models such as those reported in [70, 71], provide a better description of the QDIP relevant parameters by taking into consideration the QD shape and size to calculate the QD wavefunctions, which in turn can be used to calculate the transition rates. The current is calculated using a semiclassical Boltzmann equation.

A quantum transport model [111-115] can be used to produce a better description of the electron dynamics in QDIPs as it takes into consideration the microscopic device structure such as, the shape, size and composition of QDs, density of QDs, and doping density as well as to the internal structure design. The advantage of such a quantum transport model is that it gives a general framework to deal with quantum structure under non-equilibrium conditions such as high applied biases and in the presence of internal interactions. The interactions inside the device can be electron-electron, electron-phonon or electron-photon interactions. According to the type of interactions included, electron scattering can be elastic, which causes no energy transitions between different energy states or inelastic which leads to energy transitions. The straightforward way of including interactions in the system gives considerable flexibility in the types of

interactions to be included and the degree of approximations to be used depending on the accuracy required in the results and the complexity of the calculations. The internal parameters such as density of states (DOS) and electron density, in addition to the transmission function and current, can be obtained.

In next sections, a theoretical model [74] based on non-equilibrium Green's functions (NEGF) is given. The model is used first to calculate the DOS of the QDs, which then is used to calculate the electron density. A self-consistent solution of electron density and the average potential energy satisfying Poisson's equation has been achieved, allowing determination of the average potential and the estimated quasi-Fermi level throughout the structure. After obtaining the potential energy, the Hamiltonian of the QD is obtained and then the Green's functions are calculated. Using the quantum transport equation of the Green's functions, the dark current of the device is calculated. The model is applied to the RT-QDIP device discussed before in the previous chapters to calculate the dependence of the dark current on bias at various temperatures and compare with the experimental data. This device structure shows better performance in terms of dark current and operating temperature compared to other conventional QDIPs since the measured dark current values are two orders of magnitude less than for conventional QDIP structures [47]. A Green's function model to calculate the responsivity of RT-QDIP has been shown in chapter 4. In this model, the retarded Green's function contains all the information we need to calculate the DOS and the electron density since equilibrium conditions are assumed at low applied biases. The retarded Green's function is used to calculate the DOS in addition to the wavefunctions in the continuum part of the spectrum. However, at non-equilibrium conditions at high applied biases and in the presence of interactions, the NEGF formalism should be used which combines quantum dynamics with dissipative interactions. In NEGF formalism, the retarded Green's function describes the dynamics of the electrons inside the device, while the correlation Green's function is needed to calculate the current and the electronic occupation

of different energy states at non-equilibrium. The calculated dark current determined by the given model shows a good agreement with the experimental results. The model is also used to study the effect of varying the barrier widths between the QD layers, QD doping density and number of QD layers on the dark current. The details of the model and the dark current characteristics results are presented in the following sections.

5.2. STEADY-STATE NEGF

For steady-state transport in a quantum system, The Green's functions can be obtained as a function of the total energy. The retarded Green's function describes the dynamics of the electrons and its imaginary part gives the localized density of states of the system. At equilibrium, these states are occupied according to the Fermi function. However, at non-equilibrium, the states are filled according to the correlation or the lesser Green's function. The relation between the retarded and lesser Green's functions are through the kinetic equation. The correlation functions, lesser ($G^<$) and greater ($G^>$) Green's functions are given by [79]

$$G^< = G^r \Sigma^< G^a \text{ and } G^> = G^r \Sigma^> G^a , \tag{5.1}$$

where $\Sigma^<$ and $\Sigma^>$ are the lesser (in-scattering) and greater (out-scattering) self-energy functions of electron due to coupling with the contact layers and interactions. The electron and hole densities per unit energy are given by

$$n(\mathbf{r};E) = (-i/2\pi) G^<(\mathbf{r},\mathbf{r};E) \text{ and } p(\mathbf{r};E) = (i/2\pi) G^>(\mathbf{r},\mathbf{r};E), \tag{5.2}$$

and the local density of states $A(\mathbf{r};E) = n(\mathbf{r};E) + p(\mathbf{r};E) = -2\,\mathrm{Im}\left[G^r(\mathbf{r},\mathbf{r};E)\right]$.

For a cylindrically symmetric system as in the case of conically shaped QDIPs, the potential energy in the vicinity of QDs is invariant under rotation around QD axis. By considering only local interactions in the system, the self-energy can be considered independent of rotation angle θ. Therefore, the dimensions of the problem can be reduced from 3D to 2D problem. In cylindrical

coordinate's representation, the retarded Green's function of the system including local interactions is written as [111]

$$\left[E - H_{\text{op}} - \Sigma^{r}_{\text{int}}(r,z;E)\right] G^{r}(r,r';\theta,\theta';z,z';E) = \frac{1}{r}\delta(r-r')\delta(\theta-\theta')\delta(z-z'), \quad (5.3)$$

where the Hamiltonian operator of the system in cylindrical coordinates is given by

$$H_{\text{op}} = -\frac{\hbar^2}{2}\left(\frac{1}{r}\frac{\partial}{\partial r}\frac{r}{m^{r}(r,z)}\frac{\partial}{\partial r} + \frac{1}{m^{r}(r,z)}\frac{1}{r^2}\frac{\partial^2}{\partial\theta^2} + \frac{\partial}{\partial z}\frac{1}{m^{z}(r,z)}\frac{\partial}{\partial z}\right) + V(r,z). \quad (5.4)$$

and Σ^{r}_{int} is the retarded self-energy due to localized interactions. In Eq. (5.4), $V(r,z)$ is the potential energy seen by the electron and it is given by the summation of the conduction band offsets shown in Fig. 3-14 and the average potential energy satisfying Poisson's equation at the specific applied bias, and m^{r} and m^{z} are the in-plane and out-of-plane effective masses, respectively. Since the potential energy and the self-energy are not a function of θ, then the z-component of the angular momentum and the Hamiltonian commute, and hence, the Green's function can be written as

$$G^{r}(r,r';\theta,\theta';z,z';E) = \frac{1}{2\pi}\sum_{n} e^{in(\theta-\theta')} G^{r}_{n}(r,r';z,z';E), \; n \text{ is an integer.} \quad (5.5)$$

By substituting (5.5) into (5.3) and following the same procedure used before in chapter 3 to replace the contact layers by self-energy, we end up with

$$\left[EI - H_{\text{n}} - \Sigma^{r}_{\text{n}} - \Sigma^{r}_{\text{int}}\right] G^{r}_{\text{n}} = [r]^{-1}, \quad (5.6)$$

where H_{n} is the matrix representation of the Hamiltonian obtained using the finite differences applied to H_{op} defined in Eq. (5.4) after replacing $\left(\partial^2/\partial\theta^2\right)$ by $\left(-n^2\right)$ as shown in chapter 3. The subscript n associated with the Green's functions, Hamiltonian, and self-energies means that the calculations of these

matrices are done at a specific value n which is the quantum number of the z-component of total angular momentum. The Hamiltonian matrix H_n represents the non-interacting Hamiltonian of an isolated QD inside the virtual cylinder enclosing the QD. The coupling between the QD inside the cylinder and the surrounding, contact layers at specific n is given by the self-energy Σ_n^r. The localized interactions are given by the self-energy Σ_{int}^r which is independent of n. The term $[r]$ is a diagonal matrix whose diagonal elements are the radial part of the position vector of the electron inside the cylinder.

The diagonal elements of the localized density of states are given by

$$\begin{aligned} A(r,z;E) &= -2\,\mathrm{Im}\left[G^r(r,r;\theta,\theta;z,z;E)\right] \\ &= -\frac{1}{\pi}\sum_n \mathrm{Im}\left[G_n^r(r,r;z,z;E)\right] = \sum_n A_n(r,z;E) \end{aligned} \quad (5.7)$$

The density of states is obtained from A and is given by

$$D(E) = \frac{1}{2\pi}\mathrm{Tr}\left[A(r,z;E)\right] = \frac{1}{2\pi}\int 2\pi r\; A(r,z;E)\,dr\,dz\,. \quad (5.8)$$

The electron and hole densities are given by

$$\begin{aligned} n(r,z;E) &= (-i/2\pi)\sum_n G_n^<(r,r;z,z;E) \text{ and} \\ p(r,z;E) &= (i/2\pi)\sum_n G_n^>(r,r;z,z;E) \end{aligned}\,, \quad (5.9)$$

where $G_n^< = G_n^r\left(\Sigma_n^< + \Sigma_{int}^<\right)G_n^a$ and $G_n^> = G_n^r\left(\Sigma_n^> + \Sigma_{int}^>\right)G_n^a$

5.2.1. CALCULATING THE SELF-ENERGY

The self-energy $\left(\Sigma^r\right)$ and scattering functions $\left(\Sigma^<\text{ and }\Sigma^>\right)$ used in calculating the retarded $\left(G^r\right)$and correlation Green's functions $\left(G^<\text{ and }G^>\right)$ are due to the coupling with the contact layers and internal interactions. Assuming

that they are independent, then they can be respectively written as $\Sigma^r = \Sigma^r_{\text{cl}} + \Sigma^r_{\text{int}}$, $\Sigma^< = \Sigma^<_{\text{cl}} + \Sigma^<_{\text{int}}$ and $\Sigma^> = \Sigma^>_{\text{cl}} + \Sigma^>_{\text{int}}$.

5.2.1.1. Contact layers self-energy

The Hamiltonian used in Eq. (5.6) is for an isolated QD and hence the contact layers are replaced by the self-energy which is given by [74]

$$\Sigma^r_{\text{n}} = \tau^{\dagger}\left[EI - H_{\text{nL}}\right]^{-1}\tau[r_{\text{L}}], \tag{5.10}$$

where τ is the coupling matrix whose elements are zero every where except at the interface points inside the contact layers adjacent to the points inside the QD cylinder and H_{nL} is the Hamiltonian of the isolated contact layer.

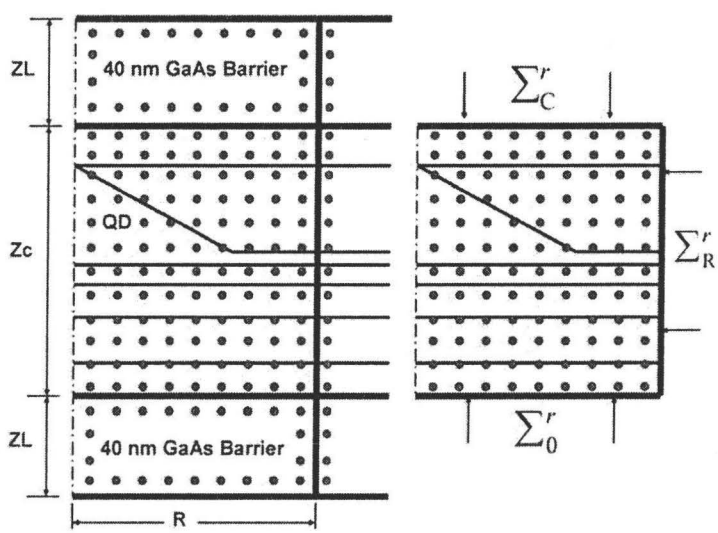

Figure 5-1 – Schematic of the lattice grid in *r-z* plane used in the numerical simulation. The surrounding contact layers are replaced by self-energies at the interface planes of the QD cylinder

Figure 5-1 shows a schematic of a discrete lattice-grid of an *r-z* plane passing through the axis of a QD containing one QD layer including the barriers that separate it from the previous and adjacent layers. The GaAs barriers above and below the cylinder in addition to the semi-infinite contact layer for $r>R$ are replaced by self-energies at the interface points at $z=ZL$, $z=ZL+Zc$ and at $r=R$.

The self-energy due to the semi-infinite contact layer is calculated analytically and shown before in chapter 3 and is given by

$$\Sigma^{r}_{\mathrm{nR}} = t^2 G^{r}_{\mathrm{nL}} R, \tag{5.11}$$

and G^{r}_{nL} are the elements of the retarded Green's function of the contact layer at $r=R+a$, $t = \hbar^2 / 2ma^2$ is the hopping parameter and a is the lattice grid constant. The self-energy for the upper barrier is calculated numerically using

$$\Sigma^{r}_{\mathrm{nC}} = \tau^{\dagger}\left[EI - H_{\mathrm{nLC}} - \Sigma^{r}_{\mathrm{nRC}} \right]^{-1} \tau[r_{\mathrm{L}}] = t^2 G^{r}_{\mathrm{nLC}}\Big|_{z,z'=a}[r_{\mathrm{L}}], \tag{5.12}$$

where H_{nLC} is the Hamiltonian of the isolated upper barrier, $\Sigma^{r}_{\mathrm{nRC}}$ is the portion of self-energy of the semi-infinite layer Σ^{r}_{nR}, from $z=ZL+Zc$ to $z=2ZL+Zc$, coupled to the upper barrier at $r=R-a$ and $G^{r}_{\mathrm{nLC}}\Big|_{z,z'=a}$ are the elements of the retarded Green's function of the upper barrier at the interface points with the QD cylinder. The self-energy of the lower barrier is given by

$$\Sigma^{r}_{\mathrm{n0}} = \tau^{\dagger}\left[EI - H_{\mathrm{nL0}} - \Sigma^{r}_{\mathrm{nR0}} \right]^{-1} \tau[r_{\mathrm{L}}] = t^2 G^{r}_{\mathrm{nL0}}\Big|_{z,z'=ZL-a}[r_{\mathrm{L}}], \tag{5.13}$$

where H_{nL0} is the Hamiltonian of the isolated lower barrier, $\Sigma^{r}_{\mathrm{nR0}}$ is the portion of self-energy of the semi-infinite layer Σ^{r}_{nR}, from $z=0$ to $z=ZL$, coupled to the lower GaAs barrier at $r=R-a$ and $G^{r}_{\mathrm{nL0}}\Big|_{z,z'=ZL-a}$ are the elements of the retarded Green's function of the lower barrier at the interface points with the QD cylinder. After coupling these self-energies to the Hamiltonian of the QD, it becomes easier to obtain the retarded Green's function and the spectral function by inverting a relatively smaller matrix dimension, instead of dealing with the very big matrix required by including the QD and the barriers, in a single matrix Hamiltonian.

By assuming quasi-equilibrium conditions in the contact layers, the scattering rates are directly related to the self-energies calculated above by the expression [79]

$$\Sigma_n^<(E) = if(E)\Gamma_n(E) \text{ and } \Sigma_n^> = -i\big(1-f(E)\big)\Gamma_n(E), \tag{5.14}$$

where $f(E)$ is the Fermi function where the states are occupied according to the quasi-Fermi level of the contact layers and $\Gamma_n(E)$, the transition rates, is related to the self-energy by

$$\Gamma_n = \mathrm{i}\left(\Sigma_n^r - \Sigma_n^a\right). \tag{5.15}$$

The determination of the quasi-Fermi levels of the contact layers, which represents the boundary conditions of the problem, should be obtained by a self-consistent solution between the charge density of the device and potential energy as will be shown in the next section.

5.2.1.2. Interactions self-energy

The self-energy due to interactions depends on the types of interactions to be included and the degree of approximations to be made. The scattering functions due to electron-phonon interactions in the first order self-consistent Born approximation are given by [111]

$$\Sigma_{\text{int}}^<(E) = \int D(E')G^<(E-E')dE' \text{ and } \Sigma_{\text{int}}^>(E) = \int D(E')G^<(E+E')dE' \tag{5.16}$$

where D is the correlation Green's function of the phonons. For localized interactions, we have three cases for $D(E)$,

- $D(E) \sim \delta(E)$ for elastic scattering where there are no energy transitions,
- $D(E) \sim \delta(E \pm \hbar\omega_o)$ for Longitudinal optical scattering where $\hbar\omega_o$ is the optical phonon energy, and
- $D(E) \sim E^2\theta(\hbar\omega_D - E)$ for acoustic phonon scattering where $\hbar\omega_D$ is the acoustic phonon energy.

The dependence of the scattering functions and hence the self-energy on the Green's functions leads to the requirement of an iterative solution of the interactions and Green's functions. It is expected to have a reduced electron-phonon scattering in QDIP (the phonon bottleneck effect) due to the 3D confinement and large separation between the energy levels of the QD. The electron-electron interactions will be treated classically by including the average potential obtained by solving Poisson's equation at specific applied bias and including the QD layer's space charge, in the total potential energy used in the Hamiltonian. So for simplicity, in this model, the interaction is chosen to be constant, independent of energy and position, which broadens the energy levels equally according to the same scattering rates. The self-energy used in the model due to interactions is given by

$$\Sigma_{\text{int}}^{r} = -i\frac{h}{2\tau_{\varphi}}, \tag{5.17}$$

where τ_{φ} is the scattering time. The corresponding scattering functions are given by

$$\Sigma_{\text{int}}^{<}(E) = if(E)\Gamma_{\text{int}}(E) \text{ and } \Sigma_{\text{int}}^{>}(E) = -i(1-f(E))\Gamma_{\text{int}}(E), \tag{5.18}$$

where $\Gamma_{\text{int}} = \text{i}\left(\Sigma_{\text{int}}^{r} - \Sigma_{\text{int}}^{a}\right) = \frac{h}{\tau_{\varphi}}$.

5.3. POTENTIAL ENERGY & QUASI-FERMI LEVEL

The potential energy of the electron in the Hamiltonian is obtained by the summation of the band offsets of the conduction bands in Fig. 3-14 and the average potential energy due to the applied bias and the space charge of the QD layers. The average potential energy satisfies Poisson's equation with specific boundary conditions at the contacts. The Poisson's equation of the average potential can be expressed as

$$\frac{d^2U}{dz^2} = \frac{e^2}{\varepsilon}\left(N_D(z) - n(z)\right), \tag{5.19}$$

where N_D and n are the doping and electron densities inside the QD array. The boundary conditions at the n^+-GaAs contacts are 0 and eV_{bias}, where V_{bias} is applied bias. The electron charge density in the device is composed of the QD charge density localized in the QD layers and the charge density due to coupling with the contacts. The doping and QD electron densities are concentrated in the QDs and the wetting layers and hence can be approximated by δ functions at the positions of the QD layers. The electron densities due to coupling with the left and right contacts, n_L and n_R respectively, are obtained from the average density of states due to the coupling with the contacts which are occupied according to the Fermi levels of the corresponding contacts. So the doping and electron densities can be written as

$$N_D(z) = \sum_{k=1}^{M} \Sigma_D\, \delta(z - kW) \text{ and } n(z) = n_L(z) + n_R(z) + \sum_{k=1}^{M} \Sigma_{QD}\, N_k \delta(z - kW), \tag{5.20}$$

where W is the separation between QD layers, M is the number of QD layers, Σ_D is sheet doping density, Σ_{QD} is the QD density and N_k is the average number of electrons per dot in the k-layer. Since the charge densities n_L and n_R depend on the average density of states which depend on the average potential energy through the device, a self-consistent solution between the charge density and potential should be obtained. The average number of electrons per dot is obtained by integrating the product of the density of states of the QD, which is assumed to be the same for all QDs in all layers, and the Fermi function, and it is given by

$$N_k = \int D(E) f_k(E) dE\,. \tag{5.21}$$

The states are occupied according to a local quasi-equilibrium Fermi level. According to the discussions of the capture rates and average occupations of QDs

by electrons in different QD layers in [69], when the energy relaxation length of electrons in the QD array is comparable to or longer than the array length, the average electron energy and capture rates are determined by the average electric field throughout the device. So in the model described in this chapter, the quasi-Fermi level during the iterative solution of the potential and the charge density will be adaptively modified such that it keeps uniform electron occupation through the QD arrays and be continuous with the equilibrium Fermi levels at the contacts. So in the middle of the device, the quasi-Fermi level will follow the average potential energy keeping the separation between them constant value. This constant value is taken to be the same as the separation between the maximum value of the potential, and the value of the Fermi level in the contact that has the higher potential. However near the contacts, the separation between the average potential and quasi-Fermi changes such that they equal their corresponding values in the thermal equilibrium contacts.

Assuming a constant Fermi level in the contacts leads to having zero current inside the contacts $\mathbf{J} = -\sigma \nabla E_f$ while there is a current inside the device which is injected from the contacts. This non-conservation of the current is due to fixing the values of the Fermi levels at the device-contact interface and deeply inside the contacts. Actually the Fermi level is not constant at the interface and the current decays exponentially deep inside the contacts. However, assuming equilibrium boundary conditions simplifies the solution. More discussion on boundary conditions can be found in [112, 115]. Therefore, the current will be calculated in the central period of the QD array where the electric field equals its average value $E = V_{\text{applied}} / L_{\text{device}}$.

The charge densities due to coupling with the contacts are given by [115]

$$n_{\mathrm{L}}(z) = \int f_{\mathrm{L}}(E) \left\langle A_{\mathrm{L}}^{\mathrm{1D}}(z;E) \right\rangle dE \text{ and } n_{\mathrm{R}}(z) = \int f_{\mathrm{R}}(E) \left\langle A_{\mathrm{R}}^{\mathrm{1D}}(z;E) \right\rangle dE , \qquad (5.22)$$

where $\left\langle A_{\mathrm{L}}^{1\mathrm{D}}(E)\right\rangle$ and $\left\langle A_{\mathrm{R}}^{1\mathrm{D}}(E)\right\rangle$ are the average density of states due to coupling with the left and right contacts respectively, and f_{L} and f_{R} are the equilibrium Fermi functions of the contacts. The average density of states is given by [111]

$$\left\langle A_{\mathrm{L,R}}^{1\mathrm{D}}(z;E)\right\rangle = \frac{m}{2\pi\hbar^2}\int_{-\infty}^{E} A_{\mathrm{L,R}}^{1\mathrm{D}}(z;E')dE', \tag{5.23}$$

where

$$A_{\mathrm{L,R}}^{1\mathrm{D}} = G_{1\mathrm{D}}^{r}\Gamma_{\mathrm{L,R}}G_{1\mathrm{D}}^{a}. \tag{5.24}$$

The 1D Green's function is given by

$$\left[E+\frac{\hbar^2}{2m}\frac{d^2}{dz^2}-U(z)-\Sigma_{\mathrm{L}}^{r}-\Sigma_{\mathrm{R}}^{r}\right]G_{1\mathrm{D}}^{r}(z,z';E)=\delta(z-z'), \tag{5.25}$$

where $\Sigma_{\mathrm{L,R}}^{r}$ and $\Gamma_{\mathrm{L,R}}$ are the 1D self-energies and the corresponding transition rates due to coupling with the left and right contacts and they are defined and calculated before in chapter 4 when the 1D transmission function was calculated in Eq. (4.9). So the coupling between the Green's function and Poisson's equation through the potential energy and the charge density leads to the requirement of a self-consistent solution, as shown in the flow-chart in Fig. 5-2. The equations of Green's function and Poisson are solved numerically using the method of finite differences.

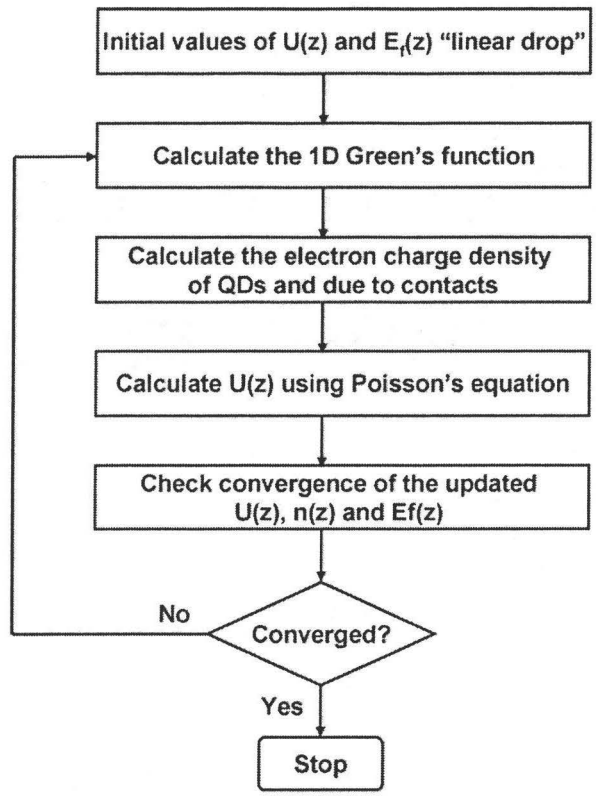

Figure 5-2 – Flow chart of the numerical solution of the electron density and average potential energy.

5.4. CURRENT CALCULATION

The terminal current per unit energy injected from a contact L in terms of the spectral function and lesser Green's function is given by [79]

$$i_{nL}(E) = \frac{e}{h}\mathrm{Tr}\left[\left(-i\Sigma_{nL}^{<}\right)A_n - \Gamma_{nL}\left(-iG_n^{<}\right)\right]. \tag{5.26}$$

Equation (5.26) can be used to calculate the current that exits the QD cylinder to the contact layer at z=0, crossing the double barrier structure adjacent to the QD. Since the interactions used in the model are constant, a simple form for the current can be obtained by substituting for $A_n = G_n^r\left(\Gamma_n + \Gamma_{int}\right)G_n^a$, $G_n^< = G_n^r\left(i\left(\Gamma_n + \Gamma_{int}\right)f_d\right)G_n^a$ and $\Sigma_{n0}^< = i\Gamma_{n0}f_0$ in Eq. (5.26), after which we get

$$i_{n0}(E)=\frac{e}{h}\mathrm{Tr}\left[\left(f_0\Gamma_{n0}\right)\left(G_n^r\left(\Gamma_n+\Gamma_{int}\right)G_n^a\right)-\Gamma_{n0}\left(G_n^r\left(\left(\Gamma_n+\Gamma_{int}\right)f_d\right)G_n^a\right)\right], \quad (5.27)$$

and this can be written as

$$i_{n0}(E)=\frac{e}{h}\mathrm{Tr}\left[\Gamma_{n0}G_n^r\left(\Gamma_n+\Gamma_{int}\right)G_n^a\right]\left(f_0-f_d\right)=\frac{e}{h}T_n(E)\left(f_0(E)-f_d(E)\right). \quad (5.28)$$

Equation (5.28) is the Landauer formalism which can be used to calculate the current. For constant interactions where we do not include electron-electron or electron-phonon interactions that cause transition between energy states, the NEGF gives a straightforward way of calculating the transmission function and hence the current which can be calculated from Eq. (5.28). When including non-constant interactions, the current should be calculated from the general equation (5.26). In equation (5.28), f_0 and f_d are the Fermi functions corresponding to the quasi-Fermi level of the contact layer at z=0 and at the QD. From the wetting layer to the top of the cylinder, through the QD height, the quasi-Fermi level of the dot is kept the same as its average value in the middle of the QD. The transition rate Γ_n used in Eq. (5.28) includes the transition rates of the contact layers from the wetting layer to the top of the cylinder at r=R and z=Zc. The total current per unit energy and the transmission function are obtained by the sum over all the values of the quantum number n and is given by

$$i_0(E)=\sum_n i_{n0}(E) \text{ and } T(E)=\sum_n T_n(E). \quad (5.29)$$

The total current exit the cylinder and the current density of the device are given by

$$I_0=\int i_0(E)dE \text{ and } J=\frac{I_0}{\pi R^2}. \quad (5.30)$$

5.5. RT-QDIP DARK CURRENT RESULTS

The self-energies of the contact layers coupled to the QD Hamiltonian at the interface surfaces at $r=R$, $z=Zc$ and $z=0$, which are Σ^{r}_{nR}, Σ^{r}_{nC} and Σ^{r}_{n0} are calculated from Eqs. (5.11), (5.12) and (5.13) respectively. The self-energy of the semi-infinite contact layer Σ^{r}_{nR} has an analytical solution as shown in chapter 3, while Σ^{r}_{nC} and Σ^{r}_{n0} are calculated numerically. The interaction self energy $\Sigma^{r}_{int} = -i\Gamma_{int}/2$ is taken the same for all points inside the cylinder where $\Gamma_{int} = h/\tau_{\varphi} = 2$ meV corresponding to scattering time $\tau_{\varphi} = 3.3$ ps. The matrix representation of the spectral function can be used to obtain the DOS such that $D(E) = \sum_{j=1}^{N_r}\sum_{k=1}^{N_z} ja \times A(ja, ka; E)$. Figure 5-3 shows the calculated DOS of the QD in both bound and continuum energy ranges. As shown in the inset of Fig. 5-3, there are three bound states lying below the conduction band edge of GaAs, zero level, and the continuum part of the DOS contains the contributions of the resonant levels in the quantum well in addition to localized states due to the QD potential.

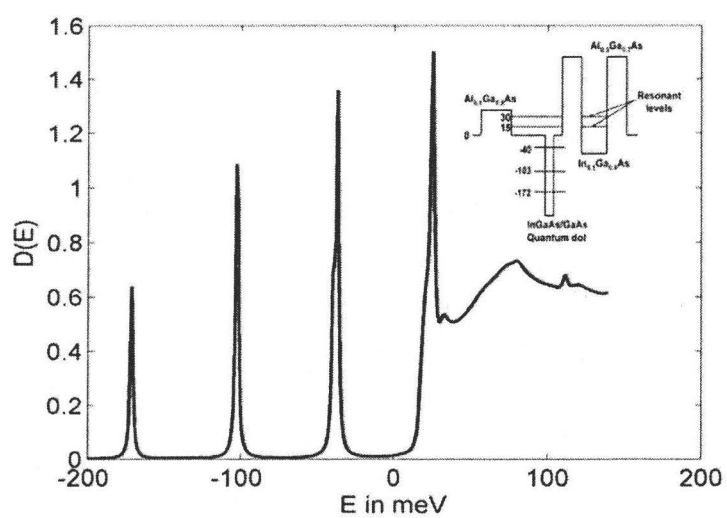

Figure 5-3 – The DOS vs energy E of the QD. The inset illustrates the position of the bound states of the QD and the resonant levels in the quantum well relative to the CB of GaAs.

The DOS shown in Fig. 5-3 is used to calculate the average number of electrons per dot from Eq. (5.21) which is used in calculating the average potential energy using Poisson's equation. The Fermi levels in the (n+ GaAs) contacts are obtained from $n_{\text{contact}} = N_C e^{-\left(\frac{E_C - E_f}{kT}\right)}$, where $n_{\text{contact}} = 2\times10^{18}$ cm^{-3} is the doping density, N_C is the effective density of states in the conduction band of GaAs, which is temperature dependent, and E_C is the conduction band energy of GaAs which is taken to be zero. At all applied biases and temperatures, an iterative solution of the average potential energy, quasi-Fermi level and electron charge density is obtained as described in the model according to the flow chart of Fig. 5-2.

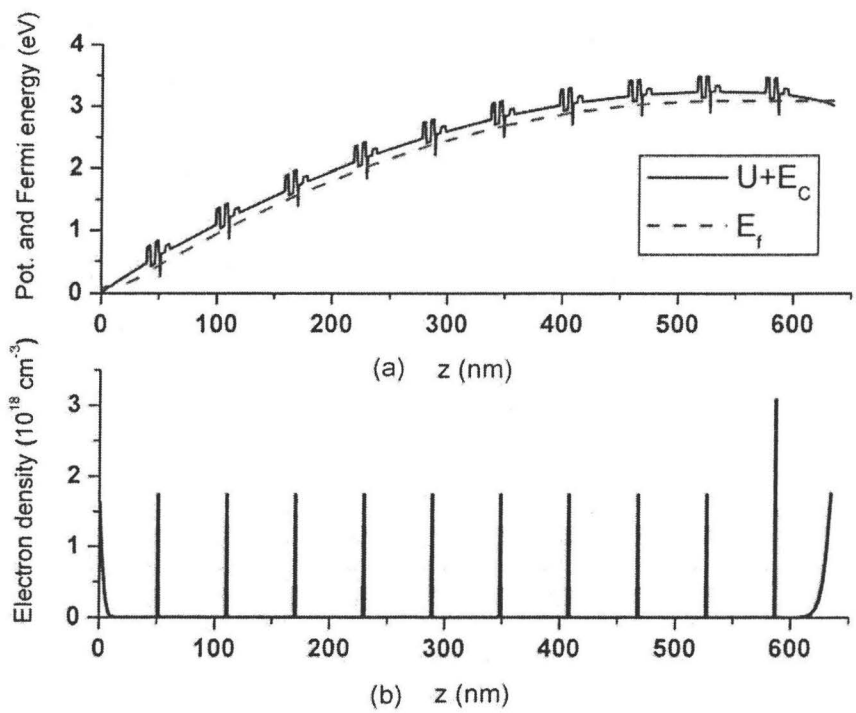

Figure 5-4 – (a) The average potential energy including the band offset variations and the quasi-Fermi level profile through the device at an applied bias of 3 V and T = 160K. (b) The average electron charge density of the QD array, including charge density due to coupling with the contacts, is given at an applied bias of 3 V and T = 160K.

The average potential energy, quasi-Fermi level and electron charge density are shown in Fig. 5-4. The results presented in Fig. 5-4 are obtained at a temperature T of 160 K and the applied bias of 3 volts. The results show that the QD layers are uniformly occupied by electrons and the QD layers near the right contact are in thermal equilibrium with the contact as their quasi-Fermi level equals the Fermi level of the contact to satisfy the boundary conditions and to have the charge density at the device contact interface equal to the electron charge density just inside the contact for charge continuity. The variation of the band offsets is added to the average potential energy to illustrate the positions of the QD layers. In the central QD layer, the electric field almost equals its average value $V_{\text{applied}} / L_{\text{device}}$. The average potential energy and quasi-Fermi level of the central QD period calculated at a specific value of applied bias and temperature are used to calculate the total electron potential energy and scattering functions of the contact layers and interactions. The average potential energy is added to the band offset variation shown in Fig. 3-14 to obtain the potential energy used to calculate the Hamiltonian of the QD cylinder. The quasi-Fermi level is used to calculate the scattering functions $\Sigma^{<}$ and $\Sigma^{>}$ of the contact layers and interactions from Eq. (5-14) and Eq. (5-18) respectively.

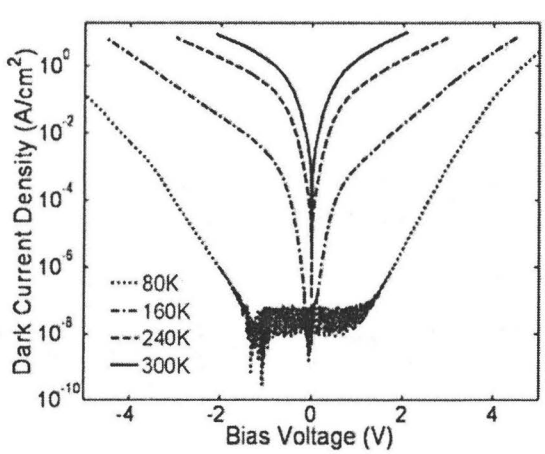

Figure 5-5 – Measured dark current density as a function of bias in the temperature range 80-300 K [47].

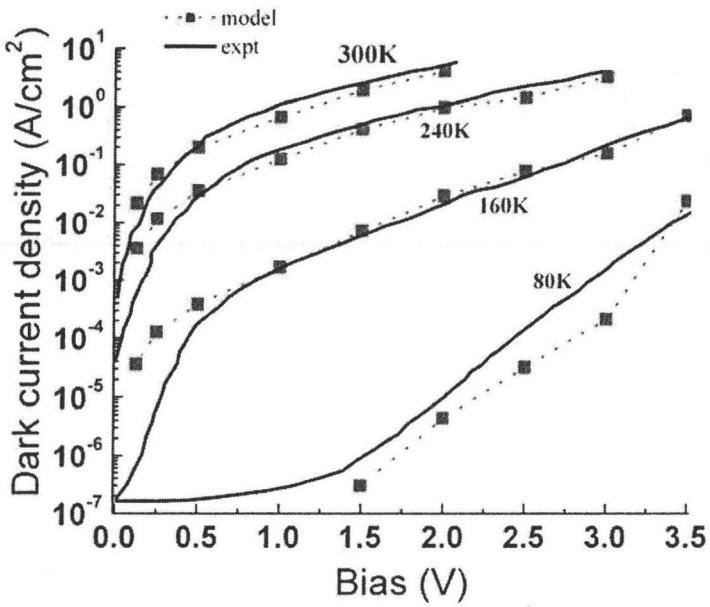

Figure 5-6 – Comparison between the calculated dark current density by the model and experimentally measured ones at various temperatures.

Experimental results of the dark current density of RT-QDIP as a function of applied bias and temperature are shown in Fig. 5-5 and are from Ref. [47]. A slight asymmetry of the measured dark current with opposite bias polarities can be due to the asymmetry of the dot heterostructure. The dark current density calculated from our model as a function of the applied bias and various temperatures are compared with the experimental results in Fig. 5-6. The experimental data used in Fig. 5-6 are extracted from Fig. 5-5. The results of the model show good agreement with the experimental results, especially for bias values above 0.5 Volt. The sensitivity of calculating the average potential energy and quasi-Fermi level on the electron charge density is larger at small bias values than for large biases. The average electron charge density in the device is calculated from Eqs. (5.21) and (5.22) using numerical integration with respect to energy. The energy step used is 1 meV and since increasing the temperature makes it small compared to kT, the accuracy of the numerical integrations used to calculate the charge density and the dark current increases with increasing

temperature. Also the convergence criteria chosen in obtaining the average potential energy and quasi-Fermi level using the flow-chart in Fig. 5-2 is to have a relative error of 1 percent in the calculated quantities. The same tolerance, grid step and energy step are used in the calculations of the dark currents for all bias values and temperatures. Improving the accuracy of the results can be achieved by decreasing the values of the tolerance and grid step used in addition to using smaller energy steps. This enables calculating the dark current and electron density at more energy values which improves the accuracy, but this requires significantly more memory usage and longer processing/computation time.

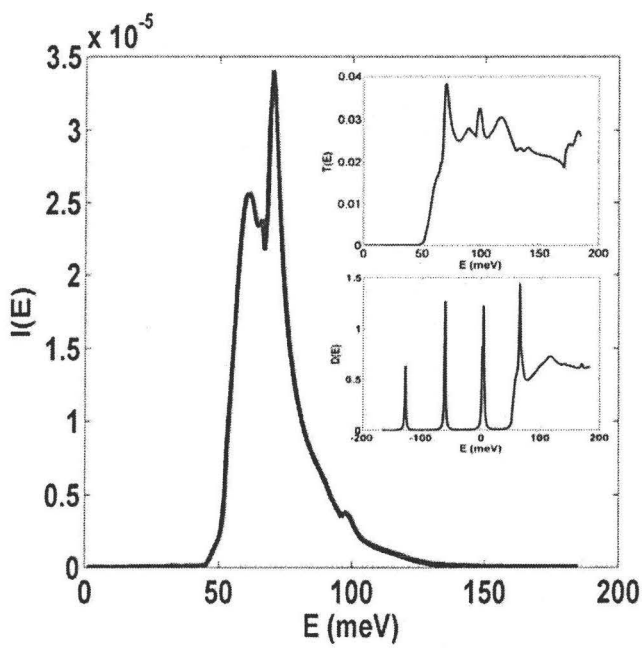

Figure 5-7 – The current exiting the QD cylinder per unit energy at T=160 K and bias=0.5 V. The inset shows the transmission function and the DOS at the same bias and temperature values.

Figure 5-7 shows the current per unit energy that exits the QD cylinder at an applied bias of 0.5 volts and a temperature T of 160 K. The inset shows the transmission function from the wetting layer to the cylinder surface at z=0 through the double barrier structure and the DOS. The current curve has its peak at the position of the resonant levels in the quantum well above the QD. The splitting of

the peak of the current density per unit energy is due to resonant tunneling through the energy levels of the QW above the QD. The separation between the two peaks is comparable to the separation between the energy levels of the QW appeared as two step functions in Fig. 3-18. The QD bound state appeared in the continuum part of the spectrum of the DOS in the inset has also contributions on the shape of the current density peak.

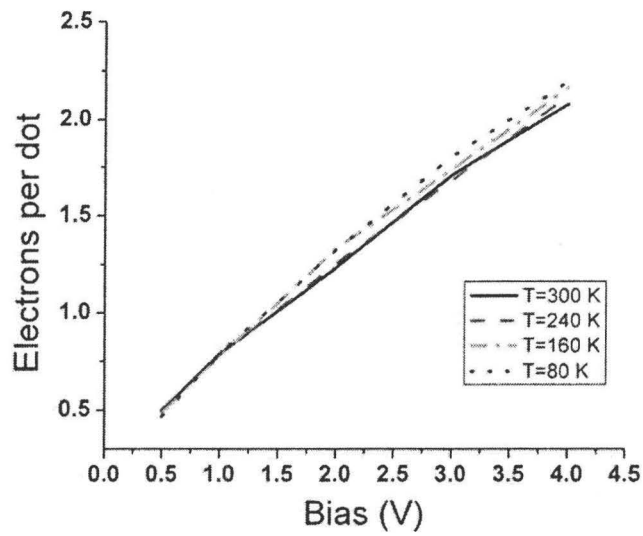

Figure 5-8 – The average number of electrons per dot as a function of applied bias at different temperature values.

To improve the performance of the detector, the dependence of the responsivity and dark current on different design parameters should be obtained and optimized. Concerning the dark current, quantitative theoretical predictions of the dark current characteristics for different design parameters are given. The model has been used to study the effect of changing the design parameters on the dark current and to extract internal information about carrier distribution in QDs at different bias voltages and temperatures. The effect of varying the applied bias and temperature on the number of electrons occupying the QD is shown in Fig. 5-8. The results show an increase of the average number of electrons per dot with the applied bias, however there is no significant change with temperature at a

specific value of bias. From the dark current results of Fig. 5-6, there is significant increase of the current with bias and temperature.

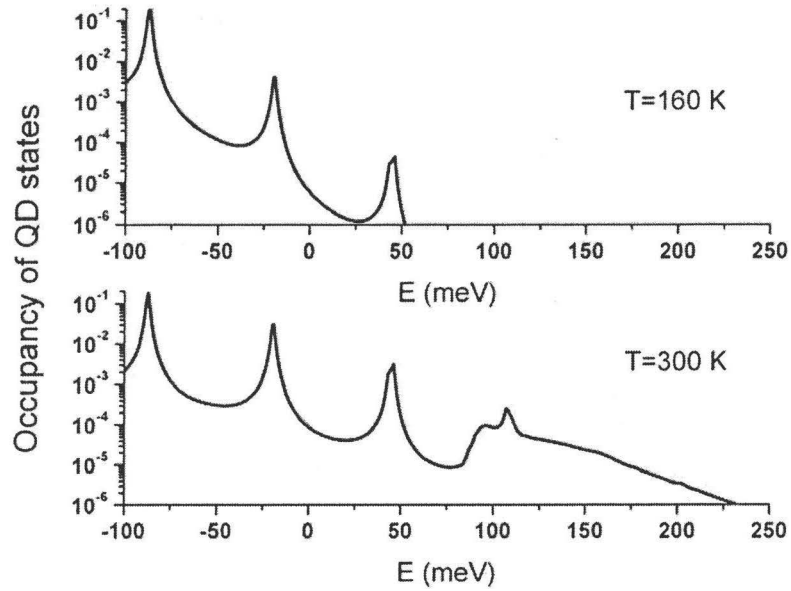

Figure 5-9 – Occupation of QD states as a function of electron energy at bias=1 V and T=160 K and 300 K.

In order to illustrate how the average number of electrons per dot almost does not change with temperature while the dark current increases significantly with temperature, the occupancy of QD states or the number of electrons per unit energy which is given by $n(E)=\sum_{j=1}^{N_r}\sum_{k=1}^{N_z} ja \times n(ja,ka;E)$ is calculated. Figure 5-9 shows the occupancy of the QD bound and continuum states at an applied bias of 1 V and at T=160 K and 300 K. The total number of electrons is almost the same; however, increasing the temperature leads to redistribution of electrons among the states such that the bound states of high energies and the continuum states become more occupied at higher temperatures, which leads to an increase in the dark current. The peaks appeared in fig. 5-9 are corresponding to the bound states of the QD as appeared in the DOS in Fig. 5-3. However, the positions of the peaks in Fig. 5-9 are shifted due to the applied bias which increases the average potential

energy and hence shift the energy levels of the QD. Figure 5-10 shows the occupancy of QD energy states at a temperature of 160 K and bias values 0.5 V and 3 V. Increasing the applied bias leads to an increase of the occupancy of all bound and continuum states as a result of the shift of the QD Fermi level toward the conduction band edge. The broadening of the Lorentzian shape of the occupancy of the QD states is dependent on the value of Γ_{int}. The value of Γ_{int} used in the model is 2 meV. Using larger values makes the shape of the levels broader and smaller values gives narrower levels. The broadening of the levels is related to the scattering time.

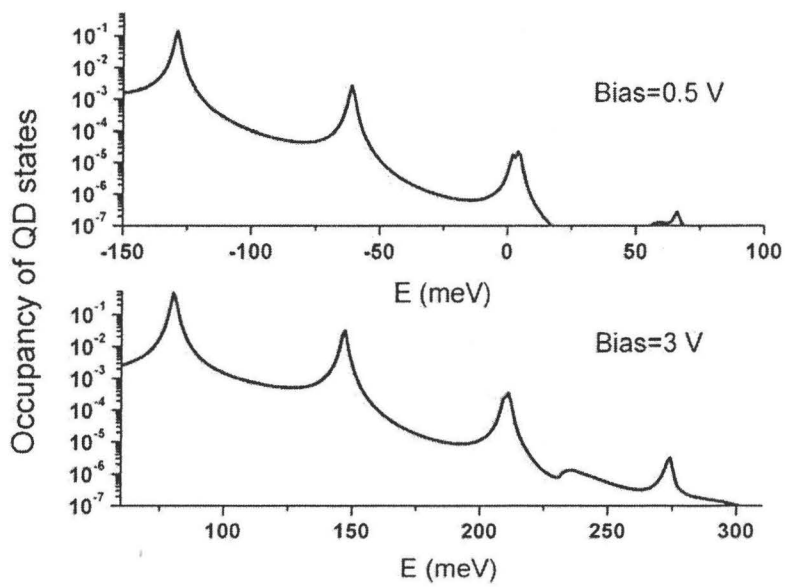

Figure 5-10 – Occupation of QD states as a function of electron energy at T=160 K and bias=0.5 V and 3 V.

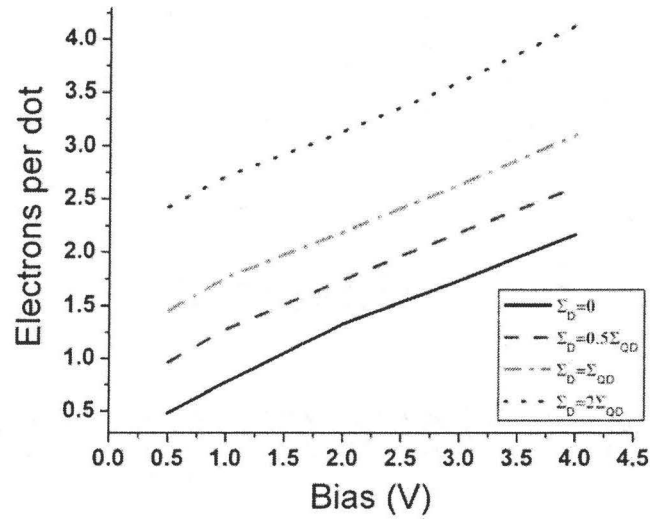

Figure 5-11 – The average number of electrons per dot as a function of applied bias at different doping densities.

The model is also used to study the effect of varying the doping density, barrier separation between QD layers and number of QD layers on the dark current characteristics. Figure 5-11 shows the effect of using different doping densities on the QD average occupation number of electrons. Four different QD sheet doping densities are used. The doping densities used are defined relative to the QD density such that $\Sigma_D / \Sigma_{QD} = 0$ for undoped layers in the experimental results shown in Fig. 5-5. Also given are the occupation numbers for $\Sigma_D / \Sigma_{QD} =$ 0.5, 1 and 2. The dark current density at the various doping levels as a function of bias is shown in Fig. 5-12. The dark current at 0.5 V shows an increase of almost one and two orders of magnitude corresponding to increasing the relative doping density from 0 to 1 and to 2 respectively. The increase in the current becomes less for higher applied biases.

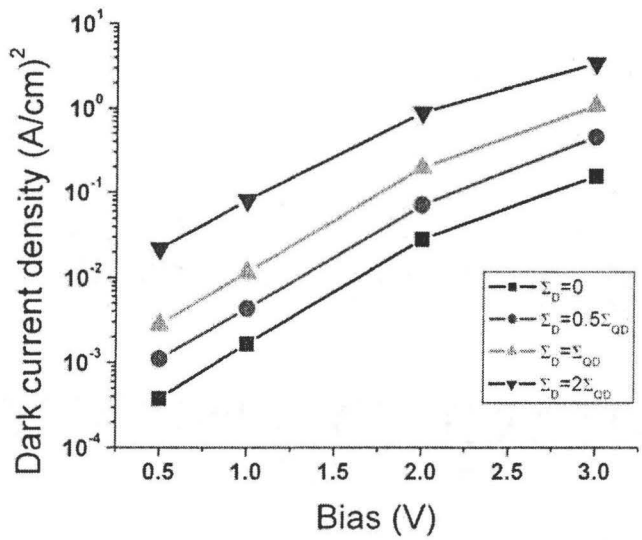

Figure 5-12 – Dark current density vs. applied bias at T=160 K and at different doping densities.

Figures 5-13 and 5-14 show the variation of the dark current density vs. applied bias with varying the barrier separation between the QD layer and the number of QD layers respectively. Increasing the barrier separation between QD layers or increasing the number of QD layers leads to a decrease of the dark current due to the decrease of the average electric field inside the device. The variation of the dark current becomes more pronounced at higher applied biases.

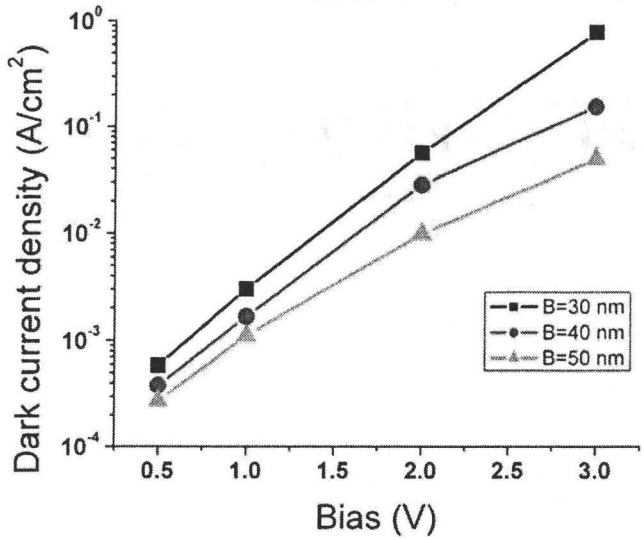

Figure 5-13 – Dark current density vs. applied bias at T=160 K and at different barrier separations, B.

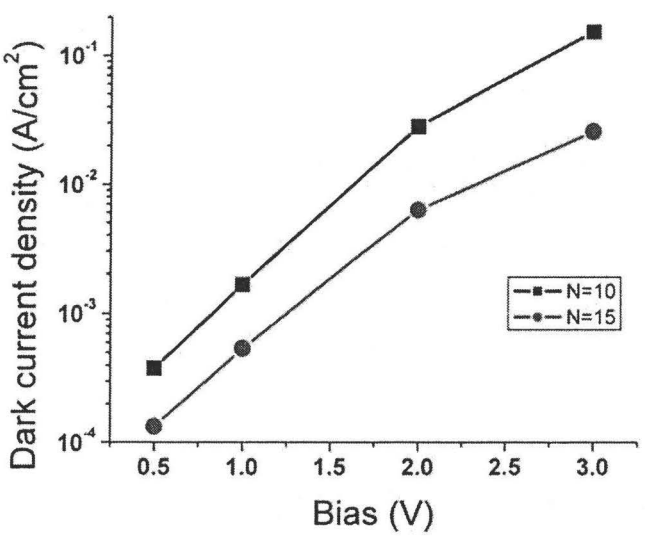

Figure 5-14 – Dark current density vs. applied bias at T=160 K and at number of QD layers=10 and 15.

CHAPTER 6 PHOTOCURRENT MODELING

Improving the responsivity and detectivity of QDIPs will enhance the detector performance and allow for the detection of low level optical input signal and operation at higher temperature. Optimizing the responsivity and detectivity requires obtaining the dark and photocurrent characteristics of the detector for different design parameters such as the QD doping density and the separation between QD layers. Theoretical models to study the current characteristics of QDIP under dark and illumination conditions have been made [64-69]. The current is calculated from a classical transport equation that includes balanced thermal and photoexcitation rates, and capture rates that are calculated classically with fitting parameters obtained by comparison with experimental results. The semi-classical Boltzmann equation model was used in [70, 71] to calculate the dark current and responsivity of a planar array QDIP structure. The microscopic device structure was used to calculate the electronic wavefunctions for calculating the thermal and optical transitions which are used to determine the current. Using a quantum transport model to obtain the current characteristics in QDIPs is preferable since it fairly describes the quantum transport phenomenon playing a significant role in the performance of such nano-devices, such as resonant tunneling and quantum interference, and considers the microscopic device structure including the shape and size of QDs, heterostructure device structure and doping density.

Theoretical modeling of the photocurrent of a resonant tunneling (RT) quantum dot infrared photodetector (QDIP) based on the non-equilibrium Green's function (NEGF) is presented in this chapter. The interaction with light used in

the model is based on the first order dipole approximation and the Fermi-golden rule which is used to obtain the transition rates due to photon emission or absorption. The bound states of the QD are obtained by solving numerically the eigenvalue problem of the Hamiltonian of the QD, while the continuum states are obtained from the retarded Green's function. The in-scattering and out-scattering self-energy functions due to photon interactions are calculated from the total transition rate and the quasi-Fermi level of the QD. The Green's functions of the QDs are obtained by numerically solving their governing kinetic equations using the method of finite differences. A quantum transport equation using the Green's functions is formed to calculate the dark and photocurrent. The model has been applied to simulate the dark current and responsivity of the RT-QDIP at different temperatures and applied biases. The simulated dark current and responsivity with this model are in good agreement with experimental results. The model was used to study the effect on the dark current and the responsivity due to changing the QD doping density and the barrier separation between QD layers. The detectivity of the detector is obtained for different design parameters to get the best performance

6.1. GREEN'S FUNCTION MODEL

In cylindrical coordinates representation, the retarded Green's function of the system including local interactions is given as [111]

$$\left[E - H_{\text{op}} - \Sigma^{r}_{\text{int}}(r,z;E)\right] G^{r}(r,r';\theta,\theta';z,z';E) = \frac{1}{r}\delta(r-r')\delta(\theta-\theta')\delta(z-z'), \quad (6.1)$$

where the Hamiltonian operator of the system in cylindrical coordinates is given by

$$H_{\text{op}} = -\frac{\hbar^2}{2}\left(\frac{1}{r}\frac{\partial}{\partial r}\frac{r}{m^{r}(r,z)}\frac{\partial}{\partial r} + \frac{1}{m^{r}(r,z)}\frac{1}{r^2}\frac{\partial^2}{\partial\theta^2} + \frac{\partial}{\partial z}\frac{1}{m^{z}(r,z)}\frac{\partial}{\partial z}\right) + V(r,z). \quad (6.2)$$

For a cylindrically symmetric system as in the case of conically shaped QD-based RT-QDIP, the potential energy in the vicinity of QDs $V(r,z)$, in Eq. (6.2), is

invariant under rotation around QD axis and can be considered independent of rotation angle θ. By considering that the interactions with the light and the lattice are only local, the self-energy $\Sigma^r_{\text{int}}(r,z;E)$, in Eq. (6.1), can be considered independent of rotation angle θ. Therefore, the dimensions of the problem can be reduced from 3D to a two-dimensional problem which simplifies the numerical calculations. In Eq. (6.2), $V(r,z)$ is the potential energy seen by the electron and is given by the summation of the conduction band offsets between the QD material and the surrounding barrier materials, and the average potential energy satisfying Poisson's equation at a specific applied bias as shown before in chapter 5. The Green's function can be written as

$$G^r(r,r';\theta,\theta';z,z';E) = \frac{1}{2\pi}\sum_n e^{in(\theta-\theta')} G^r_n(r,r';z,z';E),\ n \text{ is an integer.} \qquad (6.3)$$

The retarded Green's function at a specific quantum number n can be obtained by substituting (6.3) into (6.1) and following the same procedure used before in chapter 5 to replace the contact layers by self-energy, we get

$$\left[EI - H_{\text{n}} - \Sigma^r_{\text{n}} - \Sigma^r_{\text{int}}\right] G^r_{\text{n}} = [r]^{-1}, \qquad (6.4)$$

where H_{n} is the matrix representation of the Hamiltonian obtained using the finite differences applied to H_{op} defined in Eq. (6.2) after replacing $\left(\partial^2/\partial\theta^2\right)$ by $\left(-n^2\right)$. The subscript n represents the quantum number associated with z-component of total angular momentum and all matrices corresponding to the Hamiltonian, self-energies and Green's functions are calculated at a specific value of n. The term $[r]$ is a diagonal matrix whose diagonal elements are the radial part of the position vector of the electron inside the cylinder. The Hamiltonian matrix H_{n} is the non-interacting Hamiltonian of an isolated cylinder encompassing one QD. Zero boundary conditions are taken for H_{n} at the cylindrical surface, and so the coupling between the QD inside the cylinder and

the surrounding contact layers at specific n, is compensated by adding the self-energy Σ_{n}^{r} at the cylindrical surface. The internal interactions inside the cylinder, electron-photon interaction and interaction with the lattice, are assumed to be localized. The interaction with light is modeled using the first order dipole approximation and the Fermi golden rule, and it depends on n, while the interaction with the lattice is taken to be constant, independent on energy and position as assumed before in chapter 5. The localized interactions are given by the self-energy $\Sigma_{\mathrm{int}}^{r}=\Sigma_{\text{n-light}}^{r}+\Sigma_{\text{lattice}}^{r}$, which is the summation of the interaction with light and lattice respectively. From the retarded Green's function, the localized density of states is calculated from

$$\begin{aligned} A(r,z;E) &= -2\,\mathrm{Im}\left[G^{r}(r,r;\theta,\theta;z,z;E)\right] \\ &= -\frac{1}{\pi}\sum_{\mathrm{n}}\mathrm{Im}\left[G_{\mathrm{n}}^{r}(r,r;z,z;E)\right]=\sum_{\mathrm{n}}A_{\mathrm{n}}(r,z;E) \end{aligned} \tag{6.5}$$

The lesser and greater Green's functions are given by

$$\begin{aligned} G_{\mathrm{n}}^{<} &= G_{\mathrm{n}}^{r}\left(\Sigma_{\mathrm{n}}^{<}+\Sigma_{\text{n-light}}^{<}+\Sigma_{\text{lattice}}^{<}\right)G_{\mathrm{n}}^{a} \\ G_{\mathrm{n}}^{>} &= G_{\mathrm{n}}^{r}\left(\Sigma_{\mathrm{n}}^{>}+\Sigma_{\text{n-light}}^{>}+\Sigma_{\text{lattice}}^{>}\right)G_{\mathrm{n}}^{a} \end{aligned}, \tag{6.6}$$

where the $\Sigma^{<}$ and $\Sigma^{>}$ are the lesser and greater self-energies corresponding to the in-scattering and out-scattering processes, respectively. The calculations of these functions will be given in the next section. The electron and hole densities per unit energy are related to the lesser and greater Green's functions, and are given by

$$\begin{aligned} &n(r,z;E)=\left(-i/2\pi\right)\sum_{\mathrm{n}}G_{\mathrm{n}}^{<}(r,r;z,z;E), \\ &\text{and} \\ &p(r,z;E)=\left(i/2\pi\right)\sum_{\mathrm{n}}G_{\mathrm{n}}^{>}(r,r;z,z;E) \end{aligned} \tag{6.7}$$

6.1.1. CALCULATING THE SELF-ENERGY

The self-energy $\left(\Sigma^{r}\right)$ and scattering functions $\left(\Sigma^{<} \text{ and } \Sigma^{>}\right)$ in the cylindrical system that include one QD inside have contributions from the coupling with surrounding contact layers outside the cylinder, and the internal interactions with the lattice and the light. Assuming that these sources are independent, the self-energy and scattering functions can be written as

$$\Sigma^{r} = \Sigma^{r}_{\text{n-cl}} + \Sigma^{r}_{\text{n-light}} + \Sigma^{r}_{\text{lattice}},$$
$$\text{and} \qquad (6.8)$$
$$\Sigma^{<} = \Sigma^{<}_{\text{n-cl}} + \Sigma^{<}_{\text{n-light}} + \Sigma^{<}_{\text{lattice}} \text{ and } \Sigma^{>} = \Sigma^{>}_{\text{n-cl}} + \Sigma^{>}_{\text{n-light}} + \Sigma^{>}_{\text{lattice}}.$$

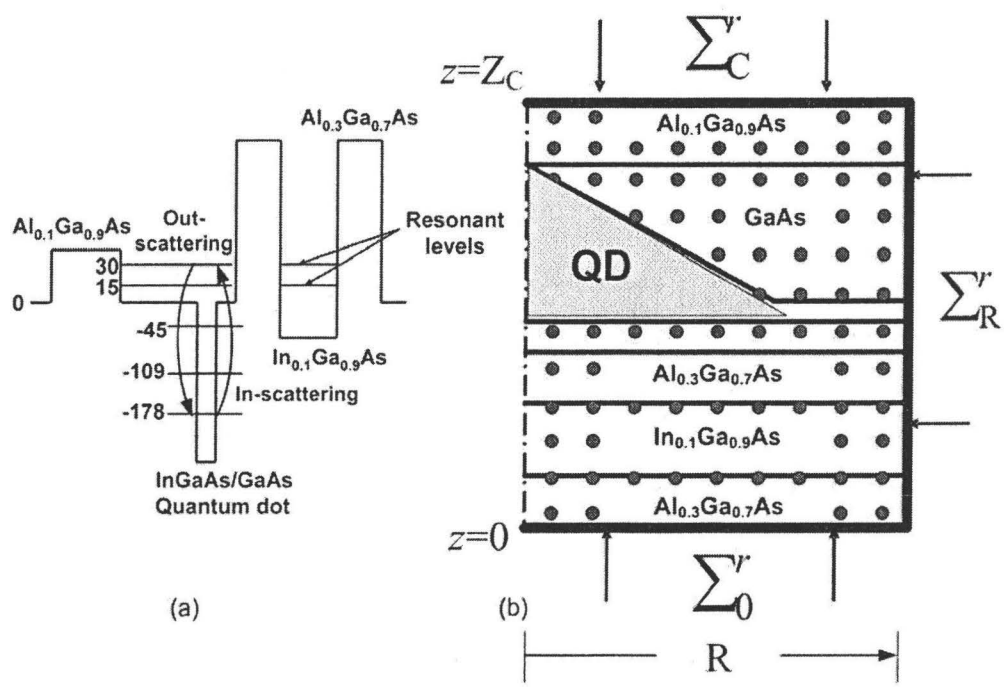

Figure 6-1 – (a) Schematic of the conduction band profile of the RT-QDIP demonstrating the heterostructure of one QD layer and the energy levels of the QD and the quantum well (in meV), relative to CB bottom in GaAs; the QD composition is $In_{0.4}Ga_{0.6}QAs$. (b) Schematic of the lattice grid in *r*-*z* plane used in the numerical simulation. The surrounding contact layers are replaced by self-energies at the interface planes of the QD cylinder.

6.1.1.1. Contact layers self-energy

The self-energy due to coupling with the contact layers at a specific value of n at the cylindrical surface as shown in Fig. 6-1 is given by [74, 75]

$$\Sigma^{r}_{\text{n-cl}} = \tau^{\dagger}\left[EI - H_{\text{nL}}\right]^{-1}\tau[r_{\text{L}}], \tag{6.9}$$

where τ is the coupling matrix whose elements are zero every where except at the interface points inside the contact layers adjacent to the points inside the QD cylinder and H_{nL} is the Hamiltonian of the isolated contact layer. The calculations of the self-energies Σ^{r}_{0}, Σ^{r}_{C}, and Σ^{r}_{R}, at the cylindrical surfaces $z = 0$, $z = Z_{\text{C}}$, and $r = R$ respectively, from Eq. (6.9) have been shown in chapter 5. By assuming that the contact layers are at quasi-equilibrium conditions, then the scattering rates are directly related to the self-energies calculated above by the expression [79]

$$\Sigma^{<}_{\text{n-cl}}(E) = if(E)\Gamma_{\text{n-cl}}(E) \text{ and } \Sigma^{>}_{\text{n-cl}} = -i\left(1-f(E)\right)\Gamma_{\text{n-cl}}(E), \tag{6.10}$$

where $f(E)$ is the Fermi function where the states are occupied according to the quasi-Fermi level of the contact layers and $\Gamma_{\text{n-cl}}(E)$, the transition rates, is related to the self-energy by

$$\Gamma_{\text{n-cl}} = \text{i}\left(\Sigma^{r}_{\text{n-cl}} - \Sigma^{a}_{\text{n-cl}}\right). \tag{6.11}$$

The determination of the quasi-Fermi levels of the contact layers, which represents the boundary conditions of the problem, should be obtained by a self-consistent solution between the charge density of the device and potential energy as shown in chapter 5.

6.1.1.2. Interactions self-energy

In this model, for simplicity, the self-energy due to interactions with the lattice is chosen to be constant, independent of energy and position, which

broadens the energy levels equally according to the same scattering rates. The self-energy used in the model due to interactions with the lattice is the same at every lattice point of the grid in Fig. 6-1, and is given by

$$\Sigma^{r}_{\text{lattice}} = -i\frac{h}{2\tau_{\varphi}}, \tag{6.12}$$

where τ_{φ} is the scattering time. The corresponding scattering functions are given by

$$\begin{aligned} \Sigma^{<}_{\text{lattice}}(E) &= if(E)\Gamma_{\text{lattice}}(E), \text{ and} \\ \Sigma^{>}_{\text{lattice}}(E) &= -i(1-f(E))\Gamma_{\text{lattice}}(E), \end{aligned} \tag{6.13}$$

where $\Gamma_{\text{lattice}} = \text{i}\left(\Sigma^{r}_{\text{lattice}} - \Sigma^{a}_{\text{lattice}}\right) = \frac{h}{\tau_{\varphi}}$. This simplified way of modeling the self-energy and scattering functions for lattice interaction inside the cylinder simplifies the calculations, since the self-consistent Born approximation of modeling the interactions with optical and acoustic phonons requires an iterative solution between the Green's function and the self-energy functions. The model assumes elastic scattering, since there is no energy transition between different energy states, and the transition between energy states through the in-scattering or out-scattering processes are assumed to be due to interaction with light through photon absorption and emission respectively.

The interaction with light is treated within the first order dipole approximation and Fermi golden rule, and the transition rate between an initial and final state due to photon absorption or emission is given by [109, 110]

$$\Gamma_{mn} = \alpha\left|\underline{e}.\left\langle\psi_m\left|e\underline{r}\right|\psi_n\right\rangle\right|^2 \delta\left(E_m - E_n - \hbar\omega\right), \tag{6.14}$$

where $\hbar\omega$ is the photon energy, E_{m} and E_{n} are the energies of the initial and final states, $\underline{e}$ is the polarization direction of the incident light, $\mu_{mn} = \underline{e}.\left\langle\psi_m\left|e\underline{r}\right|\psi_n\right\rangle$ is the electric dipole moment and α is the proportionality

constant which relates the transition rate to the imaginary part of the self-energy. The width of the broadening of an energy state described by the imaginary part of the self-energy gives the decay rate of this state. For a cylindrically symmetric problem, the wavefunctions can be assumed in the form

$$\Psi_n(r,\theta,z) = e^{in\theta}\varphi_n(r,z). \tag{6.15}$$

Therefore, for normal incidence light, the electric field is polarized in the in-plane directions, that is, x- or y-directions, and for example, for the x-polarized electric field, the dipole moment is given by

$$\begin{aligned}\mu_{mn} &= \underline{x}.\langle\psi_m|e\underline{r}|\psi_m\rangle = \langle e^{im\theta}\varphi_m(r,z)|ex|e^{in\theta}\varphi_n(r,z)\rangle \\ &= e\langle e^{i(n\pm1)\theta}\varphi_{n\pm1}(r,z)|r\cos\theta|e^{in\theta}\varphi_n(r,z)\rangle\end{aligned} \tag{6.16}$$

Equation (6.16) gives the selection rule for optical transition for normal incidence. The allowed energy transition between the bound and continuum states differ in the quantum number n by ±1, otherwise the integration over θ will make the dipole moment vanish. The bound states in the quantum dots are calculated by solving an eigenvalue problem assuming zero boundary conditions at the cylinder's surface, while the Green's function method is used to calculate the wavefunction in the continuum part as shown in chapter 4. The transition rate, which is the summation of the in-scattering and out-scattering rates, of the state with quantum number n and energy E, is given by

$$\Gamma_{\text{n-light}}(E) = \alpha\left|\underline{e}.\langle\psi_n(E)|e\underline{r}|\psi_{n\pm1}\rangle\right|^2\delta(E-E_{n\pm1}-\hbar\omega), \tag{6.17}$$

which gives the summation of the in-scattering transition rate ($-i\Sigma^{<}_{\text{n-light}}$) to the state ($n$, E) from the bound state in the QD, $\psi_{n\pm1}$, due to photon absorption, and the out-scattering rate ($i\Sigma^{>}_{\text{n-light}}$) from the state ($n$, E) to the bound state $\psi_{n\pm1}$ due to a photon emission. The corresponding scattering functions, assuming that the QD is occupied according to a quasi-equilibrium Fermi function are given by

$$\Sigma^{<}_{\text{n-light}}(E) = i\Gamma_{\text{n-light}}(E) f(E_{n\pm1}),$$
$$\text{and} \qquad (6.18)$$
$$\Sigma^{>}_{\text{n-light}}(E) = -i\Gamma_{\text{n-light}}(E)\left(1 - f(E_{n\pm1})\right).$$

The in-scattering function is the multiplication of the transition rate and the Fermi function at the bound state that gives the occupancy of the bound state assuming that the continuum state is empty, while the out-scattering function gives the capture rate from the assumed occupied continuum state to the empty bound state. The summation of the in-scattering and out-scattering functions gives the decay rate of the state, which is the total transition rate such that

$$\Gamma_{\text{n-light}}(E) = -i\Sigma^{<}_{\text{n-light}}(E) + i\Sigma^{>}_{\text{n-light}}(E), \qquad (6.19)$$

Equations (6.17), (6.18), and (6.19) show that the decay rate or the total transition rate of the state due to interaction with light is dependent only on the dipole moment and independent of temperature, while the in-scattering and out-scattering parts of the total transition rate depend on temperature through the Fermi function. The absolute value of the proportionality constant α was found to not affect the actual value of the responsivity which mainly depends on the ratio between the in-scattering and out-scattering functions and the total transition rate. Increasing the magnitude of this constant leads to a smoother responsivity curve without actually affecting its magnitude significantly. So choosing a suitable value for α, corresponding to decay rate of around ~100 meV, gives very acceptable results. The self-energy due to the interaction with the light is given as

$$\Sigma^{r}_{\text{n-light}}(E) = -i\Gamma_{\text{n-light}}(E)/2. \qquad (6.20)$$

The self-energy and scattering functions $\Sigma^{r}_{\text{n-light}}$, $\Sigma^{<}_{\text{n-light}}$, $\Sigma^{>}_{\text{n-light}}$, and $\Gamma_{\text{n-light}}$ given by equation (6.17), (6.18), and (6.20) are assumed to have non-zero values only at the gray area representing the QD, where photoexcitation and capture occur, and are zero elsewhere.

6.2. CURRENT CALCULATION

The terminal current per unit energy injected from a contact L at a specific quantum number n in terms of the lesser Green's function and the spectral function or the greater Green's function [111] is given by

$$\begin{aligned} i_{nL}(E) &= \frac{e}{h}\mathrm{Tr}\left[\left(-i\Sigma_{nL}^{<}\right)A_n - \Gamma_{nL}\left(-iG_n^{<}\right)\right] \\ &= \frac{e}{h}\mathrm{Tr}\left[\left(-i\Sigma_{nL}^{<}\right)\left(iG_n^{>}\right) - \left(i\Sigma_{nL}^{>}\right)\left(-iG_n^{<}\right)\right] \end{aligned} \quad (6.21)$$

Equation (6.21) gives the terminal current per unit energy that enters the QD cylinder from the contact layer L. It can be explained using simple arguments. In the first term $\left(-i\Sigma_{nL}^{<}\right)$ is the rate of in-scattering into an empty state from the contact layer L, and $\left(iG_n^{>}\right)$ is the density of empty states. Therefore, the first term gives the actual rate of in-scattering and in the same way, the second term gives the rate of out-scattering and the difference gives the net inflow of electrons. Equation (6.21) can be used to calculate the current that exits the QD cylinder to the contact layer at z=0, crossing the double barrier structure adjacent to the QD. In the absence of light, the terminal current is the dark current and $\Sigma_{n\text{-light}}^{<} = \Sigma_{n\text{-light}}^{>} = 0$. Since the interactions with the lattice used in the model are constant, the Landauer formula can be obtained from Eq. (6.21) to calculate the dark current as show before in chapter 5. The dark current per unit energy at a specific value of n at the contact layer at z=0 is given by

$$\begin{aligned} &i_{n0\text{-dark}}(E) = \frac{e}{h}T_n(E)\left(f_0(E) - f_d(E)\right), \\ &\text{and} \\ &T_n(E) = \mathrm{Tr}\left[\Gamma_{n0}G_n^{r}\left(\Gamma_n + \Gamma_{\text{lattice}}\right)G_n^{a}\right]. \end{aligned} \quad (6.22)$$

In Equation (6.22), f_0 and f_d are the Fermi functions corresponding to the quasi-Fermi level of the contact layer at z=0 and at the QD respectively.

In the presence of light, Eq. (6.21) can be used to calculate the total terminal current in the contact layer at z=0. The photocurrent part can be obtained from Eq. (6.21) by using the in-scattering and out-scattering function due to light interactions in the lesser and greater Green's function, and is given by

$$i_{\text{n0-photo}}(E)=\frac{e}{h}\text{Tr}\left[\left(-i\Sigma^{<}_{\text{nL}}\right)\left(iG^{r}_{\text{n}}\,\Sigma^{<}_{\text{n-light}}\,G^{a}_{\text{n}}\right)-\left(i\Sigma^{>}_{\text{nL}}\right)\left(-iG^{r}_{\text{n}}\,\Sigma^{>}_{\text{n-light}}\,G^{a}_{\text{n}}\right)\right]. \tag{6.23}$$

The photocurrent given by Eq. (6.23) is the total current minus the dark current, and the total terminal current is given by

$$i_{\text{n0}}(E)=i_{\text{n0-dark}}(E)+i_{\text{n0-photo}}(E). \tag{6.24}$$

The total terminal current flowing from the contact layer to the cylinder is obtained by the sum over all the values of the quantum number n and the integration over all energy values, and is given by

$$I_0=\int i_0(E)dE \text{ and } i_0(E)=\sum_n i_{\text{n0}}(E). \tag{6.25}$$

6.3. DETECTIVITY

The detectivity of the detector can be calculated from [47]

$$D=\frac{R_p A^{1/2}}{S_i^{1/2}}\left[\frac{\text{cm.Hz}^{1/2}}{\text{W}^{-1}}\right], \tag{6.26}$$

where R_p is the peak responsivity, S_i is the noise density spectra and A is the detector area. The noise density is related to the dark current, as shown experimentally, through the relation [49]

$$g=\frac{S_i}{4qI_{\text{dark}}}+\frac{1}{2N}, \tag{6.27}$$

where g is the photoconductive gain, and N is the number of QD layers. For a large value of N, the second term can be neglected compared to the first term and the noise density can be approximated by

$$S_i^{1/2} = \sqrt{4qI_{\text{dark}}g}\,. \tag{6.28}$$

6.4. RT-QDIP PHOTOCURRENT RESULTS

The model is applied to the RT-QDIP reported in [47, 48]. A schematic diagram of the conduction band profile of one QD layer of the RT-QDIP is shown in Fig. 6-1(a) and its description was given before in the previous chapters.

The measured responsivity of the RT-QDIP at 2 V applied bias and at different temperatures [48] is shown in Fig. 6-2. The detector has a response at 6 μm, a far-infrared response at 16 μm in addition to weak responses at 8 and 11 μm. The peak detectivity measured is 2.4×10^{10} cm.Hz$^{1/2}$ / W for the response at 6 μm at 80 K and 2 V applied bias [48]. The responsivity at 16 μm increases with temperature due to the increase of the occupation of the second excited states and disappears at low temperatures. The 300 K responsivity at 16 μm is 0.16 A/W and the detectivity is ~ 10^7 cm.Hz$^{1/2}$ / W [48].

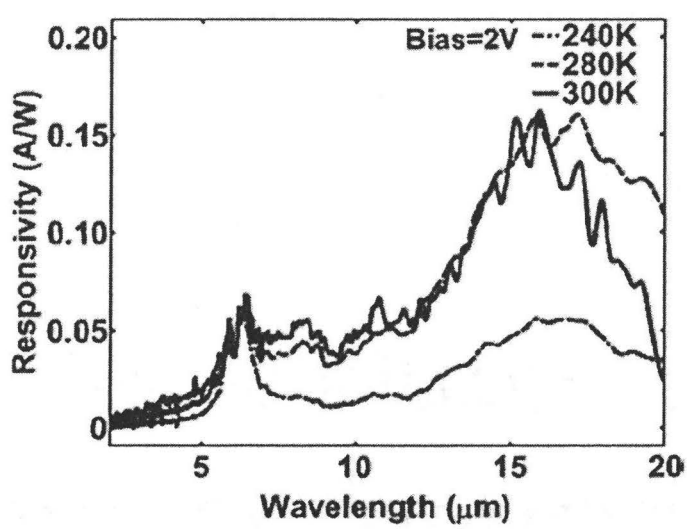

Figure 6-2 – The measured responsivity of the RT QDIP [48].

The response at 80 K as a function of bias is shown in Fig. 6-3(a) [47]. The dark current characteristics of the detector are shown in Fig. 6-3(b) [74]. The 6 μm peak increases with bias from 0.05 A/W at 2 V to 0.3 A/W at 3 V, while the corresponding dark current increase is much larger at the same temperature and applied bias. Increasing the applied bias will improve the responsivity, but will decrease the detectivity due to the bigger increase of the dark current.

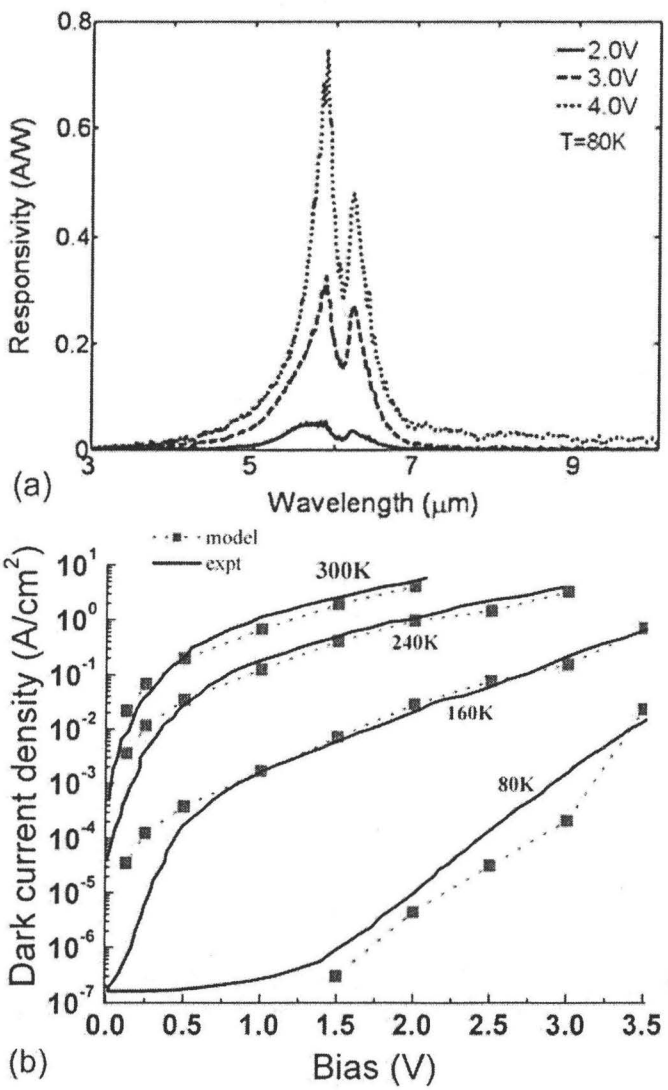

Figure 6-3 – (a) The measured responsivity of the RT-QDIP at the bias range from 2 to 4 V [47]. (b) The dark current of the RT-QDIP at various bias and temperatures by both the model [74] and measurements [47].

To interpret the responsivity curve in Fig. 6-2, the number of states per unit energy in the cylindrical volume shown in Fig. 6-1(b), is calculated and shown in Fig. 6-4. The retarded Green's function at each value of n is calculated from Eq. (6.4) using a matrix inversion, and from which the localized density of states is obtained at different values of n from Eq. (6.5). The density of states shown in Fig. 6-4 is then obtained by integrating over the space of the cylindrical volume of the localized density of states. The details of the calculations are described before in chapter 3. The QD has 3 bound states. At zero applied bias, the ground state is at E=-178 meV, relative to the CB edge of GaAs, corresponding to n=0. The first excited state is at E=-109 meV corresponding to n=1, while the second excited state is at E=-45 meV, corresponding to n=0 and 2. The transition between the three bound states and the continuum states gives the peaks appearing in the responsivity curve.

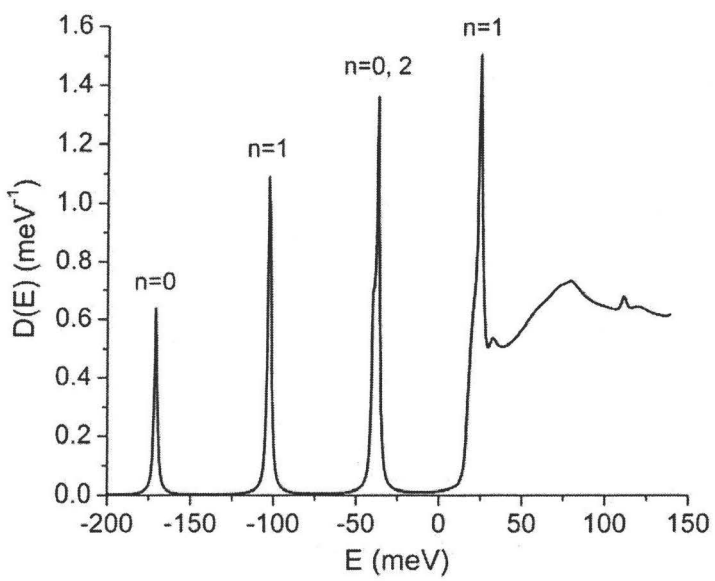

Figure 6-4 – The density of states of the RT QDIP. The bound states are from the contributions of the terms in Eq. (5) corresponding to n=0, 1, and 2. The second excited state has contributions from n=0 and n=2 as they are degenerate. The continuum states for E>0 has contributions from all terms in the series in Eq. (5).

Using the model described above, the calculated responsivity at 2 V applied bias and at three different temperatures is given in Fig. 6-5. The model gives peak responses at 6 μm and 16 μm in addition to two smaller peaks at 8 μm and 11 μm. The positions of the peaks as well as the relative amplitude of the peaks show good agreement with the experimental data in Fig. 6-2. The responsivity curve in Fig. 6-5 is obtained by the summation of all photocurrent components at different values of n due to the optical transitions between the bound states of the QD and the continuum states.

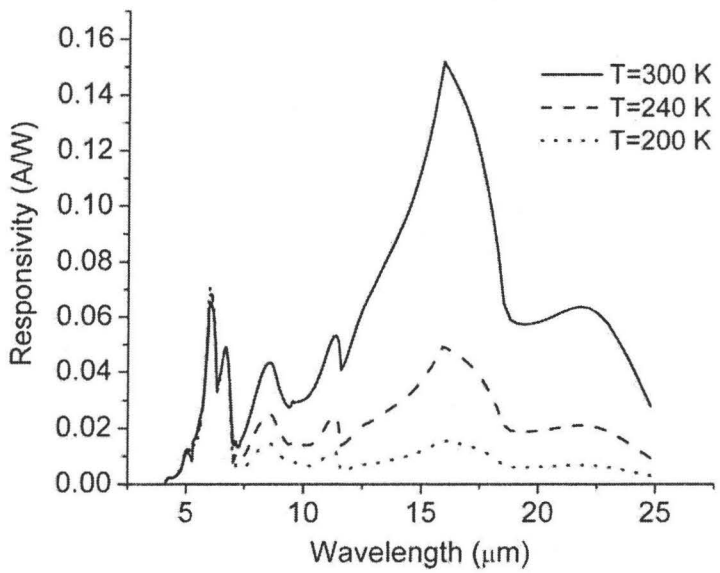

Figure 6-5 – Calculated responsivity by the model at different temperatures and 2 V applied bias.

The in-scattering functions due to the transitions from different bound states to the continuum states at 2 V and 300 K are shown in Fig. 6-6. For photon energy $\hbar\omega = \frac{hc}{\lambda}$, the transition from a bound state corresponding to n and energy E_n will be to a continuum state corresponding to $n \pm 1$ and energy E such that $\frac{hc}{\lambda} = E - E_n$. The in-scattering function $\Sigma_{01}^{<}$ from the ground state at n=0 to the continuum states at n=1 as a function of the photon wavelength is shown in Fig. 6-6(a). The mid-infrared contribution of the responsivity at the 6 μm is due to

the transition from the ground state of the QD. Figure 6-6(b) shows the in-scattering functions from the first excited state at n=1, to the continuum states corresponding to n=0 and n=2. The two transitions give the peaks in the responsivity at 8 μm and 11 μm. The far-infrared peak at 16 μm is obtained due to the transitions for the second excited state at n=0 to the continuum states at n=1 and the transitions from the second excited state at n=2 to the continuum states at n=1 and n=3 as shown in Fig. 6-6(c) and (d). The in-scattering functions $\Sigma_{01}^{<}$ and $\Sigma_{21}^{<}$ are added together since the excited states corresponding to n=0 and 2 have the same energy and the transitions from both of them to the continuum state at n=1 are correspond to the same photon energy. The in-scattering, out-scattering and total transition functions $\Sigma^{<}$, $\Sigma^{>}$ and Γ are calculated using Equations (17) and (18).

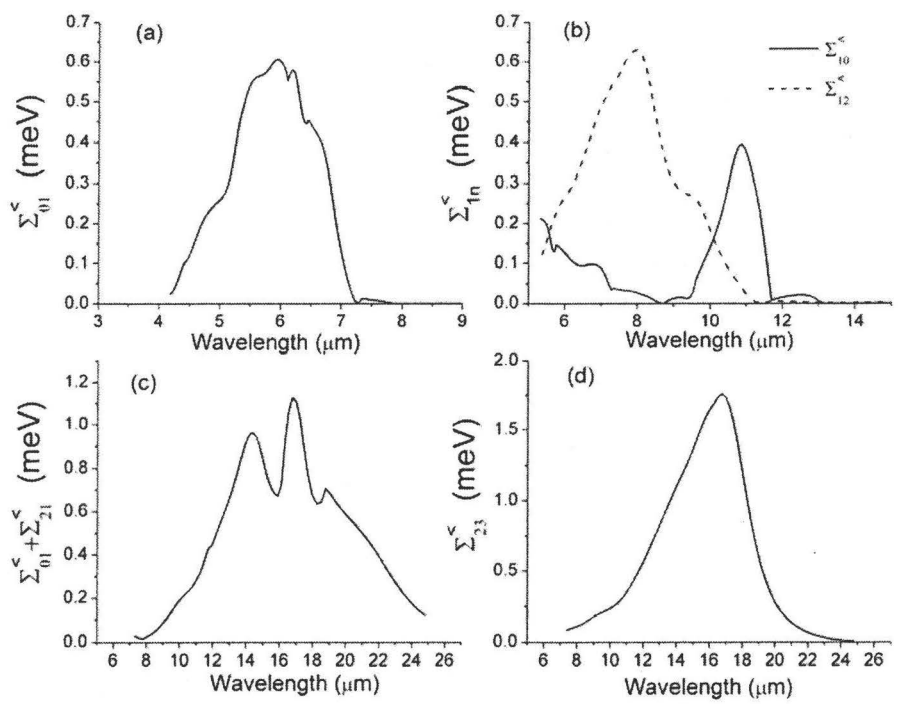

Figure 6-6 – In-scattering rate functions, as a function of the photon wavelength, due to electron transition from (a) the ground state at n=0 to the continuum at n=1, (b) the first excited state at n=1 to the continuum at n=0 and 2, (c) the excited states at n=0 and 2 to the continuum at n=1, (d) the second excited states at n=2 to the continuum at n=3.

The photocurrent components corresponding to the transition from the bound states of the QD to the continuum states at 2 V and 300 K are shown in Fig. 6-7. The photocurrent at different values of n is calculated from Eq. (6.23) and it is given as a function of the photon wavelength. The superposition of the entire photocurrent component shown in Fig. 6-7 gives the responsivity curve in Fig. 6-5.

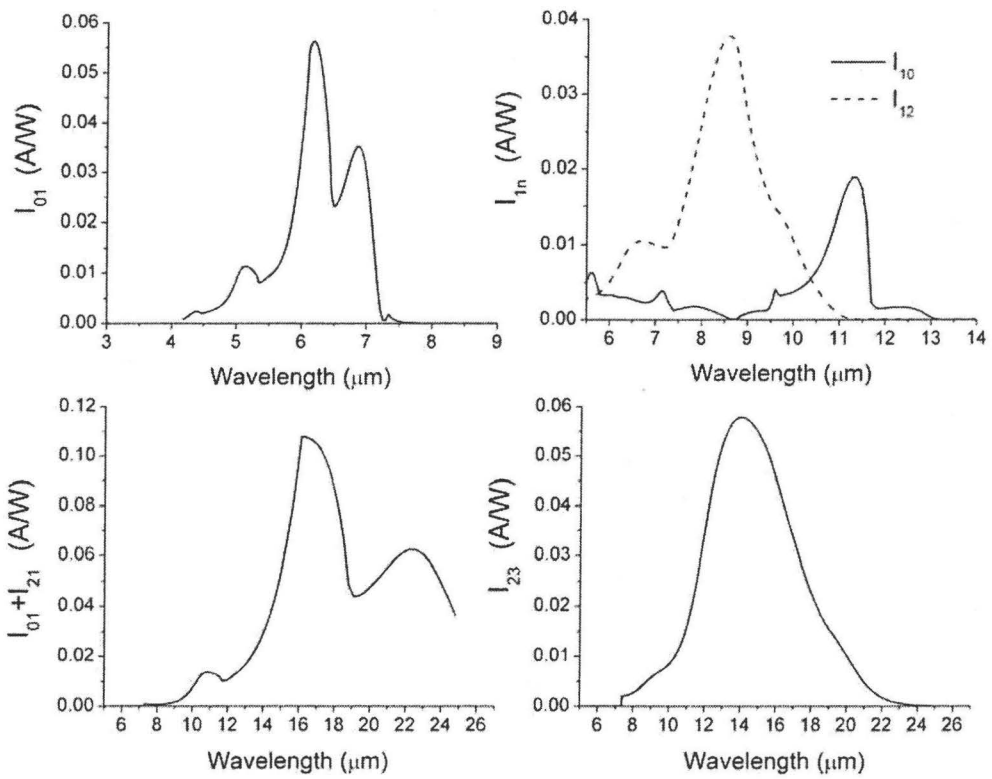

Figure 6-7 – The different photocurrent components a function of the photon wavelength, for the transitions from the bound states of the QD to the continuum states.

The mid-infrared peak at 6 μm corresponding to the transition from the ground state at n=0 to the continuum states at n=1, at 80 K and at different applied biases is shown in Fig. 6-8. The splitting of the peak is due to the overlap of the wavefunctions in the double barrier and the quantum well. The separation between the two peaks at 6 μm and 6.7 μm is ~ 21 meV which is comparable to the observed one. The increase of the responsivity with applied bias is due to the

increase of the occupation of the ground state which increases the in-scattering rate from the bound to the continuum state and the increase of the electric field that increase the transmission function.

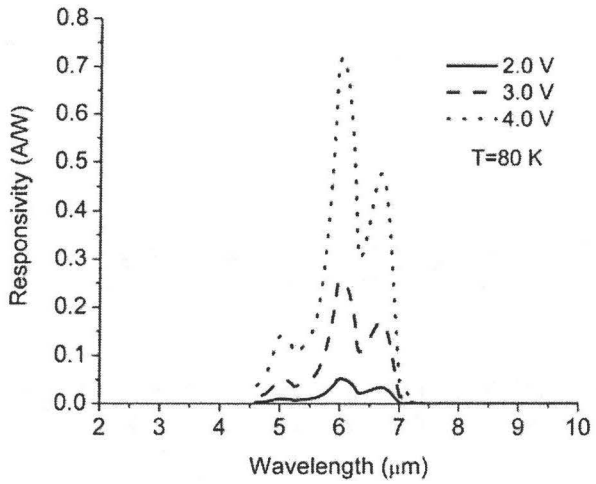

Figure 6-8 – The calculated responsivity of the RT-QDIP at the bias range from 2 to 4 V at 80 K.

The mid-infrared responsivity at 6 μm and at T=80 K as a function of applied bias is shown in Fig. 6-9. The responsivity shows an increase of almost one order of magnitude when the bias increased from 1 V to 2 V and again from 2 V to 4 V. However, the rate of increase of the dark current is much larger, as seen in Fig. 6-3, which means lower detectivity values will be obtained at large values of applied bias. So, the increase of the applied bias to increase the detector responsivity will be limited by having lower detectivity values.

The detectivity of the detector is calculated from Eq. (6.26) using the peak responsivity and the noise spectrum. The noise spectrum can be approximated by Eq. (6.28) and, obtained from the dark current characteristics and the photoconductive gain. The photoconductive gain of the detector is obtained experimentally from the measured dark current and noise spectra [49]. The photoconductive gain used in the model is approximated by the relation $g = 1 + A\exp(BV)$, where A=10^{-5} and B=4.6 V^{-1}. Figure 6-10 shows the approximate photoconductive gain used in the model and the inset shows the

measured one from the dark current and noise spectra in [47]. The gain is almost one for bias values less than 2V and increases almost exponentially for biases greater than 2 V due to avalanche effect [47].

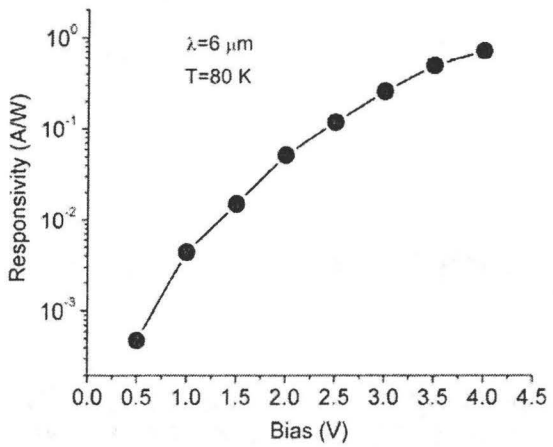

Figure 6-9 – The peak responsivity at 6 μm as a function of applied bias at 80 K.

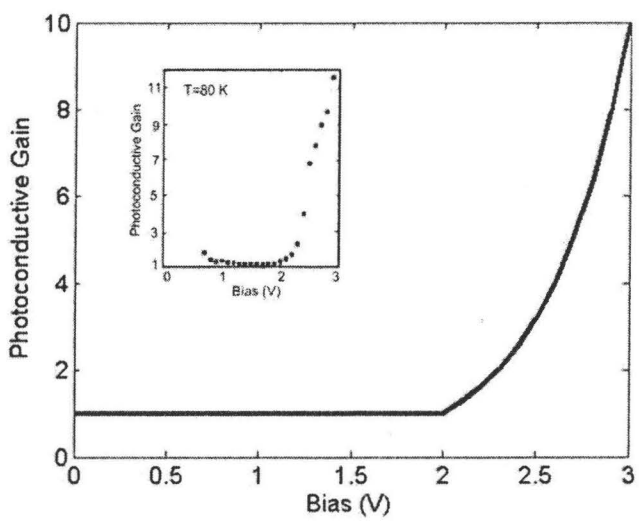

Figure 6-10 – The photoconductive gain used by the model as a function of applied bias, the inset shows the measured photoconductive gain of the 5.7 μm peak response at 80 K [47].

Using the peak responsivity values of the 6 μm peak at T=80 K, the dark current characteristics, the photoconductive gain at 80 K, and Eq. (6.26), the detectivity of the detector as a function of bias is calculated and shown in Fig. 6-11. The detectivity initially increases with bias and reaches maximum value of

3×10^{11} cm.Hz$^{1/2}$ / W at 2 V due to the increase of the responsivity with bias while the dark current values are not large. However, increasing the bias beyond 2 V will increase the dark current at a higher rate than the responsivity rate of increase. In addition the increase of the photoconductive gain, which increases the noise, will drop the detectivity of the detector as shown in Fig. 6-11. The detectivity drops to 4.15×10^{7} cm.Hz$^{1/2}$ / W at 4 V. The detectivity values calculated by the model shows agreement with the calculated detectivity in [47].

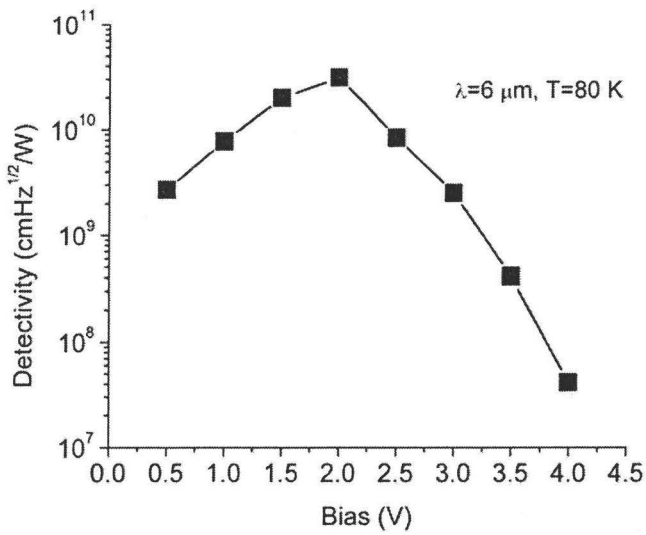

Figure 6-11– The peak detectivity by the model at 6 μm and 80 K.

The model is also used to test the effect of the doping of the QD layers and the width of the barrier between the layers, on the photocurrent, dark current and detectivity characteristics. The RT-QDIP modeled in the chapter is 10 layers and the barrier separation between the layers is 40 nm and the QDs are undoped. In the modeling, the barrier separation values used in the calculations were 30, 40, and 50 nm. The relative doping density Σ_D / Σ_{QD}, the ratio of the sheet doping density to the QD density, were 0, 0.5, 1, and 2 corresponding to 0, 0.5, 1, and 2 electrons per dot respectively. Figure 6-12 shows the peak responsivity at 6 μm and 80 K and an applied bias of 2 V as a function of relative doping density and at different barrier widths. The average electric field in the detector and occupation

of the QD bound states will be affected by the doping density and the barrier width. As discussed in chapter 5, a self-consistent solution of the charge density and the average potential energy through the device and satisfying Poisson's equation has been used to determine the quasi Fermi level and to calculate the in-scattering rates at different design parameters. The responsivity increases with the increase of the doping density and decreases with the increase of the barrier width as shown in Fig. 6-12. Increasing the relative doping density beyond that corresponding to more than 1 electron per dot produces only a small improvement in the mid-infrared responsivity since the ground state of the detector is almost fully occupied by 2 electrons per dot and the in-scattering rate does not increase.

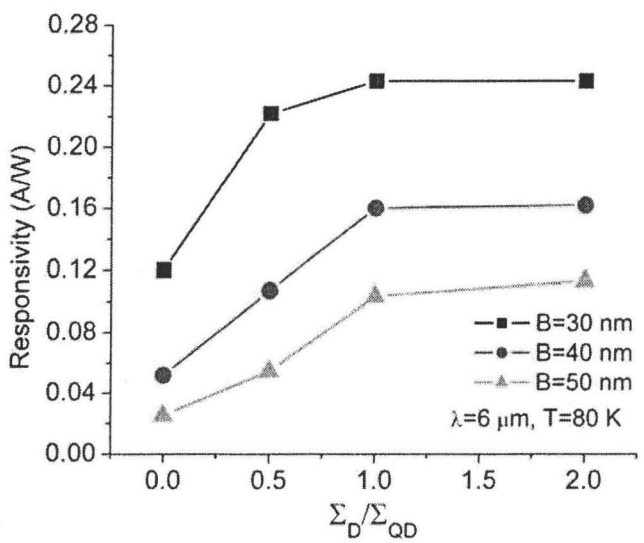

Figure 6-12– The peak responsivity at 2 V and 80 K as a function of the relative doping density and at different barrier widths.

Figure 6-13 shows the dark current values at 2 V applied bias and 80 K as a function of relative doping density and at different barrier widths. The dark current shows a monotonic increase with doping density. The value of the dark current increases almost three orders of magnitude when the relative doping density changes from 0 to 2. The increase of the barrier width from 30 nm to 50 nm decreases the dark current more than one order of magnitude.

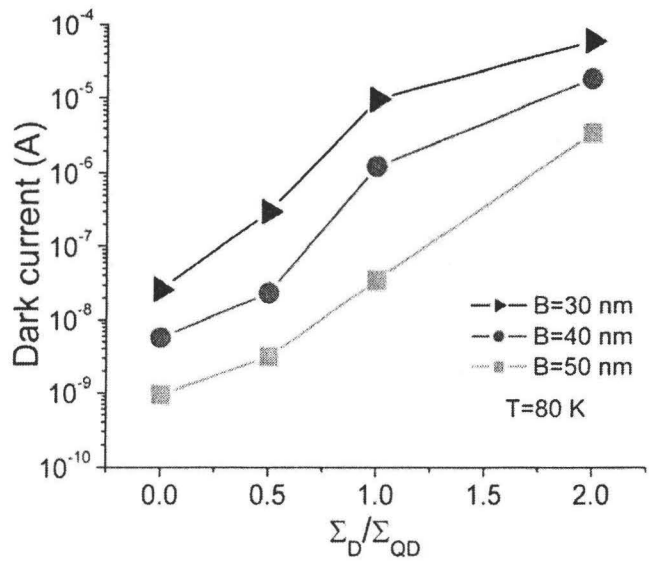

Figure 6-13– The dark current at 2 V and 80 K as a function of the relative doping density and at different barrier widths.

From the peak responsivity and dark current values shown above, the detectivity of the detector can be obtained at different doping densities and barrier widths. The mid-infrared peak detectivity at 2 V and 80 K is shown in Fig. 6-14. The increase of the doping density reduces the detectivity due to the higher rate of increase of the dark current above the photocurrent. Increasing the barrier width increases the detectivity due to the decrease in the dark current. The responsivity also decreases with the barrier width, but the decrease in the dark current is greater. The results of the Fig. 6-14 show that a larger barrier width and small doping density can give higher detectivity values, as the 0.5 relative doping and 50 nm barrier width gives higher detectivity than the undoped QDs with 40 nm barrier width. The responsivity of the detector can be improved by increasing the QD density in all layers and the number of QD layers, in order to increase the light absorption. Also, increasing both number of layers and the QD density in all layers results in a lower dark current. However, when we change the bias, the rates of increase in responsivity and dark current are different. Therefore, there is an optimum bias (see Fig. 6-11) at which the detectivity peaks, indicating the

mass approximation. The governing equation of the Green's functions is obtained in the cylindrical coordinates to be suitable for conical shaped QDs that have a cylindrical symmetry around its axis. Making use of the cylindrical symmetry and assuming local interactions allow reduction of the size of the problem to 2D instead of 3D which simplifies the numerical solution. The differential equation of the retarded Green's function in the cylindrical coordinates is discretized using the method of finite differences and the retarded Green's function matrix is obtained by a matrix inversion.

The localized DOS of the QD is obtained from the retarded Green's function and from which both the discrete energy levels and the continuum states above the QD barrier is obtained. The DOS shows all possible energy transitions which indicate the operating wavelengths of the detector. The model is used to calculate the spectral function and density of states of different QDIPs such as the QDWELL, SL-QDIP and RT-QDIP. Information of electronic states, operating wavelengths and allowed energy transitions are obtained and they are in a good agreement with experimental results.

The responsivity of QDIPs is calculated using the first-order dipole approximation and Fermi-golden rule. The bound states of the QD are obtained by solving the Hamiltonian eigenvalue problem, while the continuum states are obtained using the retarded Green's function. The responsivity results by the model are compared with the measured data and they are in good agreement with the experimental results. The model is used for optimizing the responsivity with respect to the shape and size of QDs to have an insight about the growth conditions that give best responsivity values. QDs with larger height-to-diameter ratio and small size QDs show high responsivity values.

The quantum transport equation of the NEGF is solved numerically to calculate the dark and photocurrent of the RT-QDIP. The interaction with light for photocurrent calculations has been done using the first order dipole moment and the Fermi-golden rule. A self-consistent solution of the charge density using the

density of states of the QDs and the average potential energy through the device and satisfying Poisson's equation has been done to obtain the quasi Fermi level and the average potential energy through the device. The model results for the dark and photocurrent are in good agreement with the experimental results. The model has been used for theoretical predictions of the dark and photocurrent characteristics at other design parameters. The effect of using different design parameters such as the number of QD layers, the barrier separation between the layers and the doping density on the dark and photocurrent has been obtained.

The detectivity of the RT-QDIP has been calculated at different design parameters. The results shows a trade off between the responsivity and detectivity and what determines the best performance is how much the rate of increase of the photocurrent and dark current is affected by the different design parameters.

The models developed in the thesis show good matching with experimental results. The models can be used as a tool of characterization of different QDIP structures to get the operating wavelengths, the relative strength of the responsivity peaks, the dark and photocurrent characteristics and the detector detectivity at different design parameters. This allows the best design for final device fabrication to be found saving money and time. In addition it is possible to establish the characteristics of new structures to ensure that they will meet the required specifications before their actual growth and processing. So, the outcomes of this research will allow for efficient device design with optimized performance with respect to operating wavelength, responsivity, detectivity, etc.

7.2. FUTURE WORK

The present research lays the foundation for developing quantum transport models based on NEGF to describe the main characteristics of QDIPs. The goal of these models is to understand the physical operations of these nano-devices in order to have an insight of how the detector design can be improved such that it gives the optimized performance efficiently fulfilling the required characteristics.

There is a trade off between the accuracy of the model and its complexity. Therefore, for good results a compromise between the accuracy and complexity is necessary. More research is required to improve and upgrade the models developed in the thesis to make them more accurate and to calculate more physical quantities required in fully characterizing the QDIPs. Some of these recommendations will be described in this section

7.2.1. INTERMIXING AND STRAIN EFFECT

The models developed in the thesis are based on a single band effective mass approximation. The QDIPs modeled are unipolar devices and the values of the conduction band offsets and electron effective masses are used to solve the differential equation of the Green's function. As described in chapter 3, all points in the lattice grid associated to the QD have single values for the potential energy and electron effective mass and the same thing for the QW and barrier regions. This means that no intermixing is assumed between the QD material and the material corresponding to the surrounding barriers. For example, for InAs QDs grown on GaAs, the model assumed no intermixing between In and Ga to get a simplified potential energy and effective mass profiles. The real situation is that intermixing between different heterostructure materials [116, 117, 118] does occur which will modify the values of the band offsets and effective masses [125]. Also the strain field distribution in the QD region will affect the values of band offsets and effective masses such that they will have a specific distribution in the QD and the surrounding regions. The numerical model developed in the thesis is general and can accept any input potential energy and effective masses profile if known. So finding out the exact compositions of the QD and the surrounding barrier in addition to the effect of the strain field distribution on the values of the conduction band offsets and effective masses will allow the model to describe a more realistic configuration of the QD region and hence giving better results.

7.2.2. NON-UNIFORMITY OF QDS SIZE, AND DISTRIBUTION

One of the assumptions used in the model to simplify the calculations is that it actually describes a uniform distribution of QDs in the layers of the detector in addition to using the average values of height and diameter of QDs in the calculations. This gives symmetry that allows, for example, calculating the portion of the current that passes through one QD and then the total current is the QD density times this portion of the current. In addition it simplifies the calculations of the DOS, energy eigenvalues and the corresponding wavefunctions. The model used in the thesis considered the uncertainty in the shape and size of QDs by using average values for the height and diameter of the QDs by adding a small imaginary part to the electron energy in the equation. Adding this small imaginary part causes broadening to the energy levels such that they have a Gaussian shape instead of sharp delta functions obtained when all QDs have the same shape and size. A better description of the random shape and size of QDs can be done through a sensitivity analysis technique described in [119, 120, 121]. This technique gives an estimate about the rate of change of a specific physical quantity as a function of one of the dimensional parameters, for example. In this way there is no need of multiple simulations to scan all possible values of heights and diameters of QDs and instead, the average values can be used one time in the simulation and then the sensitivity analysis will give the corresponding simulation values at other values of QD sizes. So including this technique may save time of repeating the simulations in case other QDs need to be tested.

7.2.3. INTERACTION WITH THE LATTICE

The NEGF model gives a straightforward way of including interactions in the system whether with the surrounding contacts or internally in the QDs and the surrounding barriers. The types of interactions to be included and the degree of approximations to be used determine both the accuracy and the complexity of the

calculations. The interactions with the lattice are modeled in its simplest form. The self-energy due to lattice interactions is assumed to be constant independent on energy and position and corresponding to localized elastic scattering of a constant scattering rate. This simple form of self-energy does not require a self-consistent solutions between the Green's functions and the self-energy as in the case of considering the self-consistent first order Born approximation for modeling electron phonon interactions. A realistic description of the interaction with the lattice requires including self-energies corresponding to interactions between electrons and longitudinal and acoustic phonons, but a self-consistent solution is needed in this case. Assuming constant and uniform scattering rates simplifies the calculations but it might not be valid for high applied biases and high temperature. The electron-electron interaction is considered qualitatively in the model through a self-consistent solution between the electron density and the potential energy as shown in chapter 5. A better description of electron-electron interaction can be done through the Hartree-Fock approximation to calculate the self-energy due to the charges of the QD and surrounding QDs.

7.2.4. TEMPERATURE EFFECT ON RESPONSIVITY

One important aspect that should have further interest and focus in future research is the effect of temperature on the responsivity of the detector [122- 124]. In chapter 6, the photocurrent model uses a simplified version of the interaction with the lattice that does not include inelastic scattering and the energy transitions are only due to interaction with light. Therefore the total decay rate of a state is independent of temperature while the in-scattering and out-scattering transition rates are a function of temperature through a quasi-Fermi function. This assumption does not show a decrease of the responsivity with temperature for the mid-infrared as expected, while the far-infrared peak is increased and not decreased due to the increase of the occupation of the higher excited states with temperature as shown in Fig. 6-5. Further research on interactions with the lattice

and the temperature effect on the responsivity is recommended to give better solution the problem.

7.2.5. TRANSIENT RESPONSE

Furthermore, there is one important characteristic of QDIP that has not been discussed in this work which might be useful for some applications. The transient response of the QDIP should be modeled for fluorescent applications where the time decay of the received pulse is important. The models in the thesis focus on DC applications such as thermal imaging and focal plane arrays where the signal is in steady state. For time varying signal, the transient response for the responsivity is needed. Some techniques to model the transient response in QWIPs have been shown in [126-128] using Monte Carlo methods. For an accurate description of the transient response in a quantum system like a QDIP, the real time Green's functions can be used to calculate the responsivity as a function of time [129]. Further research is needed to solve the problem without adding a lot of complexity due to the increase of the dimensions of the problem by adding an extra time axis. One simple way would be to obtain a circuit model for the QDIP in order to estimate a time constant RC for the detector. The time constant could be obtained by calculating the resistance of the barrier material between the QD layers and the equivalent capacitance between the contacts of the detector taking into consideration the QD capacitance in the layers.

APPENDIX A

The Hamiltonian in cylindrical coordinates assuming that the potential energy has azimuthal symmetry and does not depend on the rotation angle θ is given by

$$H = -\frac{\hbar^2}{2}\left(\frac{1}{r}\frac{\partial}{\partial r}\frac{r}{m^r(r,z)}\frac{\partial}{\partial r} + \frac{1}{m^r(r,z)}\frac{1}{r^2}\frac{\partial^2}{\partial\theta^2} + \frac{\partial}{\partial z}\frac{1}{m^z(r,z)}\frac{\partial}{\partial z}\right) + V(r,z) \qquad \text{(A.1)}$$

Assuming that the eigenfunctions of the Hamiltonian have the form

$$\Psi_n(r,\theta,z) = e^{in\theta}\psi_n(r,z) \qquad \text{(A.2)}$$

Therefore

$$H\Psi_n = E_n\Psi_n \qquad \text{(A.3)}$$

Substituting (A.2) into (A.3) and making use of $\frac{\partial^2\Psi_n}{\partial\theta^2} = -n^2\Psi_n$, the angular part dependence can be removed and we end up with

$$H_n\psi_n = E_n\psi_n \qquad \text{(A.4)}$$

and

$$H_n = -\frac{\hbar^2}{2}\left(\frac{1}{r}\frac{\partial}{\partial r}\frac{r}{m^r(r,z)}\frac{\partial}{\partial r} + \frac{-n^2}{m^r(r,z)}\frac{1}{r^2} + \frac{\partial}{\partial z}\frac{1}{m^z(r,z)}\frac{\partial}{\partial z}\right) + V(r,z) \qquad \text{(A.5)}$$

The differential operator in (A.5) can be discretized according to the grid representation shown in Fig. A1 as follows:

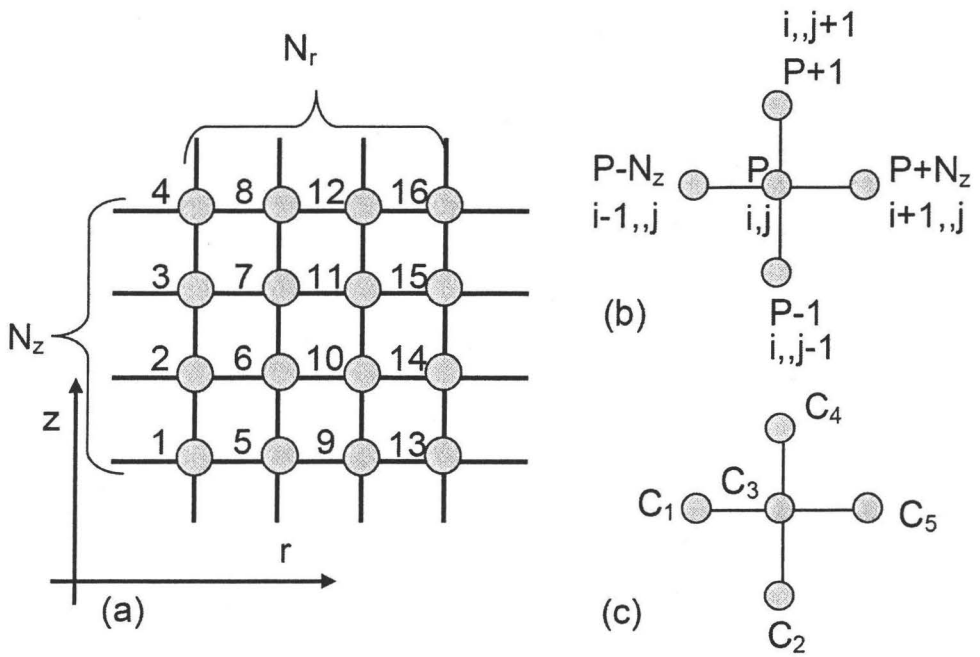

Figure A 1 – (a) Schematic of a 16 points grid used to discretize the Hamiltonian operator. (b) A lattice point and the 4 surrounding points showing the relation between the number of the point in the lattice and the corresponding indices in the radial part i=1 to 4 and the z part j=1 to 4. (c) Schematic shows that each lattice point has 5 places of non-zero values in the Hamiltonian matrix.

The radial differential part is given by

$$\left[\left(\frac{1}{r}\frac{\partial}{\partial r}\frac{r}{m^r(r,z)}\frac{\partial}{\partial r}\right)\psi\right]_{ij} = \frac{1}{ar_{ij}}\left[\left(\frac{r}{m^r}\frac{\partial}{\partial r}\right)_{i+1/2,j} - \left(\frac{r}{m^r}\frac{\partial}{\partial r}\right)_{i-1/2,j}\right]\psi_n$$

$$= \frac{1}{a^2 r_{ij}}\begin{bmatrix} \frac{r_{i+1/2,j}}{m^r{}_{i+1/2,j}}\left(\psi_{i+1,j}-\psi_{i,j}\right) \\ -\frac{r_{i-1/2,j}}{m^r{}_{i-1/2,j}}\left(\psi_{i,j}-\psi_{i-1,j}\right) \end{bmatrix} \qquad (A.6)$$

$$= \frac{1}{a^2 r_{ij}}\begin{bmatrix} \frac{\left(r_{i+1,j}+r_{i,j}\right)/2}{\left(m^r{}_{i+1,j}+m^r{}_{i,j}\right)/2}\left(\psi_{i+1,j}-\psi_{i,j}\right) \\ -\frac{\left(r_{i,j}+r_{i-1,j}\right)/2}{\left(m^r{}_{i,j}+m^r{}_{i-1,j}\right)/2}\left(\psi_{i,j}-\psi_{i-1,j}\right) \end{bmatrix}$$

and

$$\left[\left(\frac{-n^2}{m^r(r,z)r^2}\right)\psi\right]_{ij} = \left(\frac{-n^2}{a^2 m^r{}_{ij} r_{ij}{}^2}\right)\psi_{ij} \tag{A.7}$$

The z differential part is given by

$$\begin{aligned}\left[\left(\frac{\partial}{\partial z}\frac{1}{m^z(r,z)}\frac{\partial}{\partial z}\right)\psi\right]_{ij} &= \frac{1}{a}\left[\frac{1}{m^z{}_{i,j+1/2}}\left(\frac{\partial}{\partial z}\psi\right)_{i,j+1/2} - \frac{1}{m^z{}_{i,j-1/2}}\left(\frac{\partial}{\partial z}\psi\right)_{i,j-1/2}\right] \\ &= \frac{1}{a^2}\begin{bmatrix}\dfrac{2}{m^z{}_{i,j+1}+m^z{}_{i,j}}\left(\psi_{i,j+1}-\psi_{i,j}\right) \\ -\dfrac{2}{m^z{}_{i,j}+m^z{}_{i,j-1}}\left(\psi_{i,j}-\psi_{i,j-1}\right)\end{bmatrix}\end{aligned} \tag{A.8}$$

and the potential energy part is given by

$$\left[V(r,z)\psi\right]_{ij} = V_{ij}\psi_{ij} \tag{A.9}$$

By combining the equations A.6 to A.9, the Hamiltonian differential equation in A.4 is given in a matrix form as

$$\left[H_n\psi\right]_{ij} = -t\left[c_1\psi_{i-1,j} + c_2\psi_{i,j-1} + c_3\psi_{i,j} + c_4\psi_{i,j+1} + c_5\psi_{i+1,j}\right] \tag{A.10}$$

where $t = \dfrac{\hbar^2}{2m_o a^2}$ and m_o is the free electron mass while m^r and m^z are the electron effective masses in the materials in the radial and z directions and

$$
\begin{aligned}
c_1(P) &= \frac{r_{i,j} + r_{i-1,j}}{m^r{}_{i,j} + m^r{}_{i-1,j}} = \frac{r_P + r_{P-N_z}}{m^r{}_P + m^r{}_{P-N_z}}, \\
c_2(P) &= \frac{2}{m^z{}_{i,j} + m^z{}_{i,j-1}} = \frac{2}{m^z{}_P + m^z{}_{P-1}}, \\
c_4(P) &= \frac{2}{m^z{}_{i,j} + m^z{}_{i,j+1}} = \frac{2}{m^z{}_P + m^z{}_{P+1}}, \\
c_5(P) &= \frac{r_{i,j} + r_{i+1,j}}{m^r{}_{i,j} + m^r{}_{i+1,j}} = \frac{r_P + r_{P+N_z}}{m^r{}_P + m^r{}_{P+N_z}}, \text{ and} \\
c_3(P) &= -\frac{V_{i,j}}{t} - \left[c_1(P) + c_2(P) + c_4(P) + c_5(P) + \frac{n^2}{m^r{}_{i,j} r_{i,j}{}^2} \right] \\
&= -\frac{V_P}{t} - \left[c_1(P) + c_2(P) + c_4(P) + c_5(P) + \frac{n^2}{m^r{}_P r_P{}^2} \right]
\end{aligned}
\tag{A.11}
$$

The Hamiltonian matrix elements for a grid of $N_z \times N_r$ points are given by

$$
\begin{aligned}
&H_n(P,P) = c_3(P), \\
&H_n(P,P-N_z) = H_n(P-N_z,P) = c_1(P), \\
&H_n(P,P+N_z) = H_n(P+N_z,P) = c_5(P), \\
&H_n(P,P-1) = H_n(P-1,P) = c_2(P), \text{ and} \\
&H_n(P,P+1) = H_n(P+1,P) = c_4(P)
\end{aligned}
\tag{A.12}
$$

where P is from 1 to $N_z \times N_r$. The rest of the elements of the matrix are zero. The boundary conditions should be specified at the elements corresponding to i=1 and i=N_r and j=1 and j=N_z. For zero B.C at j=1 corresponding to the points 1, 5, 9, 13 and j=N_z corresponding to the points 4, 8, 12, 16, the Hamiltonian matrix elements are given by

$$
\begin{aligned}
&H_n(P,P-1) = H_n(P-1,P) = 0 \text{ for } j = 1 \\
&H_n(P,P+1) = H_n(P+1,P) = 0 \text{ for } j = N_z
\end{aligned}
\tag{A.13}
$$

For zero B.C at $i = N_r$ corresponding to the elements 13, 14, 15, 16, the Hamiltonian matrix elements are given by

$$
H_n(P,P+N_z) = H_n(P+N_z,P) = 0 \text{ for } i = N_r \tag{A.14}
$$

Around the cylinder axis at i=1 corresponding to the points 1, 2, 3, 4, the zero derivative B.C should be applied. The wavefunction value should be the same around the axis and so $\psi_n(1) = \psi_n(0)$. By using this B.C in A.10, the Hamiltonian matrix elements will be given by A.12 except that

$$H_n(P,P) = c_3(P) = -\frac{V_P}{t} - \left[c_2(P) + c_4(P) + c_5(P) + \frac{n^2}{m^r{}_P r_P{}^2} \right] \qquad \text{(A.12)}$$

For the corner points such as 1, 4, 13, 16, they have two B.C corresponding to both the radial and z parts and both of the two conditions will be applied to the Hamiltonian matrix elements as shown above. After obtaining the Hamiltonian matrix including the B.C, the eigenvalue problem can be solved to get the energy eigenvalues and the corresponding eigenstates. For the continuum part of the spectrum, a proper self energy function should be added at the cylinder boundaries to simulate the proper open B.C. After obtaining the Hamiltonian matrix and the self-energy due coupling with the surrounding or due internal interactions, the Green's function of the system can be calculated and from which the electronic and transport properties can be obtained as showed in the thesis.

APPENDIX B

The retarded Green's function in the lead satisfying the equation

$$[E-H_n]G_n^r=\frac{1}{r}\delta(r-r')\delta(z-z') \tag{B.1}$$

can be written as

$$G_n^r=\sum_m \chi_m(z)\chi_m^*(z')f_{nm}(r,r') \tag{B.2}$$

where $\chi_m(z)$ satisfies the eigenvalue problem

$$\left[-\frac{\hbar^2}{2m}\frac{d^2}{dz^2}+V(z)\right]\chi_m(z)=\varepsilon_m\chi_m(z) \tag{B.3}$$

and

$$\sum_m \chi_m(z)\chi_m^*(z')=\delta(z-z') \tag{B.4}$$

Substituting B.2 into B.1 and using B.3 and B.4 we end up with

$$(E-\varepsilon_m)f_{nm}+\frac{\hbar^2}{2m}\left(\frac{1}{r}\frac{\partial}{\partial r}r\frac{\partial}{\partial r}-\frac{n^2}{r^2}\right)f_{nm}=\frac{1}{r}\delta(r-r') \tag{B.5}$$

This can be written as

$$\left(\frac{1}{r}\frac{\partial}{\partial r}r\frac{\partial}{\partial r}\right)f_{nm}+\left(k_m^2-\frac{n^2}{r^2}\right)f_{nm}=\frac{1}{r}\delta(r-r')\times\frac{2m}{\hbar^2} \tag{B.6}$$

Which is Bessel differential equation with a delta function source term in the R.H.S and $k_m^2=\dfrac{2m(E-\varepsilon_m)}{\hbar^2}$. For $R\le r<r'$, which is a point outside the cylinder which has a radius of R and lies in the surrounding lead, the solution to B.6 is given by

$$f_{nm}=C_1J_n(k_mr)+C_2Y_n(k_mr) \tag{B.7}$$

For $r>r'$, the solution should be finite at infinity, so it is given by the Henkel function of the first kind

$$f_{nm} = C_3 H_n^{(1)}(k_m r) \tag{B.8}$$

The first solution should give zero B.C at $r = R$ and therefore

$$\begin{aligned} &f_{nm} = C_1 J_n(k_m R) + C_2 Y_n(k_m R) = 0 \Rightarrow C_2 = -C_1 \frac{J_n(k_m R)}{Y_n(k_m R)} \text{ and} \\ &f_{nm} = C_1 \left[J_n(k_m r) - Y_n(k_m r) \frac{J_n(k_m R)}{Y_n(k_m R)} \right] \end{aligned} \tag{B.9}$$

The two solutions should be equal at $r = r'$ and therefore the solution can be written in the form

$$f_{nm} = C \left[J_n(k_m r^<) - Y_n(k_m r^<) \frac{J_n(k_m R)}{Y_n(k_m R)} \right] H_n^{(1)}(k_m r^>) \tag{B.10}$$

where $r^<$ and $r^>$ are the smaller and greater of r and r'. By integrating B.6 around $r = r'$, the solution should satisfy the equation

$$\left. \frac{\partial f_{nm}}{\partial r} \right|_{r=r'+\varepsilon} - \left. \frac{\partial f_{nm}}{\partial r} \right|_{r=r'-\varepsilon} = \frac{1}{r'} \times \frac{2m}{\hbar^2} \tag{B.11}$$

Substituting B.10 into B.11, we get

$$C \begin{bmatrix} H_n'^{(1)}(k_m r') \left(J_n(k_m r') - Y_n(k_m r') \dfrac{J_n(k_m R)}{Y_n(k_m R)} \right) \\ -H_n^{(1)}(k_m r') \left(J_n'(k_m r') - Y_n'(k_m r') \dfrac{J_n'(k_m R)}{Y_n(k_m R)} \right) \end{bmatrix} = \frac{1}{r'} \times \frac{2m}{\hbar^2} \tag{B.12}$$

Solving B.12 will give the value of the constant C. To solve B.12, the asymptotic behavior for large value of $r \to \infty$ of the Bessel and Henkel functions will be used to do the derivative and the required substitution in B.12. The asymptotic value of the Bessel function at very large r are given by

$$J_n(x) \to \sqrt{\frac{2}{\pi x}}\cos\left(x-\frac{n\pi}{2}-\frac{\pi}{4}\right),\ x \gg 1$$
$$Y_n(x) \to \sqrt{\frac{2}{\pi x}}\sin\left(x-\frac{n\pi}{2}-\frac{\pi}{4}\right),\ x \gg 1 \qquad \text{(B.13)}$$
$$H_n^{(1)}(x) \to \sqrt{\frac{2}{\pi x}}\exp\left[i\left(x-\frac{n\pi}{2}-\frac{\pi}{4}\right)\right],\ x \gg 1$$

Substituting B.13 into B.12, the constant C can be obtained and it is given by

$$C=\left(\frac{\pi}{2}\frac{Y_n(k_mR)}{J_n(k_mR)+iY_n(k_mR)}\right)\times\frac{2m}{\hbar^2}=\left(\frac{\pi}{2}\frac{Y_n(k_mR)}{H_n^{(1)}(k_mR)}\right)\times\frac{2m}{\hbar^2} \qquad \text{(B.14)}$$

So the radial part of the Green's function can be written as

$$f_{mm}(r,r')=\left(\frac{\pi}{2}\frac{Y_n(k_mR)}{H_n^{(1)}(k_mR)}\right)\times\frac{2m}{\hbar^2}\left[J_n(k_mr^<)-Y_n(k_mr^<)\frac{J_n(k_mR)}{Y_n(k_mR)}\right]H_n^{(1)}(k_mr^>) \qquad \text{(B.15)}$$

and $r^<$ and $r^>$ are the smaller and greater of r and r'. Specifically the radial part calculated at $r=r'=R+a$, which is one lattice constant inside the lead and outside the cylinder is given by

$$f_{mm}(r=r'=R+a)=\frac{\pi}{2}\frac{2m}{\hbar^2}\begin{bmatrix}J_n\left(k_m\left(R+a\right)\right)Y_n\left(k_mR\right)\\-J_n\left(k_mR\right)Y_n\left(k_m\left(R+a\right)\right)\end{bmatrix}\frac{H_n^{(1)}\left(k_m\left(R+a\right)\right)}{H_n^{(1)}\left(k_mR\right)} \qquad \text{(B.16)}$$

and the Green's function is then given by

$$G_n^r=\sum_m \chi_m(z)\chi_m^*(z')\frac{\pi}{2}\frac{2m}{\hbar^2}\begin{bmatrix}J_n\left(k_m\left(R+a\right)\right)Y_n\left(k_mR\right)\\-J_n\left(k_mR\right)Y_n\left(k_m\left(R+a\right)\right)\end{bmatrix}\frac{H_n^{(1)}\left(k_m\left(R+a\right)\right)}{H_n^{(1)}\left(k_mR\right)} \qquad \text{(B.17)}$$

The previous derivation is obtained for propagating modes for $E>\varepsilon_m$. The same procedure can be used to obtain the Green's function for evanescent modes where $E \le \varepsilon_m$. And in this case, the modified Bessel functions I and K will be used and the same procedure will be applied. So the Green's function for all energy values is given by

$$G_n^r = \begin{cases} \sum_m \chi_m(z)\chi_m^*(z')\frac{\pi}{2}\frac{2m}{\hbar^2}\begin{bmatrix} J_n\left(k_m(R+a)\right)Y_n(k_mR) \\ -J_n(k_mR)Y_n\left(k_m(R+a)\right)\end{bmatrix} \\ \qquad \times \frac{H_n^{(1)}\left(k_m(R+a)\right)}{H_n^{(1)}(k_mR)}, \quad E > \varepsilon_m \\ \sum_m \chi_m(z)\chi_m^*(z')\frac{\pi}{2}\frac{2m}{\hbar^2}\begin{bmatrix} K_n\left(k_m(R+a)\right)I_n(k_mR) \\ -K_n(k_mR)I_n\left(k_m(R+a)\right)\end{bmatrix} \\ \qquad \times \frac{K_n\left(k_m(R+a)\right)}{K_n(k_mR)}, \quad E \le \varepsilon_m \end{cases} \tag{B.18}$$

REFERENCES

1. A. Rogalski, "Infrared detectors: status and trends," *Progress in Quantum Electronics*, **27**, pp.59-210, (2003).
2. J. Piotrowski and A. Rogalski, "Uncooled long wavelength infrared photon detectors," *Infrared Physics & Technology*, **46**, pp.115–131, (2004).
3. A. Rogalski, K. Adamiec, J. Rutkowski, *Narrow-Gap Semiconductor Photodiodes*, SPIE Press, Washington (2000).
4. B. F. Levine, "Quantum-well infrared photodetectors," *J. Appl. Phys.*, **74**, pp.R1-R81, (1993).
5. J. L. Pan, C. G. Fonstad Jr., "Theory, fabrication and characterization of quantum well infrared photodetectors," *Mater. Sci. Eng.*, **28**, pp.65-147, (2000).
6. A. Rogalski, "Assessment of HgCdTe photodiodes and quantum well infrared photoconductors for long wavelength focal plane arrays," *Infra. Phys. Technol.*, **40**, pp. 279-294, (1999).
7. M. O. Manasreh , Semiconductor quantum wells and superlattices for long-wavelength infrared detectors, (artech House, Norwood,, 1993)
8. F. F. Sizov, and A. Rogalski, Infrared photon detectors, (SPIE Optical Engineering Press, Bellingham, 1995)
9. S. D.Gunapala and K. M. S. V. Bandara, Recent development in quantum-well infrared photodetectors," *Thin films*, Academic Press, New yor*k*, Vol. **21**, pp. 113-237, (1995)
10. L. J. Kozlowski, G. M. W illiams, G. J. Sullivan, C. W. Farley, R. J. Anderson, J. Chen, D. T.Cheung, W. E. Tennant and R. E. DeWames, " LWIR 128×128 GaAs/AlGaAs multiple quantum well hybrid focal plane array" *IEEE Trans. Electron devices*, **38,** pp. 1124-1130, May (1991).
11. B. F. Levine, C. G. Bethea, K. G. Glogovsky, J. W. Stay and R. E. Leibenguth, "Long-wavelength 128*128 GaAs quantum well infrared photodetector arrays", *Semicond. Sci. Technol.* **6**, pp. C114-C119, Dec. (1991).
12. G. C.. Bethea, B. F. Levine, M. T. Asom, R. E. Leibenguth, J. W. Stayt, K. G. Glogovsky, R. A. Morgan, J. D. Blackwell and W. J. Parrish, " Long wavelength infrared 128×128 Al_xGa_{1-x} As/GaAs quantum well infrared camera and imaging system" *IEEE Trans. Electron devices*, **40**, pp. 1957-1963 (1993).
13. W. A. Beck, J. W. Little, A. C. Goldberg and T. S. Faska, in: H. C. Liu, B. F.Levine, J. Y. Anderson (Eds), *Quantum Well Intersubband Transition Physics and Devices*, (Kluwer Academic Publishers, Dordrecht, 1994).
14. L.J. Kozolwski, in:H. C. Liu, B. F. Levine, J. Y. Anderson , Quantum well Intersubband Transition Physics and Devices, (Kluwer Academic Publishers, Dordrecht, pp. 43, 1994).

15. A. Rogalski, "Comparison of the performance of quantum well and conventional bulk infrared photodetectors," *Infra. Phys. Technol.*, **38**, pp. 295-310 (1997).

16. J. Phillips, "Evaluation of the fundamental properties of quantum dot infrared detectors," *J. Appl. Phys.*, **91**, pp. 4590-4594, Apr. (2002).

17. Y. G. Sidorov, S. A. Dvoretsky, M. V. Yakushev, N. N. Mikhailov, V. S. Varavin and V. I. Liberman, "Peculiarities of the MBE growth physics and technology of narrow-gap II–VI compounds," *Thin Solid Films*, **306**, pp. 253-265 (1997)

18. S. Krishna, A. D. Stiff-Roberts, J. D. Phillips, P. Bhattacharya and S. W. Kennerly, "Hot dot detectors," *IEEE Circuits and Devices Magazine*, **18**, pp. 14-24, Jan.(2002).

19. J. Phillips, ""Evaluation of the fundamental properties of quantum dot infrared detectors," *J. Appl. Phys.*, **91**, pp. 4590–4594, (2002).

20. B. Kochman, A. D. Stiff-Roberts, S. Chakrabarti, J. D. Phillips, S. Krishna, J. Singh and P. Bhattacharya, "Absorption, carrier lifetime, and gain in InAs–GaAs quantum-dot infrared photodetectors," *IEEE J. Quant. Elec.*, **39**, pp. 459-467, Mar. (2003).

21. V. Ryzhii, I. Khmyroval, M. Ryzhii, V. Mitin, "Comparison of dark current, responsivity and detectivity in different intersubband infrared photodetectors," *Semicond. Sci. Technol.*, **19**, pp. 8-16, (2004).

22. E. Finkman , S. Maimon, V. Immer, G. Bahir, S. E. Schacham, F. Fossard, F. H. Julien, J. Brault and M. Gendry," Polarized front-illumination response in intraband quantum dot infrared photodetectors at 77 K," *Phys. Rev.* B **63**, 045323 (7 pages) (2001), and references therein.

23. S. Krishna, S. D. Gunapala, S. V. Bandara, C. Hill and D. z. Ting, "Quantum dot based Infrared focal plane arrays," *Proceedings of the IEEE*, **95**, pp. 1838-1852, Sep (2009).

24. S. Chakrabarti, A.D. Stiff-Roberts, X. H. Su, P. Bhattacharya, G. Ariyawansa and A. G. U. Perera, "High-performance mid-infrared quantum dot infrared photodetectors," *J. Phys. D: Appl. Phys.*, **38,** pp. 2135-2141 (2005).

25. A. D. Stiff, X. H. Su, S. Chakrabarti and P. Bhattacharya, "Contribution of field-assisted tunneling emission to dark current in InAs-GaAs quantum dot infrared photodetectors," *IEEE Photonics Technol. Lett*,. **16**, pp. 867-869, (2004).

26. D. L. Huffaker, G. Park, Z. Zou, O. B. Shchekin, and D. G. Deppe," 1.3 μm room-temperature GaAs-based quantum-dot laser," *Appl. Phys. Lett.* **73**, pp. 2564-2566 (1998).

27. L. F. Lester, A. Stintz, H. Li, T. C. Newell, E. A. Pease, B. A. Fuchs, and K. J. Malloy, "Optical characteristics of 1.24-μm InAs quantum-dot laser diodes," *IEEE Photon. Tech. Lett.*, **11**, pp. 931-933 (1999).

28. A. E. Zhukov, A. R. Kovsh, N. A. Maleev, S. S. Mikhrin, V. M. Ustinov, A. F. Tsatsul'nikov, M. V. Maximov, B. V. Volovik, D. A. Bedarev, Yu. M. Shernyakov, P. S. Kop'ev, and Zh. I. Alferov, N. N. Ledentsov and D. Bimberg.,"Long-wavelength lasing from multiply stacked InAs/InGaAs quantum dots on GaAs substrates," *Appl. Phys. Lett.*, **75**, 1926 (3 pages), (1999).

29. A. E. Zhukov, et al.," Continuous-wave operation of long-wavelength quantum-dot diode laser on a GaAs substrate," *IEEE Photon. Tech. Lett*, **11**, pp. 1345-1347 (1999).

30. Y. Nakata, K. Mukai, M. Sugawara, K. Ohtsubo, H. Ishikawa, and N. Yokoyama," Molecular beam epitaxial growth of InAs self-assembled quantum dots with light-emission at 1.3 μm," *J. Cryst. Growth* **208**, pp. 93-99 (2000).

31. R. S. Attaluri, S. Annamalai, K. T. Posani, A. Stintz, and S. Krishna, "Effect of Si doping on normal icidence InAs/In0.15Ga0.85As dots-in-well quantum dot infrared photdetectors," *J. Appl. Phys.* **99**, 083105 (3 pages), May (2006).

32. N. N. Ledentsov, A. R. Kovsh, A. E. Zhukov, N. A. Maleev, S. S. Mikhrin, A. P. Vasil'ev, E. S. Semenova, M. V. Maximov, Yu M. Shernyakov, N. V. Kryzhanovskaya, V. M. Ustinov, and D. Bimberg, "High performance quantum dot lasers on GaAs substrates operating in 1.5 μm range," *Electron. Lett.*, **39**, pp. 1126-1128, July (2003).

33. J. Gowar, *Optical Communication Systems*, pp. 71-89, Prentice Hall, London, (1984).

34. J. M. Senior, *Optical Fiber Communications: Principles and Practice*, 2nd Ed., pp. 84-153, Prentice Hall, U.K., (1992).

35. G. P. Agrawal, *Fiber-Optic Communication Systems*, 3rd ed., Wiley Interscience, N.Y., (2002).

36. I. D. Aggarwal, G. Lu, *Fluoride Glass Fiber Optics*, pp. xi-xiv, Academic Press, (1991).

37. James A. Harrington, *Infrared Fibers and their Applications*, pp. 5-7, SPIE Press, (2004).

38. M. N. Abedin, T. F. Refaat, O. V. Sulima, S. Ismail and U.N. Singh, "Two-micron detector development using Sb-based material systems," *Proceedings of the Sixth Annual NASA Earth Science Technology Conference*, ESTC-2006, (2006).

39. S. D. Humphries, K. S. Repasky, P. Nachman, J. A. Shaw, J. L. Carlsten, L. H. Spangler, "Atmospheric carbon dioxide measurements using a tunable laser based system," *6th Annual Conference on Carbon Capture & Sequestration*, Pittsburgh, Pennsylvania, (2007).

40. P. Norton, "Infrared sensors in spacecraft that monitor planet Earth," *Opto-Electron. Rev.*, **16**, pp. 105-117, (2008).

41. N. P. Prasad, *Introduction to Biophotonics*, John Wiley & Sons Canada, Ltd., (2003).

42. R. Weissleder and U. Mahmood, "Molecular imaging," *Radiology* **219**, pp. 316-333 (2001).

43. S. R. Cherry, "In vivo molecular and genomic imaging: new challenges for imaging physics," *Physics in Medicine and Biology* **49**, R13-R48 (2004).

44. C. Bremer, C. H. Tung, A. Bogdanov, Jr., and R. Weissleder, "Imaging of differential protease expression in breast cancers for detection of aggressive tumor phenotypes," *Radiology* **222**, pp. 814-818 (2002).

45. S. Krishna, "Quantum dots-in-a-well infrared photodetectors," *J. Phys. D: Appl. Phys.*, **38,** pp. 2142-2150 (2005).

46. S. Chakrabarti, A. D. Stiff, P. Bhattacharya, and S. W. Kennerly, "High responsivity AlAs/InAs/GaAs superlattice quantum dot infrared photodetector," *Electron. lett.*, **40,** pp.197-198, Feb. (2004).

47. S. Xiaohua, S. Chakrabarti, P. Bhattacharya, G. Ariyawansa and A. G. Unil Perera, "A Resonant Tunneling Quantum-Dot Infrared Photodetector," *IEEE J. Quantum Electron.*, **41**, pp. 974-979 (2005).

48. P. Bhattacharya, X. H. Su and S. Chakrabarti, "Characteristics of a Tunneling Quantum-dot Infrared Photodetector Operating at Room Temperature," *Appl. Phys. Lett.* **86**, 191106 (3 pages), May (2005).

49. A. D. Stiff, S. Krishna, P. Bhattacharya, and S. W. Kennerly, "Normal-incidence, high-temperature, mid-infrared, InAs-GaAs vertical quantum-dot infrared photodetector," *IEEE J. Quantum Electron.* **37**, pp. 1412-1419, Nov. (2001).

50. D. Pan and E. Towe, "Normal-incidence intersubband (In, Ga)As/GaAs quantum dot infrared photodetectors," *Appl. Phys. Lett.* **73**, pp. 1937-1939 (1998).

51. L. Jiang, S. S. Li, N. T. Yeh, J. I. Chiy, C. E. Ross and K. S. Jones "$In_{0.6}Ga_{0.4}As$/GaAs quantum-dot infrared photodetector with operating temperature up to 260 K,", *Appl. Phys. Lett.* **82**, 1986 (3 pages), Mar. (2003).

52. M. Sugawara, K. Mukai, and H. Shoji, "Effect of phonon bottleneck on quantum-dot laser performance," *Appl. Phys. Lett.*, **71**, pp. 2791-2793 (1997).

53. K. Ikeda,, H. Sekiguchi, F. Minami, J. Yoshino, Y. Mitsumori, H. Amanai, S. Nagao, and S. Sakaki, "Phonon bottleneck effects in InAs/GaInP quantum dots," *Journal of Luminescence* **108**, pp. 273–276 (2004).

54. D. Bimberg, M. Grundmann, and N. N. Ledentsov, "*Quantum Dot Heterostructures*," (John Wile & Sons Ltd, England, 19995).

55. J. Phillips, K. Kamath, T. Brock, and P. Bhattacharya, "Characteristics of InAs/AlGaAs self-organized quantum dot modulation doped field effect transistors," *Appl. Phys. Lett.*, **72**, 3509 (3 pages), (1998).

56. S. Kim, H. Mohseni, M. Erdtmann, E. Michel, C. Jelen, and M. Razeghi, "Growth and characterization of InGaAs/InGaP quantum dots for midinfrared photoconductive detector," *Appl. Phys. Lett.*, **73,** 963 (3 pages), (1998).

57. Dong Pan, E.Towe, and S. Kennerly, "Normal-incidence intersubband .In, Ga.As/GaAs quantum dot infraredphotodetectors," *Appl. Phys. Lett.*, **73**, 1937 (3 pages), Oct. (1998).

58. S. Maimon, E. Finkman, G. Bahir, S. E. Schacham, J. M. Garcia and P. M. Petroff, "Intersublevel transitions in InAs/GaAs quantum dots infrared photodetectors," *Appl. Phys. Lett.* **73**, pp. 2003-2005 (1998).

59. S. J. Xu, S. J. Chua, T. Mei, X. C. Wang, X. H. Zhang, G. Karunasiri, W. J. Fan, C. H. Wang, J. Jiang, S. Wang, and X. G. Xie, "Characteristics of InGaAs quantum dot infrared photodetectors," *Appl. Phys. Lett.* **73**, 3153 (3 pages), (1998).

60. N. Horiguchi, T. Futatsugi, Y. Nakata, N. Yokoyama, T. Mankad, and P. M. Petroff, "Quantum Dot Infrared Photodetector Using Modulation Doped InAs Self-Assembled Quantum Dots," *Jpn. J. Appl. Phys.*, **38**, pp. 2559-2561 (1999).

61. E. Kim, A. Madhukar, Y. Zhengmao and J. C. Campbell, "High detectivity InAs quantum dot infrared photodetectors," *Appl. Phys. Lett.* **84**, 3277 (3 pages), (2004).

62. D. Pan, E. Towe, and S. Kennerly, "A five-period normal-incidence (In, Ga)As/GaAs quantum-dot infrared photodetector," *Appl. Phys. Lett.* **75**, 2719 (3 pages), (1999).

63. L. Chu, A. Zrenner, G. Bohm, and G. Abstreiter, "Normal-incident intersubband photocurrent spectroscopy on InAs/GaAs quantum dots," *Appl. Phys. Lett.*, **75**, 3599 (3 pages), (1999).

64. D. M. –T. Kuo, A. Fang, and Y. C. Chang," Theoretical modeling of dark current and photo-response for quantum well and quantum dot infrared detectors," *Infrared Physics & Technology* **42**, pp. 433-442 (2001).

65. M. B. El Mashade, M. Asir and A. Nasr, "Theoretical analysis of quantum dot infrared photodetectors," *Semicond. Sci. Technol.* **18**, pp. 891-900 (2003).

66. V. Ryzhii, "Negative differential photoconductivity in quantum-dot infrared photodetectors," *Appl. Phys. Lett.* **78**, 3346 (3 pages), (2001).

67. V. Ryzhii, I. Khmyrova, V. Mitin, and M. Stroscio, "On the detectivity of quantum-dot infrared photodetectors," *Appl. Phys. Lett.* **78**, 3523 (3 pages), (2001).

68. V. Ryzhii, "The theory of quantum-dot infrared phototransistors," *Semicond. Sci. Technol.*, **11**, pp. 759-765 (1996).

69. V. Ryzhii, I. Khmyrova, V. Pipa, V. Mitin and M. Willander, "Device model for quantum dot infrared photodetectors and their dark-current characteristics," *Semicond. Sci. Technol.* **16**, pp. 331-338 (2001).

70. N. Vukmirovic, Z. Ikonic, I. Savic, D. Indjin and P. Harrison, "A microscopic model of electron transport in quantum dot infrared photodetectors," *J. Appl. Phys.*, **100**, 74502 (10 pages), (2006).

71. N. Vukmirovic, Z. Ikonic, V. D. Jovanovic, D. Indjin and P. Harrison," Optically pumped intersublevel midinfrared lasers based on InAs-GaAs quantum dots," *IEEE J. Quantum Electron.* **41**, pp. 1361-1368 (2005).

72. A. Amtout, S. Raghavan, P. Rotella, G. von Winckel, A. Stintz and S. Krishna, "Theoretical modeling and experimental characterization of InAs/InGaAs quantum dots in a well detector," *J. App. Phys.*, **96**, 3782 (5 pages), (2004).

73. H. Jiang and J. Singh, "Strain distribution and electronic spectra of InAs/GaAs self-assembled dots: An eight-band study," *Phys. Rev. B* **56**, pp. 4696- 4701 (1997).

74. M. A. Naser, M. J. Deen and D. A. Thompson, "Theoretical modeling of dark current in quantum dot infrared photodetectors using nonequilibrium Green's functions," *J. Appl. Phys.* **104**, 14511 (11 pages), July (2008).

75. M. A. Naser, M. J. Deen and D. A. Thompson, "Spectral function and responsivity of resonant tunneling and superlattice quantum dot infrared photodetectors using Green's function," *J. Appl. Phys.* **102**, 83108 (12 pages), Oct.(2007).

76. M. A. Naser, M. J. Deen, D. A. Thompson, "Spectral function of InAs/InGaAs quantum dots in a well detector using Green's function," *J. Appl. Phys.* **100**, 093102 (6 pages) , Nov.(2006).

77. M. A. Naser, M. J. Deen and D. A. Thompson, "Theoretical Modeling of Quantum Dot Infrared Photodetectors," *14th Canadian Semiconductor Technology Conference* (12 August 2009).

78. M. A. Naser, M. J. Deen and D. A. Thompson, "Modeling and Optimization of Quantum Dot Infrared Photodetectors," *Electrochemical Society Conference*, (1 July 2008).

79. S. Datta, *Electronic Transport in Mesoscopic Systems* (Cambridge University, Press, 1995).

80. G. D. Mahan, *Many-Particle Physics* (Kluwer Academic/ Plenum Publishers, New York, 2000).

81. P. C. Martin and J. Schwinger, "Theory of many- particle systems," *Phys. Rev.*, **115**, pp. 1342-1349 (1959).

82. L. P. Kadanoff and G. Baym, *Quantum statistical Mechanics*, Frontiers in physics Lecture notes series, Benjamin/ cummings, (1962).

83. L. V. Keldysh, "Diagram technique for non- equilibrium processes," *sov. Phys. JETP* **20**, pp. 1018-1026, (1965).

84. D. C. Langreth, linear and non- linear Electron transport in solids, eds. J. T. Devreese and E. Van Doren, NATO Advanced Study Institute Series B, vol. **17**, p.3, plenum, New York (1976).

85. P. Danielewicz, "Quantum theory of non-equilibrium processes," *Ann. Phys.*, **152**, 239, (1984).

86. J. Rammer and H. Smith, "Quantum field-theoritical methods in transport theory of metals," *Rev. Mod. Phys.* **58,** pp. 323-359, (1986)

87. G. D. Mahan, "Quantum transport equation for electric and magnetic fields," *phys. Rep.* **145,** pp. 251-318, (1987)

88. F. S. Khan, J. H. Davies and J. W. Wilkins, "Quantum transport equations for high electric fields," *Phys. Rev. B*, **36**, pp. 2578-2597 (1987).

89. E. V. Anda and F. Flores, "The role of inelastic scattering in resonant tunneling heterostructures," *J. Phys. Cond. Matter*, **3,** pp. 9087-9101 (1991).

90. E. Runge and H. Ehrenreich, "Non-equilibrium transport in alloy-based resonant tunneling system," *Annals of Physics,* **219**, 55 (1992).

91. R. Lake and S. Datta, "Rate equations from the Keldysh formalism applied to the phonon peak in resonant tunneling diodes," *Phys. Rev. B*, **46**, pp. 6427-6438 (1993).

92. H. M. Pastawki and H. Ehrenreich, "Classical and quantum transport from generalized Landauer-Buttiker equations. II. Time-dependant resonant tunneling," *phys. Rev. B,* **46,** pp. 4053-4070 (1992).

93. C. Caroli, R. Combescot, P. Nozieres and D. Saint-James, "A direct circulation of the tunneling current :IV. Electron-phonon interaction effects," *J. phys. C.:solid state Physics*, **5**, pp. 21-42 (1972).

94. H. Hang and A. Jauho, Quantum Kinetics in transport and optics of semiconductors (Springer-Velag, 1996).

95. P. I. Danielewicz, "Quantum theory of nonequilibrium processes," *Annals of Physics*, **152**, Issue 2, pp. 239-304 (1984).

96. D. K. Ferry and S. M. Goodnick, *Transport in Nanostructures* (Cambridge University, Press, 1997).

97. J. -Y. Marzin and G. Bastard, "Calculation of the energy levels in InAs/GaAs quantum dots," *Solid State Commun.* **92**, pp. 437-442, (1994).

98. M. Califano, and P. Harrison, "Approximate methods for the solution of quantum wires and dots: Connection rules between pyramidal, cuboidal, and cubic dots," *J. Appl. Phys.* **86**, pp. 5054-5059, (1999).

99. M..Califano and P. Harrisonn, "Presentstion and experimental validation of a single-band, constant-potential model for self – assembled InAs/GaAs quantum dots," *Phys. Rev. B*, **61**, pp. 10959-10965 (2000).

100. D. Gershoni, H. Temkin, G. J. Dolan, J. Dunsmuir, S. N. G. Chu, and M. B. Panish, " Effects of two-dimensional confinement on the optical properties of InGaAs/InP quantum wire structures," *Appl. Phys. Lett.*, **53**, 995 (3 pages), (1988).

101. S. Li, J. Xian, J. Liu, F. Yang, Z. Niu, S. Feng and H. Zheng, " InAs/GaAs single-electron quantum dot qubit," *J. App. Phys.* **90**, 6151 (5 pages), (2001).

102. Y. Zou, P. Grodzinski, E. P. Menu, W. G. Jeong, P. D. Dapkus, J. J. Alwan and J. J. Coleman, "Characterization and determination of the band-gap discontinuity of the $In_xGa_{1-x}As$/GaAs pseudomorphic quantum well," *Appl. Phys. Lett.* **58**, 601 (3 pages), (1991).

103. E. S. Koteles, "Determining energy-band offsets in quantum wells using only spectroscopic data," *J. Appl. Phys.* **73,** 8480 (5 pages), (1993).

104. F. Michael,M. D. Johnson, "Replacing leads by self-energies using non-equilibrium Green's functions, " *Physica B* **339**, Issue 1, pp. 31-38 (2003).

105. B. Aslan, H. C. Liu, M. Korkusinski, S. -J. Cheng and P. Hawrylak, "Response spectra from mid- to far-infrared, polarization behaviors, and effects of electron numbers in quantum-dot photodetectors," *Appl. Phys. Lett.* **82,** 630 (3 pages), (2003).

106. S. Chakrabarti, X. H. Su, P. Bhattacharya, G. Ariyawansa and A. G. U. Perera, "Characteristics of a multi-color InGaAs/GaAs quantum dot infrared photodetector," *IEEE Photonics Tech. Lett.*, Vol. **17**, No. 1, pp.178-180, (January 2005).

107. K. Pierz, S. Krishna, P. Bhattacharya and S. Kennerly, "Normal-incidence, high-temperature, mid-infrared, InAs-GaAs vertical quantum-dot infrared photodetector",*IEEE J. Quantum Electron.* **37**, pp. 1412-1419 (2001).

108. I. Vurgaftman, J. R. Meyer, and L. R. Ram-Mohan, "Band parameters for III–V compound semiconductors and their alloys ," *J. Appl. Phys.* **89**, pp. 5815-5875 (2001).

109. S. L. Chuang, Physics of Optoelectronic Devices, (John Wiley & Sons, Inc., 1995).

110. J. H. Davies, The Physics of Low-Dimensional Semiconductors, (Cambridge University Press, 1998).

111. R. Lake and S. Datta, "The Non-equilibrium Green's Function Method Applied to Double Barrier Resonant Tunneling Diodes," *Phys. Rev.* B **45**, pp. 6670-6685 (1992).

112. M. J. McLennan, Y. Lee and S. Datta, "Voltage Drop in Mesoscopic Systems: A Numerical Study Using a Quantum Kinetic Equation," *Phys. Rev.* B **43**, pp. 13846-13884 (1991).

113. M. Cahay, M. McLennan, S. Datta, and M. S. Lundstrom, "Importance of space-charge effects in resonant tunneling devices," *Appl. phys. Lett.*. **50**, pp. 612-614 (1987).

114. S. Datta, "A simple kinetic equation for steady-state quantum transport," *J. Phys. Matter* **2**, pp. 8023-8052, (1990).

115. S. Datta.," Nanoscale device modeling: the Green's function method," *Superlattice and Microstructures* **28**, pp. 253-278 (2000).

116. P. D. Siverns, S. Malik, G. McPherson, D. Childs, C. Roberts, R. Murray, B. A. Joyce, and H. Davock, "Scanning transmission-electron microscopy study of InAs/GaAs quantum dots" *Phys. Rev. B* **58**, R10127-R10130 (1998).

117. D. Leonard, M. Krishnamurthy, S. Fafard, J. L. Merz, and P. M. Petroff, , "Molecular-beam epitaxy growth of quantum dots from strained coherent uniform islands of InGaAs on GaAs," *J. Vac.Sci. Technol. B* **12**, pp. 1063-1066 (1994).

118. J. M. Garcia, G. Medeiros-Ribeiro, K. Schmidt, T. Ngo, J. L. Feng, A. Lorke, J. Kotthaus, and P. M. Petroff, "Intermixing and Shape Changes during the Formation of InAs Self-Assembled Quantum Dots" *Appl. Phys. Lett.* **71**, 2014 (3 pages), (1997).

119. M. A. Swillam, M. H. Bakr, X. Li and J. Deen, "Efficient sensitivity analysis of time independent Schrödinger equation with application to quantum lasers," *Optics Communications*, **281**, pp 4169-4554 (2008).

120. M. A. Swillam, M. H. Bakr, and X. Li, "Efficient 3D sensitivity analysis of surface plasmon waveguide structures," *Optics Express*, vol. **16**, pp. 16371-16381 Oct. (2008).

121. M. A. Swillam, M.H. Bakr, and X. Li, "Full vectorial 3D sensitivity analysis and design optimization using BPM," *IEEE J. Lightwave Technology*, vol. **26**, pp. 528 – 536, Mar. (2008).

122. X. Lu and J. Vaillancourt, and M. J. Meisner, "Temperature-dependent photoresponsivity and high-temperature (190 K) operation of a quantum dot infrared photodetector," *Appl. Phys. Lett.* **91**, 051115 (3 pages), (2007).

123. Z. Ye and J. C. Campbell, Z. Chen, E. Kim, and A. Madhukar, "Noise and photoconductive gain in InAs quantum-dot infrared photodetectors," *Appl. Phys. Lett.* **83**, pp. 1234-1236 (2003).

124. H. C. Liu, "Noise gain and operating temperature of quantum well infrared photodetectors," *Appl. Phys. Lett.* **61**, pp. 2703-2705, (1992).

125. S. Tavakoli, M. A. Naser, D. A. Thompson, and M. J. Deen, "Experimental characterization and theoretical modeling of the strain effect on the evolution and inter-band transitions of InAs quantum dots grown on $In_xGa_{1-x}As$ ($0.0 \leq x \leq 0.3$) metamorphic pseudosubstrates on GaAs wafers", *J. Appl. Phys.*, **106**, 063533 (8 pages), (2009).

126. M. Ryzhii, V. Ryzhii, and M. Willander, "Monte Carlo modeling of electron velocity overshoot effect in quantum well infrared photodetectors," *J. Appl. Phys.*, **84**, pp. 3403-3408 (1998).

127. M. Ryzhii and V. Ryzhii, "Monte Carlo analysis of ultrafast electron transport in quantum well infrared photodetectors," *Appl. Phys. Lett.* **72**, pp. 842-844 (1998).

128. V. Ryzhii and M. Ryzhii, "Nonlinear dynamics of recharging processes in multiple quantum well structures excited by infrared radiation," *Phys.Rev B* . **62**, pp. 10292-10296, (2000).

129. A. Jauho, N. Wingreen, Y. Meir, "Time-dependent transport in interacting and noninteracting resonant-tunneling systems," *Phys.Rev B* . **50**, pp. 5528-5544, (1994).